The Dissertation Committee for Zachary W. Murphy Certifies that this is the approved version of the following Dissertation:

ENERGY PRODUCTION AND CO_2 STORAGE THROUGH MULTIPHASE FLOW EXPERIMENTS IN HYDRATE SYSTEMS

Committee:

Peter B. Flemings, Supervisor

David A. DiCarlo, Co-Supervisor

Kehua You

Daniel Breecker

William Waite

M. Bayani Cardenas

ENERGY PRODUCTION AND CO_2 STORAGE THROUGH MULTIPHASE FLOW EXPERIMENTS IN HYDRATE SYSTEMS

by

Zachary W. Murphy

Dissertation

Presented to the Faculty of the Graduate School of
The University of Texas at Austin
in Partial Fulfillment
of the Requirements
for the Degree of

Doctor of Philosophy

The University of Texas at Austin
December 2023

Acknowledgements

I first must thank my supervisor, Peter Flemings, for consistently pushing me to be a better student, geologist, experimentalist, writer, and thinker. Your unwavering support and guidance have allowed me to grow tremendously over the past five years. I know that your mentorship has prepared me to be successful in whatever endeavors I pursue next.

I am also incredibly grateful to my co-supervisor, David DiCarlo. Your help with all things experimental was invaluable to my project, and you provided me with constant feedback and help when I felt stuck. Most importantly, you helped Peter and I grasp concepts outside of our ‘geologic’ comfort zone.

I would also like to acknowledge my dissertation committee, Kehua You, Bill Waite, Dan Breecker, and Bayani Cardenas for your valuable feedback and support throughout my project. Without the help of Josh O’Connell, Ed Cullen, Aaron Price, and Peter Polito none of my lab work or experiments would have been possible.

Thank you to the graduate students and researchers that I had the pleasure of working with over the last 5 years. Especially, Kevin Meazell, David Fukuyama, Alejandro Cardona, Kristopher Darnell, Kehua You, Yi Fang, Steve Phillips, Landon Lockhart, and Olin Carty.

Above all, I want to thank my wife, Sydney, for being so supportive of me during this long journey. Your constant support and encouragement are the only reason I was able to finish this. Alex, Mom, and Dad, thank you. Finally, to Schatze and Helen for being the best part of my time in Austin.

Abstract

ENERGY PRODUCTION AND CO_2 STORAGE THROUGH MULTIPHASE FLOW EXPERIMENTS IN HYDRATE SYSTEMS

Zachary W. Murphy, Ph.D.
The University of Texas at Austin, 2023

Supervisor: Peter B. Flemings
Co-Supervisor: David A. DiCarlo

Gas hydrate is a solid ice-like compound composed of water and gas. In porous media at low temperatures, high pressures, and with sufficient gas, hydrate will form. Hydrate will occupy a fraction of the pore space, which greatly impacts the petrophysical and geomechanical properties of the system. This study investigates the morphology of gas hydrate within porous media and its impact on multiphase fluid flow behavior in these systems. To explore these impacts, I develop a method for forming hydrates in porous media and then perform systematic flow experiments on the hydrate-bearing samples.

I first perform two-phase (water and hydrate) and three-phase (gas, water, and hydrate) relative permeability experiments. Through these experiments, I show that in hydrate systems water will always be the wetting phase and gas and hydrate will be the non-wetting phases. I then present a modeling framework for relative permeability in the presence of hydrate that is based on the porous media's characteristics and thermodynamically preferred pore occupancy, unlike most previous models that have fixed

pore and tube geometry assumptions. By using the pore occupancy and treating hydrate as a fluid phase, the relative permeability of hydrate-bearing systems can be predicted from measurements of hydrate-free sediment.

Lastly, I explore the potential of CH_4 hydrate reservoirs for simultaneous energy production and CO_2 storage. Using a sand-packed 7.6-meter tube saturated with CH_4 hydrate and water, I inject flue gas (CO_2+CH_4) and observe the dissociation of CH_4 hydrate and subsequent formation of CO_2 hydrate. Chromatographic analysis of the effluent gas unveils the formation of distinct compositional zones during this reactive transport process. These experiments illuminate a solidification and dissociation process where hydrate replacement is composed of a complex series of steps that is driven by the combination of fluid flow and thermodynamics. This dissertation advances the understanding of multiphase flow dynamics that are critical to the lifecycle of hydrate systems on both geologic and production timescales. It offers enhanced modeling of multiphase fluid flow and carbon exchange within hydrate systems, which are relevant to other geologic systems like permafrost.

Table of Contents

Chapter 1: Introduction

1.1 BACKGROUND AND MOTIVATION

Gas hydrates, or hydrates, are complex, crystalline structures formed from a lattice of water molecules encapsulating smaller 'guest' molecules such as methane (CH_4) or carbon dioxide (CO_2) (Kvenvolden & McMenamin, 1980). The most common form of hydrate (Structure I) is composed of 5.75 moles of water to 1 mole of gas, typically CH_4 (Sloan & Koh, 2007). Hydrates will form at low temperature and high-pressure where there is sufficient gas to exceed the gas solubility.

Hydrates occur naturally in large quantities in permafrost and marine sediments (R. Boswell & T. S. Collett, 2011). Methane hydrates play a significant role in the global organic carbon budget with estimates that 5-22% of the world’s organic carbon is stored in CH_4 hydrate (Ruppel & Kessler, 2017). In addition to their role in the carbon cycle, hydrates are studied as potential drilling hazards (McConnell et al., 2012), as potential energy sources (R. Boswell & T. S. Collett, 2011), and as potential CO_2 storage opportunities (Schoderbek & Boswell, 2011). For all of these cases, multiphase flow will occur as water and gas flow through the hydrate systems.

During flow processes, CH_4 was initially thought to be transported in the dissolved phase, however, multiphase flow may occur as gas and water have been shown to travel through the sediment as separate phases (e.g., Fu et al., 2020; You & Flemings, 2021). These three-phase zones are common in hydrate systems at the base of hydrate stability (BHS) or during dissociation or formation of hydrates (e.g., Liu & Flemings, 2006;

Zatsepina & Buffett, 1998). Therefore, to understand how hydrate systems form, evolve, and dissociate, a fundamental understanding of how all three-phases flow is crucial to predicting formation and dissociation of these systems on both production and geologic timescales.

Broadly, this dissertation aims to provide a comprehensive examination of multiphase flow in methane hydrate systems in the context of their formation, stability, and potential uses, with particular emphasis on their impact on fluid flow, their capacity as an energy resource, and their prospective role in CO_2 storage. In the following chapters, an attempt is made to understand the pore scale emplacement and behavior of hydrates and the resulting impacts on fluid flow. These topics are explored with multiphase flow experiments where fluid flow properties and behavior are examined in the presence of methane hydrate. The project first explores methane hydrate pore occupancy in two-phase (hydrate-water) and three-phase (hydrate-gas-water) systems and the impact this pore occupancy has on flow. These experimental techniques are then applied to a set of flow experiments that investigate the potential for CO_2 storage in CH_4 reservoirs.

1.2 RELATIVE PERMEABILITY IN HYDRATE SYSTEMS

Water and gas flow in the presence of hydrate is crucial to understanding and modeling how hydrate systems form, evolve, and dissociate. Much work has been done to understand how hydrates will alter the flow properties and permeability of hydrate-bearing sediments (Waite et al., 2009a). This altered flow behavior will influence hydrate formation, hydrocarbon recovery, and CO_2 storage. Attempts have been made to estimate the in-situ permeability of hydrate-bearing reservoirs through drilling measurements

(Kleinberg et al., 2003; Suzuki et al., 2015) or from pressure-core experiments (Fang et al., 2022; Yoneda et al., 2021). Additionally, many experiments have investigated the flow properties of synthetically (laboratory) formed hydrate (Delli & Grozic, 2014; Johnson et al., 2011; Kneafsey et al., 2011; Liang Lei et al., 2019). However, due to the difficulty in conducting these experiments, forming hydrates in the lab, and the limited opportunities to measure in-situ permeability, there is much uncertainty of the flow behavior in the presence of hydrate. Therefore, many works have attempted to model or simulate the permeability behavior in the presence of hydrate but there are limited experiments to verify the predicted behavior (Dai & Seol, 2014; Daigle, 2016; Myshakin et al., 2012) .

Preliminary works focused on understanding the bulk permeability reduction caused by the presence of hydrate (e.g., Clennell et al., 1999). Measurements from NMR and laboratory flow experiments led to popular models that treat hydrate as part of the porous media and thus result in a decrease in the absolute permeability (Kleinberg et al., 2003). From these works, multiple models were developed on how to quantify this permeability reduction. Generally, there are two models that are widely used for modeling permeability in hydrate systems: the original porous media (OPM) and evolving porous media (EPM) model (Moridis, Kowalsky, et al., 2007). The OPM model assumes that hydrate will behave like a fluid phase and thus the permeability of the system is modeled with the hydrate occupying a fraction of the pore space. Alternatively, the EPM model treats the hydrate as a precipitated solid phase that reduces the bulk porosity and bulk permeability of the system. While both approaches are used, the EPM model is predominantly used in the hydrate literature, especially in experimental works (Delli & Grozic, 2014).

For either the EPM or OPM model, the pore occupancy will control the relative permeability behavior in the system. The two most used models of pore occupancy are the 'pore filling' and 'grain coating' model (Liu & Flemings, 2007). A simple cartoon of these two models is shown in Figure 1.

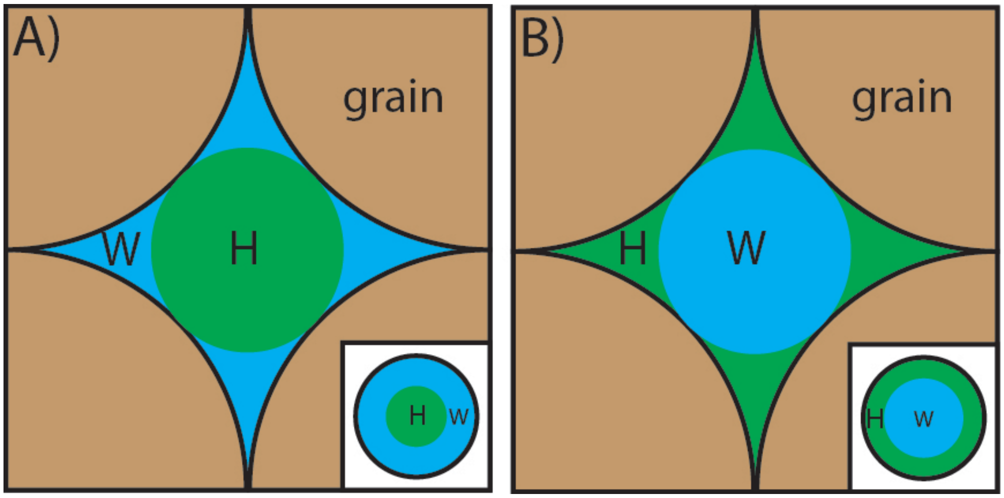

Figure 1 Cartoon schematic of conventional models of hydrate pore occupancy. A) Pore filling model where hydrate forms in the center of the pore. The inset shows the pore-filling capillary tube model. B) Grain coating model where hydrate forms along the grains. The inset shows the grain-coating capillary tube model.

The EPM and OPM model differ in how the relative permeability is determined from the pore occupancy. For the EPM model, the overall permeability reduction caused by hydrate is calculated based on a 'pore-filling' or 'grain-coating' hydrate. These permeability reduction models are based on simple capillary tube model where the hydrate is either in the annulus of the tube (pore filling) or coats the outside of the tube (grain coating). The EPM relative permeability is then modeled by scaling a Brooks & Corey

(1964) type model by the permeability reduction caused by hydrate (Jang & Santamarina, 2014; Johnson et al., 2011). These early models provided a very good estimate of relative permeability in hydrate systems but are overly simplified and do not capture the complex behavior of relative permeability in geologic systems. Even with these simplifications and limited experimental validation, most modeling efforts still use these EPM models for gas and water relative permeability. For the OPM model, the hydrate is treated as any other fluid phase and the relative permeability of the other phases is modeled based on the pore occupancy – either pore filling or grain coating (Moridis et al., 2008).

Like the OPM model, more recent work has used the hydrate pore occupancy to estimate the water relative permeability in hydrate systems (Dai et al., 2019; Daigle, 2016). These works represent a significant advance in predicting relative permeability in hydrate systems but still rely on the 'pore filling' or 'grain coating' assumption but with more complexity (not capillary tube models). Some works have argued that based on the hydrate formation technique the hydrate will either be 'pore filling' or 'grain coating' and then relative permeability models have been developed for each case (Priest et al., 2009).

As hydrate-bearing pressure cores have become more assessable, experiments of in-situ relative permeability of water have been conducted (Fang et al., 2022; Yoneda et al., 2022). These experiments are a breakthrough for permeability measurements but are extremely challenging, slow, require highly specialized equipment, and use valuable core samples. Therefore, there are very few measurements that generally focus on water permeability in the presence of hydrate (no gas) and no clear best practice, OPM or EPM, has been established based on pressure core experiments.

In Chapter 2, I first explore two-phase, water/hydrate systems. I develop a systematic method for forming varying levels of hydrate saturation in a pressure vessel. I then run flow experiments in these systems and measure the two-phase relative permeability of water at varying hydrate saturations. These experiments are among the few systematic sets of experiments to test the flow properties of water in the presence of hydrate. Based on the measured flow properties of the water in the presence of hydrate, I show that water will be the wetting phase and hydrate will be the non-wetting phase in a two-phase system. From these results, I develop a method for determining the relative permeability of water in the presence of hydrate without needing to conduct complex experiments in the presence of hydrate.

The next chapter expands this work to three-phase (gas, water, and hydrate) systems. This chapter presents experiments that measure gas and water relative permeability in the presence of hydrates. These experiments are some of the preliminary experiments to measure both gas and water relative permeability in the presence of CH_4 hydrate. This work shows once again that the water will be the wetting phase in a hydrate system. Gas and hydrate will compete for the larger pores which will determine the flow properties of the system. At my experimental conditions, the measured gas relative permeability suggests that hydrate will be the least-wetting phase and gas will be the intermediate phase. I present a model for gas and water relative permeability that is based on the pore occupancy of the phases. Finally, I show that the relative permeability of gas and water in the presence of hydrate can be determined without running experiments in the presence of hydrate.

From this set of multiphase experiments, I develop a general understanding of how relative permeability concepts should be applied to hydrate systems. Based on concepts from energy production literature (i.e., oil/gas/water relative permeability), I show that hydrate should be treated like any other non-wetting fluid (e.g., oil or gas). My experiments confirm this behavior, and I present a new conceptual model and method for predicting relative permeability in hydrate systems.

1.3 CO_2 SEQUESTRATION IN HYDRATE SYSTEMS

One potential use for hydrate systems is for CO_2 storage or sequestration. Since hydrates can form from many gases (such as CO_2), many works have suggested swapping CO_2 and CH_4 in hydrate reservoirs (Lee et al., 2003; Schoderbek et al., 2012). Generally, these works suggest that if CO_2 is injected into a CH_4 hydrate reservoir, the CH_4 hydrate will be replaced by CO_2 hydrate. This work is predicated on CO_2 hydrate being more thermodynamically preferable as hydrate than CH_4 (Ohgaki et al., 1996).

Original CO_2 exchange work suggested that CH_4 and CO_2 would naturally swap through diffusion to reach equilibrium (Ota et al., 2005). While true, this diffusion is extremely slow and not practical in laboratory or production timescales. Therefore, other techniques have been explored where N_2 is combined with the CO_2 to facilitate the exchange (Boswell et al., 2017). Unlike CO_2, N_2 is a poor hydrate-former and will act as a buffer to hydrate formation and preliminary work suggested that exchange experiments with N_2 present performed much better than those without (Birkedal et al., 2015). Based on these findings, Darnell et al. (2017) and (2019) explored the thermodynamic behavior of CO_2+N_2 injection into CH_4 hydrate systems. This modeling work suggested that the exchange process will consist of dissociation and reformation. Since this technique does not rely on slow diffusion, the exchange process is much faster and more practical for laboratory and production timescales. Due to the complexity of these processes, few experiments have explored these exchange techniques and models. These two models, diffusion and equilibrium, are shown in the cartoon below.

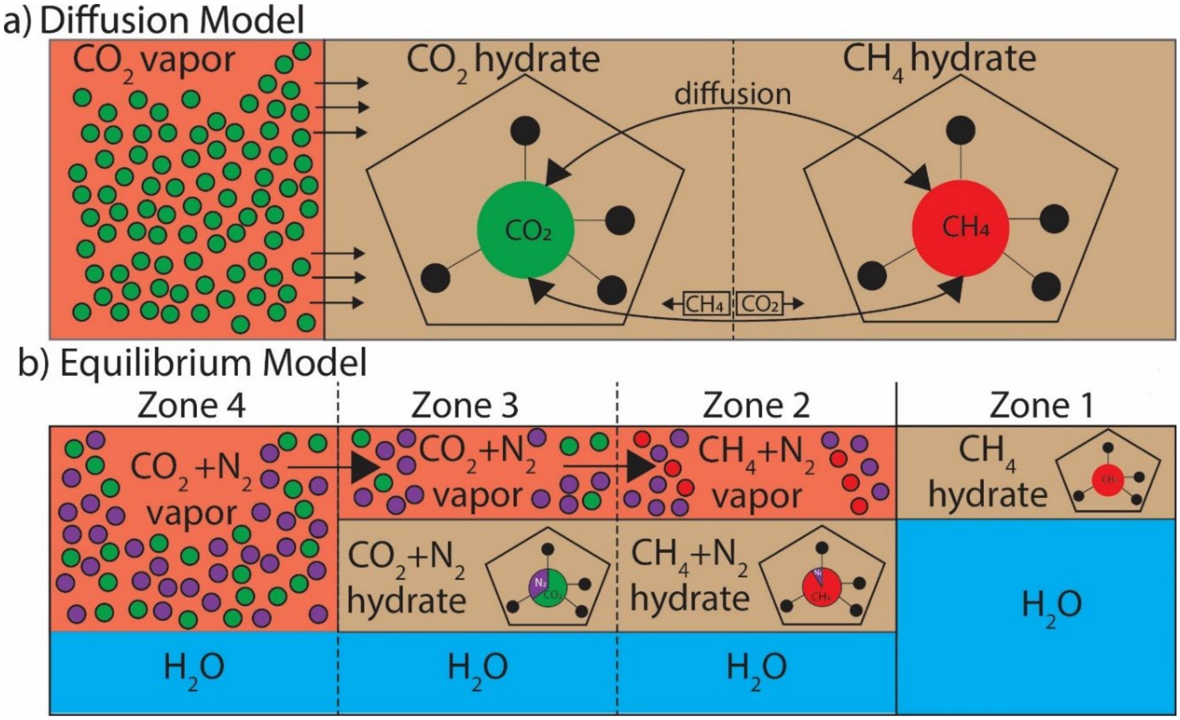

Figure 2 Cartoon representation of diffusion model and equilibrium model. These two models represent two key processes that drive CO2-CH4 guest molecule exchange. The diffusion model shows direct exchange of CH_4 molecules for CO_2 molecules in a slow, diffusion-controlled process. The equilibrium model shows zones of dissociation/dissolution and reformation which is controlled by the local composition and equilibrium in each zone.

The final chapter of this work uses the hydrate formation and multiphase flow methods developed in Chapter 2 and 3 and applies it to a set of experiments that explore the potential of hydrate reservoirs as a storage mechanism for CO_2. CO_2 hydrate systems are of increasing importance for applications of CO_2 storage. As CO_2 storage continues to grow, CO_2 hydrates may play an important role as a potential storage reservoir or trapping mechanism. I present a series of CO_2-CH_4 exchange experiments that elucidate the fundamental processes of CO_2 hydrate formation during flow. These experiments show that CO_2-CH_4 exchange is comprised of dissociation and reformation processes where CH_4 hydrate is systematically dissociated and CO_2 mixed hydrate is systematically formed. This work is one of the first sets of systematic experiments to explore the complex hydrate formation and dissociation processes that occur during CH_4-CO_2 exchange. Among other findings, an updated conceptual model of the equilibrium model for guest molecule exchange is provided.

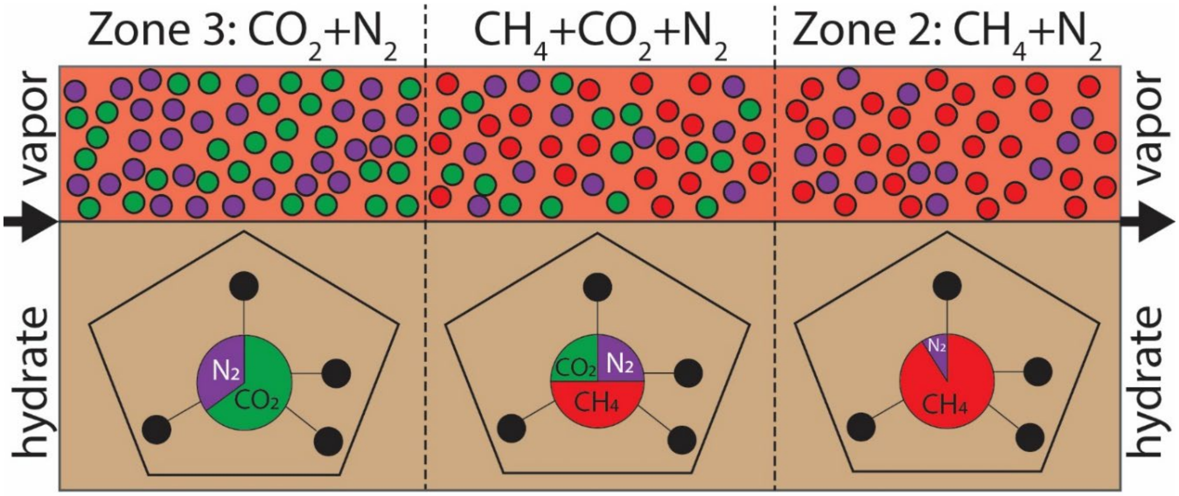

Figure 3 Updated conceptual model of guest molecule exchange for equilibrium model. This updated model includes the center zone which has all three components (CH_4/CO_2/N_2) present in all three phases (hydrate/vapor/liquid). This broad zone forms due to the kinetics of hydrate formation which cause the system to not quickly reach equilibrium. Additionally, this zone allows for increased hydrate formation as CH_4 and CO_2 are more likely hydrate formers than N_2.

1.4 FUTURE WORK

The work presented here explores multiphase flow processes in hydrate systems and attempts to predict how multiple phases and composition of phases will behave during flow. The experiments presented here took many years to accomplish and provide the foundation for countless more experiments using the techniques established for this work.

1. The relative permeability work presented in Chapter 2 and 3 could be expanded to other geologic material to further validate these concepts. A major limitation of laboratory formed hydrates is the (relatively) low hydrate saturation that can be reach (~50%). Natural hydrate reservoirs can have hydrate saturations over 90%. Therefore, measuring water and gas relative permeability in systems in higher hydrate saturation will provide more insight into how these systems behave. To achieve this, these experiments could be conducted on pressure cores that have hydrate saturations of over 90% (Thomas et al., 2020). By conducting these experiments on natural cores, a more complete relative permeability curve could be obtained that range from 0-90% hydrate saturation. Additionally, since the relative permeability curve will be unique for each porous media, additional experiments will highlight the difference between the porous media (e.g., Berea Sandstone vs deep marine mud).
2. The pore occupancy presented in Chapter 3 could be further tested to see if hydrate is indeed the intermediate-wetting phase at higher pressure/deeper depths. Due to pressure limitations of my experimental apparatus, I was unable to run experiments under these conditions. However, in a system that is rated for >15 MPA, these same experiments could be conducted to see if the hydrate/gas pore occupancy changes as a

function of pressure. At higher pressure, we would expect hydrate to be the intermediate-wetting phase and gas to be the least-wetting. These experiments could further validate the pore occupancy and relative permeability model presented in Chapter 3.

3. As CO_2 sequestration continues to grow and become a key part of the global carbon cycle, hydrates will likely play a key role in sequestration processes. The work from Chapter 4 could be adapted and expanded to further test how CO_2 hydrates can aid in carbon sequestration. For example, a simple experiment would be to inject the same flue gas used in Chapter 4 into a saline reservoir at hydrate stable conditions. If at the correct pressure and temperature, a three-phase system with CO_2 hydrate, vapor (CO_2+N_2), and water will form. These experiments could provide the foundation for using CO_2 hydrates as a potential sequestration reservoir without any initial CH_4 hydrate or complex CH_4-CO_2 exchange processes.
4. The slimtube apparatus developed for Chapter 4 has tremendous potential for measuring reactive flow processes in hydrate systems. This setup could be used to test gas fractionation during hydrate formation in similar experiments to the ones presented in Chapter 4.

1.5 REFERENCES

Birkedal, K. A., Hauge, L. P., Graue, A., & Ersland, G. (2015). Transport mechanisms for co2-ch4 exchange and safe co2 storage in hydrate-bearnig sandstone. *Energies*, *8*. https://doi.org/doi: 10.3390/en8054073

Boswell, R., & Collett, T. S. (2011). Current perspectives on gas hydrate resources [10.1039/C0EE00203H]. *Energy & Environmental Science*, *4*(4), 1206-1215. https://doi.org/https://doi.org/10.1039/C0EE00203H

Boswell, R., Schoderbek, D., Collett, T. S., Ohtsuki, S., White, M., & Anderson, B. J. (2017). The Iġnik Sikumi Field Experiment, Alaska North Slope: Design, Operations, and Implications for CO2–CH4 Exchange in Gas Hydrate Reservoirs. *Energy & Fuels*, *31*(1), 140-153. https://doi.org/10.1021/acs.energyfuels.6b01909

Clennell, M. B., Hovland, M., Booth, J. S., Henry, P., & Winters, W. J. (1999). Formation of natural gas hydrates in marine sediments 1. Conceptual model of gas hydrate growth conditioned by host sediment properties. *Journal of Geophysical Research*, *104*(B10), 22985-23003. https://doi.org/10.1029/1999jb900175

Dai, S., Kim, J., Xu, Y., Waite, W. F., Jang, J., Yoneda, J., Collett, T. S., & Kumar, P. (2019). Permeability anisotropy and relative permeability in sediments from the National Gas Hydrate Program Expedition 02, offshore India. *Marine and Petroleum Geology*, *108*, 705-713. https://doi.org/10.1016/j.marpetgeo.2018.08.016

Dai, S., & Seol, Y. (2014). Water permeability in hydrate-bearing sediments: A pore-scale study. *Geophysical Research Letters*, *41*(12), 4176-4184. https://doi.org/10.1002/2014GL060535

Daigle, H. (2016). Relative permeability of hydrate-bearing sediments from critical path analysis. *Journal of Petroleum Science and Engineering*.

Darnell, K. N., Flemings, P. B., & DiCarlo, D. (2019). Nitrogen-Driven Chromatographic Separation During Gas Injection Into Hydrate-Bearing Sediments. *Water Resources Research*. https://doi.org/10.1029/2018wr023414

Darnell, K. N. F., P.B.; DiCarlo, D. (2017). Subsurface injection of combustion power plant effluent as a solid-phase carbon dioxide storage strategy. *Geophysical Research Letters*, *44*, 5521-5530. https://doi.org/10.1002/2017GL073663

Delli, M. L., & Grozic, J. L. H. (2014). Experimental determination of permeability of porous media in the presence of gas hydrates. *Journal of Petroleum Science and Engineering*, *120*, 1-9. https://doi.org/http://dx.doi.org/10.1016/j.petrol.2014.05.011

Fang, Y., Flemings, P. B., Daigle, H., Phillips, S. C., & O'Connell, J. (2022). Permeability of methane hydrate-bearing sandy silts in the deep-water Gulf of Mexico (Green Canyon Block 955). *AAPG Bulletin*, *106*(5), 1071-1100. https://doi.org/https://doi.org/10.1306/08102121001

Fu, X., Jimenez-Martinez, J., Nguyen, T. P., Carey, J. W., Viswanathan, H., Cueto-Felgueroso, L., & Juanes, R. (2020). Crustal fingering facilitates free-gas methane migration through the hydrate stability zone. *Proceedings of the National Academy of Sciences*, *117*(50), 31660-31664. https://doi.org/doi:10.1073/pnas.2011064117

Jang, J., & Santamarina, J. (2014). Evolution of gas saturation and relative permeability during gas production from hydrate-bearing sediments: gas invasion vs. gas nucleation. *Journal of Geophysical Research Solid Earth*, *119*, 116-126. https://doi.org/https://doi.org/10.1002/2013JB010480

Johnson, A., Patil, S., & Dandekar, A. (2011). Experimental investigation of gas-water relative permeability for gas-hydrate-bearing sediments from the Mount Elbert Gas Hydrate Stratigraphic Test Well, Alaska North Slope. *Marine and Petroleum*

Geology, *28*(2), 419-426. https://doi.org/https://doi.org/10.1016/j.marpetgeo.2009.10.013

Kleinberg, R. L., Flaum, C., Griffin, D. D., Brewer, P. G., Malby, G. E., Peltzer, E. T., & Yesinowski, J. P. (2003). Deep sea NMR: Methane hydrate growth habit in porous media and its relationship to hydraulic permeability, deposit accumulation, and submarine slope stability. *Journal of Geophysical Research: Solid Earth*, *108*(B10), 2508. https://doi.org/10.1029/2003JB002389

Kneafsey, T. J., Seol, Y., Gupta, A., & Tomutsa, L. (2011). Permeability of laboratory-formed methane-hydrate-bearing sand: measurements of observations using X-ray computed tomography. *SPE Journal*, *16*(1), 78-94.

Kvenvolden, K. A., & McMenamin, M. A. (1980). *Hydrates of natural gas; a review of their geologic occurrence* [Report](825). (Circular, Issue. U. S. G. Survey. http://pubs.er.usgs.gov/publication/cir825

Lee, H., Seo, Y., Seo, Y.-T., Moudrakovski, I. L., & Ripmeester, J. A. (2003). Recovering Methane from Solid Methane Hydrate with Carbon Dioxide. *Angewandte Chemie International Edition*, *42*(41), 5048-5051. https://doi.org/https://doi.org/10.1002/anie.200351489

Lei, L., Seol, Y., Choi, J.-H., & Kneafsey, T. J. (2019). Pore habit of methane hydrate and its evolution in sediment matrix – Laboratory visualization with phase-contrast micro-CT. *Marine and Petroleum Geology*, *104*, 451-467. https://doi.org/10.1016/j.marpetgeo.2019.04.004

Liu, X., & Flemings, P. B. (2006). Passing gas through the hydrate stability zone at southern Hydrate Ridge, offshore Oregon. *Earth and Planetary Science Letters*, *241*(1–2), 211-226. https://doi.org/doi:10.1016/j.epsl.2005.10.026

Liu, X., & Flemings, P. B. (2007). Dynamic multiphase flow model of hydrate formation in marine sediments. *Journal of Geophysical Research*, *112*(B3). https://doi.org/doi:10.1029/2005jb004227

McConnell, D. R., Zhang, Z., & Boswell, R. (2012). Review of progress in evaluating gas hydrate drilling hazards. *Marine and Petroleum Geology*, *34*(1), 209-223. https://doi.org/10.1016/j.marpetgeo.2012.02.010

Moridis, G., Kowalsky, M. B., & Pruess, K. (2008). *TOUGH+HYDRATE v1.2 User's Manual: A Code for the Simulation of System Behavior in Hydrate-Bearing Geologic Media*. Lawrence Berkeley National Laboratory. http://escholarship.org/uc/item/23p861p4

Moridis, G. J., Kowalsky, M. B., & Pruess, K. (2007). Depressurization-Induced Gas Production From Class 1 Hydrate Deposits. *SPE Reservoir Evaluation & Engineering*, *10*(05), 458-481.

Myshakin, E. M., Gaddipati, M., Rose, K., & Anderson, B. J. (2012). Numerical simulations of depressurization-induced gas production from gas hydrate reservoirs at the Walker Ridge 313 site, northern Gulf of Mexico. *Marine and Petroleum Geology*, *34*(1), 169-185. https://doi.org/10.1016/j.marpetgeo.2011.09.001

Ohgaki, K., Takano, K., Sangawa, H., Matsubara, T., & Nakano, S. (1996). Methane exploitation by carbon dioxide from gas hydrates—phase equilibria for CO2-CH4 mixed hydrate system—. *Journal of chemical engineering of Japan*, *29*(3), 478-483.

Ota, M., Abe, Y., Watanabe, M., Smith, R. L., & Inomata, H. (2005). Methane recovery from methane hydrate using pressurized CO2. *Fluid Phase Equilibria*, *228-229*, 553-559. https://doi.org/https://doi.org/10.1016/j.fluid.2004.10.002

Priest, J. A., Rees, E. V. L., & Clayton, C. R. I. (2009). Influence of gas hydrate morphology on the seismic velocities of sands. *Journal of Geophysical Research: Solid Earth*, *114*(B11), B11205. https://doi.org/10.1029/2009JB006284

Ruppel, C. D., & Kessler, J. D. (2017). The interaction of climate change and methane hydrates. *Reviews of Geophysics*, *55*(1), 126-168. https://doi.org/https://doi.org/10.1002/2016RG000534

Schoderbek, D., & Boswell, R. (2011). Iġnik Sikumi# 1, gas hydrate test well, successfully installed on the Alaska North Slope. *Natural Gas & Oil*, *304*, 285-4541.

Schoderbek, D., Martin, K. L., Howard, J., Silpngarmlert, S., & Hester, K. (2012, 2012/12/3/). *North Slope Hydrate Fieldtrial: CO2/CH4 Exchange*

Sloan, E. D., & Koh, C. A. (2007). *Clathrate Hydrates of Natural Gases*. CRC Press.

Suzuki, K., Takayama, T., & Fujii, T. (2015). Density structure report from logging-while-drilling data and core data at the first offshore gas production test site on Daini-Atsumi Knoll around eastern Nankai Trough. *Marine and Petroleum Geology*, *66*, 388-395. https://doi.org/10.1016/j.marpetgeo.2015.02.026

Thomas, C., Phillips, S. C., Flemings, P. B., Santra, M., Hammon, H., Collett, T. S., Cook, A. E., Pettigrew, T., Mimitz, M., Holland, M., & Schultheiss, P. (2020). Pressure coring operations during The University of Texas-Gulf of Mexico 2-1 (UT-GOM2-1) Hydrate Pressure Coring Expedition in Green Canyon Block 955, northern Gulf of Mexico. *AAPG Bulletin*, *104*(9), 1877-1901. https://doi.org/10.1306/02262019036

Waite, W. F., Santamarina, J. C., Cortes, D. D., Dugan, B., Espinoza, D. N., Germaine, J., Jang, J., Jung, J. W., Kneafsey, T. J., Shin, H., Soga, K., Winters, W. J., & Yun, T. S. (2009a). Physical properties of hydrate-bearing sediments. *Reviews of Geophysics*, *47*(4). https://doi.org/10.1029/2008rg000279

Yoneda, J., Jin, Y., Muraoka, M., Oshima, M., Suzuki, K., Waite, W. F., & Flemings, P. B. (2022). Comprehensive pressure core analysis for hydrate-bearing sediments from Gulf of Mexico Green Canyon Block 955, including assessments of geomechanical viscous behavior and nuclear magnetic resonance permeability. *AAPG Bulletin*, *106*(5), 1143-1177. https://doi.org/https://doi.org/10.1306/04272120204

Yoneda, J., Jin, Y., Muraoka, M., Oshima, M., Suzuki, K., Walker, M., Otsuki, S., Kumagai, K., Collett, T. S., Boswell, R., & Okinaka, N. (2021). Multiple physical properties of gas hydrate-bearing sediments recovered from Alaska North Slope 2018 Hydrate-01 Stratigraphic Test Well. *Marine and Petroleum Geology*, *123*, 104748. https://doi.org/https://doi.org/10.1016/j.marpetgeo.2020.104748

You, K., & Flemings, P. B. (2021). Methane Hydrate Formation and Evolution During Sedimentation. *Journal of Geophysical Research-Solid Earth*, *126*(4). https://doi.org/10.1029/2020JB021235

Zatsepina, O. Y., & Buffett, B. A. (1998). Thermodynamic conditions for the stability of gas hydrate in the seafloor. *J. Geophys. Res.*, *103*(B10), 24127-24139. https://doi.org/10.1029/98jb02137

Chapter 2: Hydrate is a non-wetting phase in porous media

2.1 ABSTRACT

[1]In porous media containing gas hydrate, the hydrate morphology impacts the flow behavior of the fluid phases. We hypothesize that hydrate emplaces itself as a non-wetting phase and use this idea to describe relative permeability of water in the presence of hydrate. We perform steady-state relative permeability measurements in hydrate-bearing samples with a range of hydrate saturation. We measure and compare water relative permeability in the presence of gas and in the presence of hydrate and find that the water relative permeability is the same in both cases. This suggests that 1) relative permeability for hydrate systems can be obtained without performing difficult experiments on hydrate bearing sediments, 2) flow properties are porous-media dependent, and 3) models that assume a fixed pore or tube geometry are inadequate.

2.2 INTRODUCTION

Methane hydrates are a significant portion of the global carbon budget, with estimates suggesting ~3x10^{14} m^3 of methane gas is locked in coarse-grained, high hydrate concentration, reservoirs (e.g. R. Boswell & T. Collett, 2011). Fluid flow properties of coarse-grained hydrate-bearing sediments will control how hydrate systems form, dissociate, and evolve on both geologic and production timescales (e.g. Jang & Santamarina, 2014). The vast amount of methane gas stored in hydrate-bearing reservoirs

---

[1] This chapter is published as: Murphy, Zachary W., David A. DiCarlo, Peter B. Flemings, and Hugh Daigle. "Hydrate is a nonwetting phase in porous media." *Geophysical Research Letters* 47, no. 16 (2020): e2020GL089289.
I conceived and designed this study, performed the experiments, gathered the data, conducted the analysis, made the figures, and wrote the manuscript. David DiCarlo, Peter Flemings, and Hugh Daigle edited the manuscript for clarity and provided valuable feedback on the manuscript contents.

has motivated significant research on fluid flow in hydrate systems that spans energy resources (Boswell, 2009; Konno et al., 2017), climate change (Archer et al., 2008; Dickens et al., 1995), and CO_2 sequestration (Darnell et al., 2019; Koh et al., 2016).

Hydrate in porous media reduces the pathways available for flow of fluid phases (water and gas), and understanding this reduction is needed to assess formation (You et al., 2019) and model production of hydrate reservoirs (e.g. Moridis, Reagan, et al., 2007; Myshakin et al., 2019). Emplacement of hydrate can be considered a change in the pore space with related changes in porosity and permeability (e.g. Dai et al., 2012; Waite et al., 2009b) and models to predict reductions in permeability and porosity due to hydrate formation have been built under this concept (Kleinberg et al., 2003; Liu & Flemings, 2006; Moridis et al., 2019).

In contrast, the effects of hydrate can be understood in terms of a fixed pore volume (constant porosity) where the hydrate occupies a *fraction of the pore space* (hydrate saturation S_h = volume hydrate/total pore volume) and the reduction of permeability is parameterized as the *relative permeability* (k_r = measured permeability with hydrate/measured permeability without hydrate) (Blunt, 2017). We believe this approach is simpler as we hypothesize that hydrate occupies the same space in a porous media as a fluid phase. This results in similar pathways for fluid flow, and the same functional forms can be used from the relative permeability literature.

2.3 RELATIVE PERMEABILITY

Relative permeability concepts and models are well defined in the energy production and hydrogeology literature (e.g. Blunt, 2017; Lake, 1989). These models predict how the flow of one fluid phase is affected by the presence of a second fluid phase by considering how the different phases are arranged within the pore system. Surface energies dominate the pore scale emplacement of fluid phases: the interface between the fluid phases deforms to a surface of constant curvature to minimize the free energy. The curvature depends on the amount of non-wetting phase in the system.

Figure 4 shows measurements of water and gas relative permeabilities in Berea sandstone along with a simplified arrangement of the phases in different-sized triangular pores. The phases are delineated into wetting (blue) and non-wetting (red) – the wetting phase is the phase that minimizes the mineral surface energy when it covers the mineral surfaces. For most geologic materials water (brine) is the wetting phase, and the non-wetting phase is usually gas (as in this case) or oil. At high wetting-phase saturations, water exists in all but the largest pores with the smallest interface curvature (A) – this is depicted as three different pore sizes in the inset of Figure 4. As the wetting phase saturation decreases, water is forced into smaller and smaller pores and the interface assumes larger curvatures (B and C).

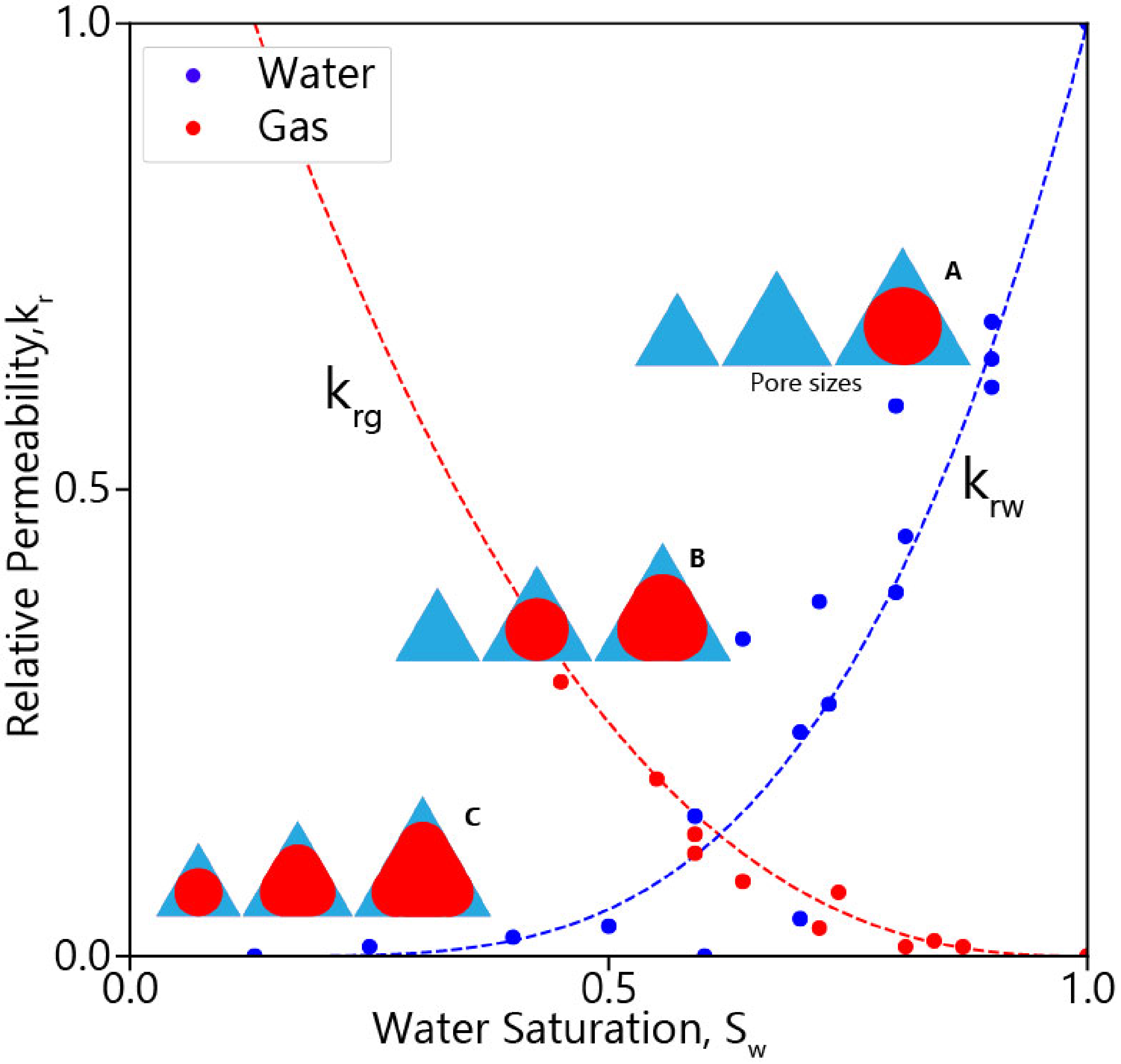

Figure 4 Gas/water drainage relative permeability in a Berea Sandstone. Corey-type fits (dashed lines) give different Corey parameters for the water (nw=3.5, Srw=0.15) and gas (ng=2.5, Srg=0.0) phases. The larger exponent for the wetting phase is a feature of relative permeability. The triangles represent the pore size distribution at three different saturations with blue as the wetting phase and red as the non-wetting phase. A) The non-wetting phase only occupies the largest pores. B,C) As the non-wetting saturation increases, it invades smaller pores until residual wetting saturation is reached.

As the saturation of a given phase is reduced, the effective permeability of that phase is reduced. The largest pore spaces are the best conduits for fluid flow; thus, the wetting-phase relative permeability drops quickly with decreasing wetting-phase saturation (blue line, right to left). In contrast, the non-wetting-phase relative permeability drops at a lower rate with decreasing non-wetting-phase saturation (red line, left to right). The relative permeability of each phase can be modeled with a functional form (e.g. Brooks & Corey, 1964; van Genuchten, 1980), and the wetting phase relative permeability invariably drops more rapidly with a decline in saturating than the non-wetting phase relative permeability (i.e. the wetting phase relative permeability is more non-linear). Importantly, each porous medium has a unique geometry controlled by geology (parent material, depositional environment, diagenesis, etc.), and thus the shape of the curves will be different (Blunt, 2017).

Even though hydrate is solid, it can move through dissolution and reformation (e.g. Liu & Flemings, 2011). Recent experiments suggest that hydrate first forms at the gas/water interface, but then behaves similarly to a mobile, non-wetting phase that will rearrange itself to minimize energy through Ostwald ripening type behavior (e.g. Chen & Espinoza, 2018; L. Lei et al., 2019). This movement is driven by minimizing free energy, and the hydrate/water interface minimizes its energy by deforming to a state of constant curvature. In addition, the surfaces of the grains have lower interfacial energy when contacted by water than hydrate (Waite et al., 2009b). Because of this, we hypothesize that for a hydrate/water system, *hydrate is emplaced like a non-wetting fluid phase.* If hydrate acts as a non-wetting phase, the relative permeability of water in the presence of hydrate should vary as a function of water saturation in the same way as relative permeability of water in the presence of gas or oil. We call this model the *non-wetting model*.

Note that hydrate being a non-wetting phase is not a new concept. Most famously, Clennell (1999) presented this concept, but in terms of relative permeability it has mostly been applied with a capillary tube model of the porous media (Kleinberg et al., 2003). This simplification gives a specific prediction for a functional form of the relative permeability. The wetting and non-wetting models (i.e. grain coating and pore filling) have been used as a guiding assumption for many papers interpreting relative permeability and other sediment properties such as acoustic, hydraulic, and electrical (Mahabadi et al., 2019; Priest et al., 2009; Spangenberg, 2001). However, the actual complexity of the porous media and physics of hydrate formation are not captured in these simple models.

2.4 EXPERIMENTS

To test the non-wetting hypothesis, we performed experiments to measure water relative permeability in the presence of gas and the presence of hydrate.

2.4.1 Gas/water relative permeability

The porous medium was a Berea sandstone core (55 cm length, 3.8 cm diameter) with a measured bulk porosity of 0.22. The oven-dried core was placed in a core holder with 5 pressure taps spaced 4 cm apart that were connected to differential pressure transducers (Figure 5) and a confining stress of 1.7 MPa was applied. The pressure taps were necessary to reduce the influence of capillary end effects (Chen et al., 2017). A vacuum was pulled on the sample to remove all air, and then 3.5% NaCl brine was pulled into the sample to fully saturate the core. The absolute permeability was measured using the steady state method and Darcy's law:

$$k_{abs} = \frac{-Q \cdot \mu}{A}\left(\frac{L}{\Delta P}\right), \tag{1}$$

where Q is the flow rate, μ is the viscosity, L is the length, A is the area, and ΔP is the pressure drop. The bulk absolute permeability of the sample was determined to be 2.17x10^{-13} m^2 (~220 mD).

The relative permeabilities to gas and water were then obtained using the steady-state method. Five different fractional flow rates of water ($f_w = \frac{Q_w}{Q_w + Q_g}$,where Qw is the flow rate of water and Qg is the flow rate of gas) [f_w=1.0, 0.5, 0.1, 0.01, 0] were used and after steady-state was reached (dP/dt=0) the internal pressure drops were recorded. The water removed from the system was weighed to determine the phase saturations. The relative permeability was calculated using the Darcy-Buckingham equation (2) for phase i:

$$k_{r(i)} = \frac{-Q_i \cdot \mu_i}{k_{abs} \cdot A}\left(\frac{L}{\Delta P_i}\right). \tag{2}$$

The gas/water experimental data are shown in Figure 4. We then fit a Brooks-Corey type equation (Brooks & Corey, 1964) to the water (Eq. 3) and gas (Eq. 4) data:

$$k_{rw} = \left(\frac{S_w - S_{rw}}{1 - S_{rw}}\right)^{n_w}, \tag{3}$$

$$k_{rg} = \left(\frac{S_g - S_{rg}}{1 - S_{rg}}\right)^{n_g}, \tag{4}$$

where S_w is water saturation, S_{rw} is residual water saturation, n_w is the water fitting parameter, S_g is gas saturation, S_{rg} is residual gas saturation, and n_g is the gas fitting parameter. The derived model parameters are similar to previous experiments for gas/water in Berea Sandstone (e.g. Chen et al., 2017).

2.4.2 Hydrate formation

We next formed hydrate in the same Berea Sandstone core starting from either a high or low water saturation initial condition. The low saturation method began with a fully methane vapor-saturated core. Brine was then injected until the water saturation was between 10-60%. The high saturation method began with a fully brine-saturated core. Methane gas was then injected until the water saturation decreased to 80-90%.

After the initial condition was achieved, the procedure for both formation methods was the same. At room temperature, methane gas was injected with a syringe pump until the sample reached ~8.5 MPa. The pore pressure was held constant throughout the entire experiment and the amount of gas injected was recorded by the pump. The system was then cooled to 6°C and held constant for the entire experiment (Figure 5). Gas was injected to maintain constant pressure as the system cooled and entered the hydrate stability zone (Figure 5A).

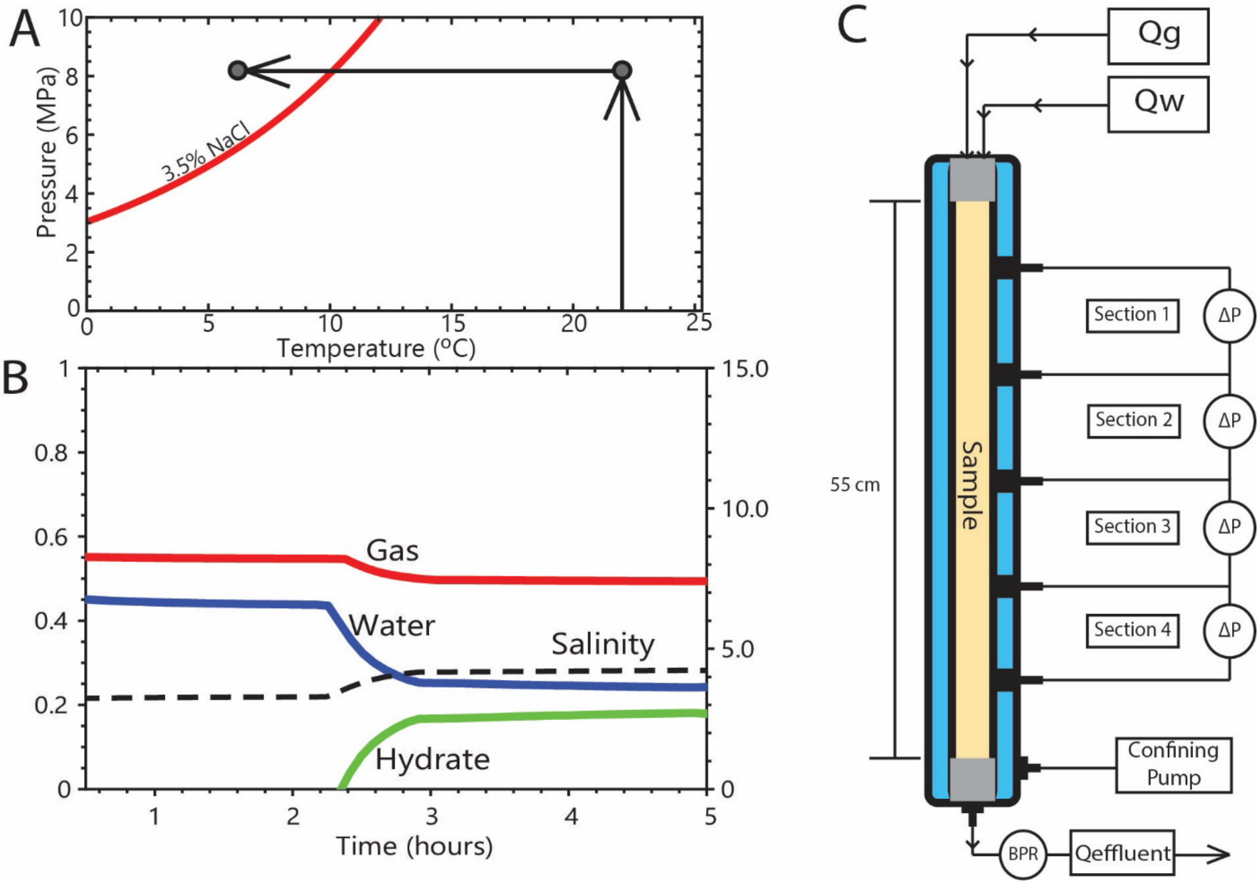

Figure 5 A) Pressure-Temperature diagram and experimental path. Hydrate is stable above the red line. To form hydrate, the sample begins at room temperature and atmospheric pressure. The sample is pressurized to 8 MPa, then cooled to 6°C and held constant. B) Example of mass balance analysis (Appendix A) for low saturation method. Saturation changes are calculated as gas enters system. Hydrate nucleation occurs at ~2.5 hrs and formation rate slow after ~4 hours. C) Experimental design for relative permeability experiments. Flow rates are controlled by upstream pumps. Pressure is measured using differential pressure transducers between each section. Pore pressure is maintained with a back-pressure-regulator (BPR). Confining stress is controlled with a syringe pump.

We monitored the phase saturations through mass balance analysis for the entire experiment (Appendix A). As the sample cools, a small amount of gas was needed to maintain pressure (Figure 5B, hours 0-2.5). After between 2-30 hours, we observed a large amount of gas injected into the system (Figure 5B, hour 2.5). This large jump was interpreted to be initial hydrate formation. The formation continued for hours to days

(Figure 5B, hour 2.5-end). Once we observed that hydrate formation stopped or significantly slowed, we stopped gas injection and reached our final hydrate saturation. This formation process was completed for five different hydrate saturations (Table 1).

2.4.3 Hydrate/water relative permeability

After forming hydrate, 3.5% NaCl brine was flowed through the core until steady state was reached. Initially, residual gas was displaced or reacted into hydrate leaving a two-phase hydrate/water system which took roughly 1-3 pore volumes.

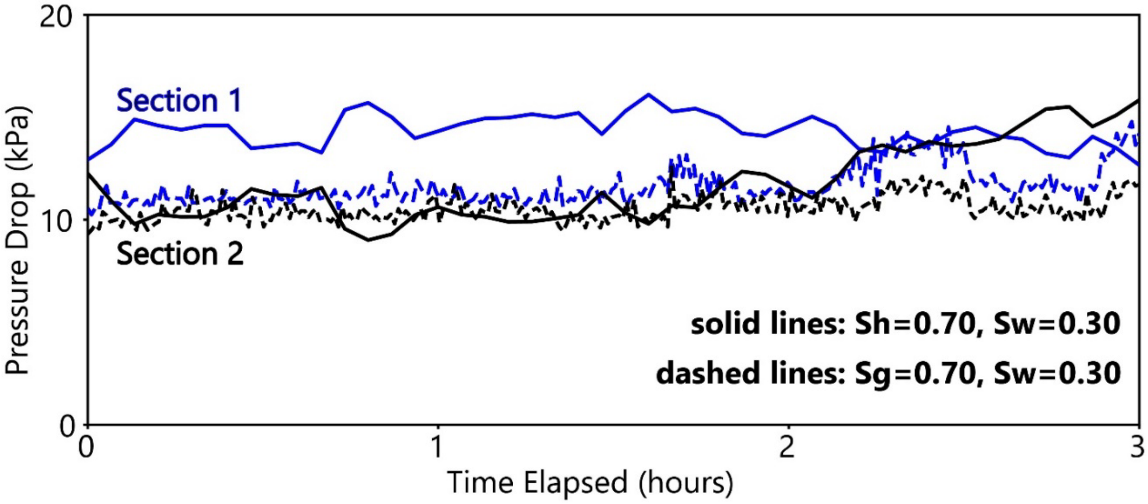

Figure 6 Pressure drop vs time for hydrate/water and gas/water relative permeability experiment. The two data sets shown are at the same flow rate (Qw=0.1 ml/min) and same water saturation (Sw=0.3). Two center sections are shown (blue data: Section 1, black data: Section 2). The scatter is much larger in the hydrate/water data and is likely due to hydrate movement and blockages. The water effective permeability is calculated from the pressure data (eq. 2). The effective permeability for each section is averaged to get a bulk water effective permeability (Table 1) and water relative permeability for each water saturation.

Once only hydrate and water were present in the core, three different flow rates (Q_w=0.01, 0.05, 0.1 ml/min) were used. The measured pressure traces showed larger fluctuations than the gas/water system (Figure 6). A likely explanation is hydrate dissolution and reforming in different parts of the pore space. Pressure readings at individual pressure taps were intermittently lost, presumably due to hydrate blockage. However, there were enough pressure sections to obtain one average value for permeability for the center sections of the core at each hydrate saturation (Table 1, Figure 7). Lastly, the hydrate saturation was confirmed by depressurizing the sample using a method derived from Phillips et al. (2019).

Table 1 Experimental results for hydrate/water relative permeability experiments.

Sample	Formation Method	Hydrate Saturation	$k_{eff,w}$ (mD)	$k_{eff,w}$ (x10^{-13} m^2)	k_{rw}
1	Low Saturation	0.22	67.5	0.666	0.27
2	High Saturation	0.43	12.5	0.123	0.05
3	Low Saturation	0.14	115	1.13	0.46
4	High Saturation	0.62	5.00	0.050	0.02
5	High Saturation	0.70	1.70	0.017	0.007

2.5 DISCUSSION

Figure 7 shows that the water relative permeability in the presence of hydrate (black data) overlies the water relative permeability in presence of gas (gray data). In other words, the measured water relative permeability is independent of the other phase – it depends only on the water saturation.

Comparing the data to various hydrate emplacement models, the behavior is exactly what is predicted from the hydrate as a non-wetting phase (blue line) model. If instead hydrate is emplaced as a wetting phase, the water relative permeability in the presence of hydrate should follow the gas relative permeability from the gas/water measurements. This is shown as the wetting model (red curve) and clearly overpredicts the observed water relative permeability. Unsurprisingly, the simplified tube coating (green curve) and tube filling (purple curve) models overpredict and underpredict the data, respectively.

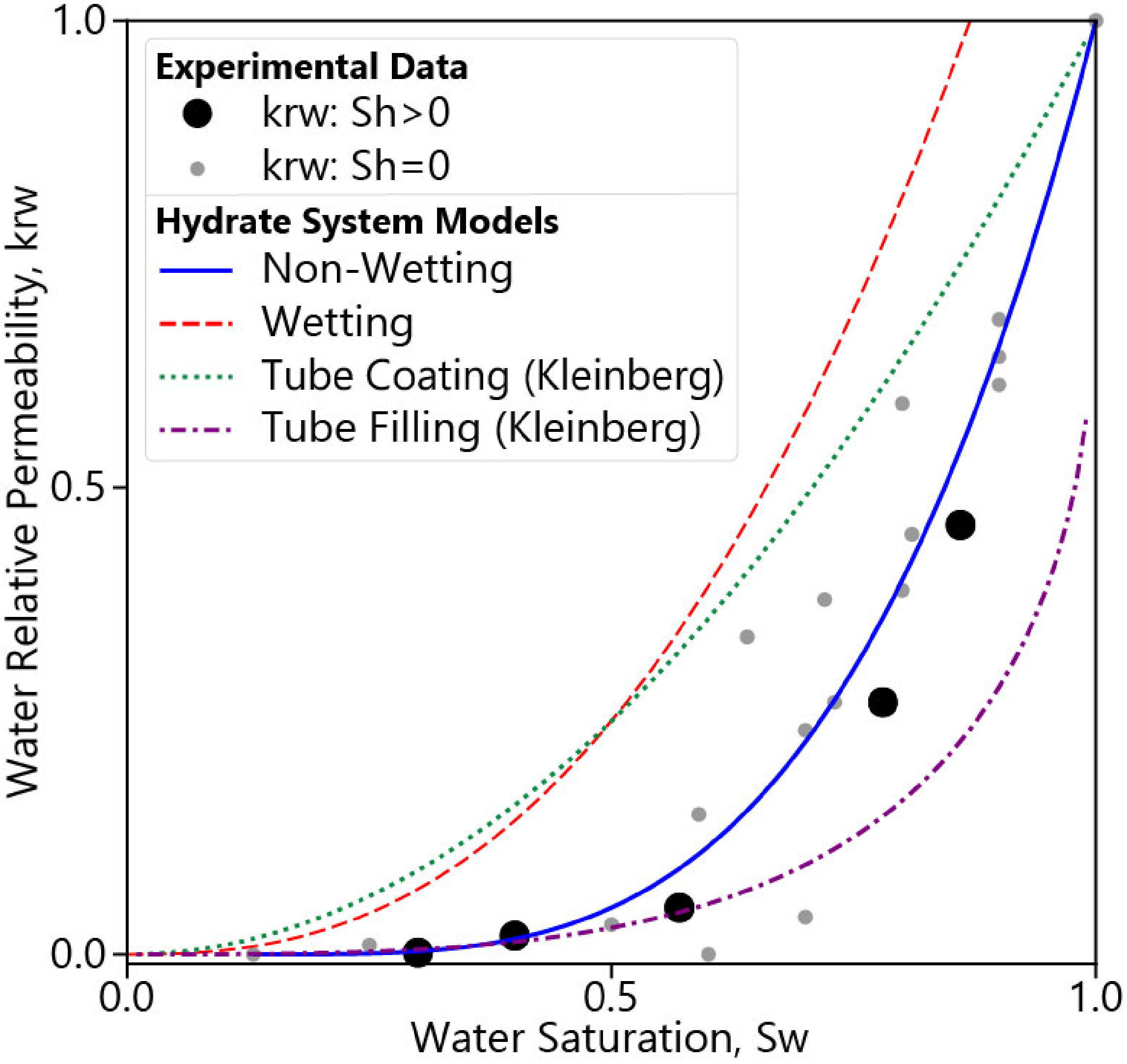

Figure 7 Water relative permeability in the presence of hydrate (black circles) and gas (gray circles) from steady-state experiments. Hydrate non-wetting (blue line) and hydrate wetting (red dashed line) models are fit from gas/water experiments (Figure 4). Two commonly used models for relative permeability for hydrate-bearing porous media are shown from the hydrate literature (Kleinberg et al., 2003).

These results suggest that the best estimate for relative permeability of hydrate/water systems can be obtained from gas/water relative permeability experiments. Such experiments are much simpler to perform than experiments with hydrate since they do not require formation and potential annealing of hydrate, which is a complex process. Furthermore, in cases where the porous medium has been previously studied, it may be easy to apply conventional relative permeability models based on knowledge of the pore geometry.

Other models such as those presented by Kleinberg (2003), Daigle (2016), or others try to capture more of the complexity of porous media and may more successfully describe relative permeability. That said, the advantage of our work is that detailed knowledge of the pore structure is not necessary, and accurate relative permeability predictions are possible from simpler gas/water laboratory experiments.

Other evidence of the non-wetting behavior of hydrate can be seen in both laboratory and natural samples. In many natural systems, hydrate is found in high concentration in coarse grained sediment and is much less abundant in fine grained sediment (Cook & Malinverno, 2013; Phillips et al., 2020). This may be due in part to flow focusing in coarser-grained layers due to their higher intrinsic permeability (e.g. Nole et al., 2016) but is observable in low-flux systems as well, implying a strong influence of capillary phenomena (Cook & Malinverno, 2013; Malinverno, 2010). Likewise, in synthetic porous media, hydrate forms at the gas/water interface but subsequently migrates to the larger pores to minimize surface energy (e.g. Chen et al., 2020; Liang Lei et al., 2019). Since hydrate preferentially forms in or migrates to larger pores on a laboratory timescale and is predominantly found in coarse-grained sediment, the hydrate behaves like a non-wetting phase.

Although less common than two-phase systems, there have been numerous discoveries of hydrate reservoirs where three phases (gas, water, and hydrate) can co-exist (e.g. Milkov et al., 2004). These three-phase zones can also play a crucial role in reservoir production models (You et al., 2019). We propose that our model of relative permeability can be expanded to three-phase systems with gas, water, and hydrate. Based on the same energy argument as the two-phase system, water will fill the small pores (Clennell et al., 1999), and gas and hydrate will compete for the larger pores in such a way as to minimize interfacial energy. The three-phase water relative permeability may be predicted using two-phase measurements since the water will always flow through the smallest pores, and gas and hydrate will occupy the largest pores. Three-phase gas relative permeability may be the same as two-phase gas relative permeability (assuming that gas will be restricted to the largest pores based on the relative magnitudes of the gas-water and hydrate-water interfacial energies), but both need to be verified by experiments. The three-phase argument presented here is for an ideal, thermodynamically stable system. However, we are unsure if laboratory or natural systems will ever reach this thermodynamic stability.

2.6 CONCLUSIONS

We successfully measured the relative permeability of water in a Berea Sandstone core in the presence of gas and in the presence of a range of hydrate saturations. The experiments show that the relative permeability in the hydrate/water system behaves the same as in a gas/water system. These results suggest that hydrate adopts a non-wetting behavior preferentially filling the larger pores. Therefore, water relative permeability for a hydrate system is best derived through simpler gas/water relative permeability experiments in the same porous medium. We suggest that hydrate non-wetting model may be extended to three-phase relative permeability in hydrate/gas/water systems.

2.7 REFERENCES

Archer, D., Buffett, B. A., & Brovkin, V. (2008). Ocean methane hydrates as a slow tipping point in the global carbon cycle. *Proceedings of the National Academy of Sciences*, *106*(49), 20596-20601. https://doi.org/10.1073/pnas.0800885105

Blunt, M. J. (2017). *Multiphase Flow in Permeable Media: A Pore-Scale Perspective*. Cambridge University Press. https://doi.org/10.1017/9781316145098

Boswell, R. (2009). Is gas hydrate energy within reach? *Science*, *325*(5943), 957-958. https://doi.org/10.1126/science.1175074

Boswell, R., & Collett, T. (2011). Current prospective on gas hydrate resources. *Energy & Environmental Science*, *4*, 10.

Brooks, R. H., & Corey, A. T. (1964). Hydraulic Properties of Porous Media. *Hydrology Papers*.

Chen, X., & Espinoza, D. N. (2018). Ostwald ripening changes the pore habit and spatial variability of clathrate hydrate. *Fuel*, *214*, 614-622. https://doi.org/10.1016/j.fuel.2017.11.065

Chen, X., Espinoza, D. N., Luo, J. S., Tisato, N., & Flemings, P. B. (2020). Pore-scale evidence of ion exclusion during methane hydrate growth and evolution of hydrate pore-habit in sandy sediments. *Marine and Petroleum Geology*, *117*. https://doi.org/10.1016/j.marpetgeo.2020.104340

Chen, X., Kianinejad, A., & A. DiCarlo, D. (2017). Measurements of CO2-brine relative permeability in Berea sandstone using pressure taps and a long core. *Greenhouse Gases: Science and Technology*, *7*(2), 370-382. https://doi.org/10.1002/ghg.1650

Clennell, M. B., Hovland, M., Booth, J. S., Henry, P., & Winters, W. J. (1999). Formation of natural gas hydrates in marine sediments 1. Conceptual model of gas hydrate growth conditioned by host sediment properties. *Journal of Geophysical Research*, *104*(B10), 22985-23003. https://doi.org/10.1029/1999jb900175

Cook, A. E., & Malinverno, A. (2013). Short migration of methane into a gas hydrate-bearing sand layer at Walker Ridge, Gulf of Mexico. *14*(2), 283-291. https://doi.org/10.1002/ggge.20040

Dai, S., Santamarina, J. C., Waite, W. F., & Kneafsey, T. J. (2012). Hydrate morphology: Physical properties of sands with patchy hydrate saturation. *Journal of Geophysical Research: Solid Earth*, *117*(B11), B11205. https://doi.org/10.1029/2012JB009667

Daigle, H. (2016). Relative permeability of hydrate-bearing sediments from critical path analysis. *Journal of Petroleum Science and Engineering*.

Darnell, K. N., Flemings, P. B., & DiCarlo, D. (2019). Nitrogen-Driven Chromatographic Separation During Gas Injection Into Hydrate-Bearing Sediments. *Water Resources Research*. https://doi.org/10.1029/2018wr023414

Dickens, G. R., O'Neil, J. R., Rea, D. K., & Owen, R. M. (1995). Dissociation of oceanic methane hydrate as a cause of the carbon isotope excursion at the end of the Paleocene. *Paleoceanogr.*, *10*, 965-971.

Jang, J., & Santamarina, J. (2014). Evolution of gas saturation and relative permeability during gas production from hydrate-bearing sediments: gas invasion vs. gas nucleation. *Journal of Geophysical Research Solid Earth*, *119*, 116-126. https://doi.org/https://doi.org/10.1002/2013JB010480

Kleinberg, R. L., Flaum, C., Griffin, D. D., Brewer, P. G., Malby, G. E., Peltzer, E. T., & Yesinowski, J. P. (2003). Deep sea NMR: Methane hydrate growth habit in porous media and its relationship to hydraulic permeability, deposit accumulation, and submarine slope stability. *Journal of Geophysical Research: Solid Earth*, *108*(B10), 2508. https://doi.org/10.1029/2003JB002389

Koh, D.-Y., Kang, H., Lee, J.-W., Park, Y., Kim, S.-J., Lee, J., Lee, J. Y., & Lee, H. (2016). Energy-efficient natural gas hydrate production using gas exchange. *Applied Energy*, *162*(Supplement C), 114-130. https://doi.org/https://doi.org/10.1016/j.apenergy.2015.10.082

Konno, Y., Fujii, T., Sato, A., Akamine, K., Naiki, M., Masuda, Y., Yamamoto, K., & Nagao, J. (2017). Key Findings of the World’s First Offshore Methane Hydrate Production Test off the Coast of Japan: Toward Future Commercial Production. *Energy & Fuels*, *31*(3), 2607-2616. https://doi.org/10.1021/acs.energyfuels.6b03143

Lake, L. W. (1989). *Enhanced oil recovery*. Prentice Hall. https://books.google.com/books?id=nm5MAQAAIAAJ

Lei, L., Seol, Y., Choi, J.-H., & Kneafsey, T. J. (2019). Pore habit of methane hydrate and its evolution in sediment matrix – Laboratory visualization with phase-contrast micro-CT. *Marine and Petroleum Geology*, *104*, 451-467. https://doi.org/10.1016/j.marpetgeo.2019.04.004

Lei, L., Seol, Y., & Myshakin, E. M. (2019). Methane Hydrate Film Thickening in Porous Media. *Geophysical Research Letters*, *46*(20), 11091-11099. https://doi.org/10.1029/2019gl084450

Liu, X., & Flemings, P. B. (2006). Passing gas through the hydrate stability zone at southern Hydrate Ridge, offshore Oregon. *Earth and Planetary Science Letters*, *241*(1–2), 211-226. https://doi.org/doi:10.1016/j.epsl.2005.10.026

Liu, X., & Flemings, P. B. (2011). Capillary effects on hydrate stability in marine sediments. *Journal of Geophysical Research-Solid Earth*, *116*(B07102), 24. https://doi.org/10.1029/2010jb008143

Mahabadi, N., Dai, S., Seol, Y., & Jang, J. (2019). Impact of hydrate saturation on water permeability in hydrate-bearing sediments. *Journal of Petroleum Science and Engineering*, *174*, 696-703. https://doi.org/https://doi.org/10.1016/j.petrol.2018.11.084

Malinverno, A. (2010). Marine gas hydrates in thin sand layers that soak up microbial methane. *Earth and Planetary Science Letters*, *292*(3-4), 399-408. https://doi.org/10.1016/j.epsl.2010.02.008

Milkov, A. V., Dickens, G. R., Claypool, G. E., Lee, Y.-J., Borowski, W. S., Torres, M. E., Xu, W., Tomaru, H., Tréhu, A. M., & Schultheiss, P. (2004). Co-existence of gas hydrate, free gas, and brine within the regional gas hydrate stability zone at Hydrate Ridge (Oregon margin): evidence from prolonged degassing of a pressurized core. *Earth and Planetary Science Letters*, *222*(3–4), 829-843. https://doi.org/http://dx.doi.org/10.1016/j.epsl.2004.03.028

Moridis, G. J., Reagan, M. T., Kim, S.-J., Seol, Y., & Zhang, K. (2007). Evaluation of the Gas Production Potential of Marine Hydrate Deposits in the Ulleung Basin of the Korean East Sea. In.

Moridis, G. J., Reagan, M. T., Queiruga, A. F., & Boswell, R. (2019). Evaluation of the performance of the oceanic hydrate accumulation at site NFHP-02-09 in the Krishna-Godavari Basin during a production test and during single and multi-well production scenarios. *Marine and Petroleum Geology*, *108*, 660-696. https://doi.org/10.1016/j.marpetgeo.2018.12.001

Myshakin, E. M., Seol, Y., Lin, J.-S., Uchida, S., Collett, T. S., & Boswell, R. (2019). Numerical simulations of depressurization-induced gas production from an interbedded turbidite gas hydrate-bearing sedimentary section in the offshore India: Site NGHP-02-16 (Area-B). *Marine and Petroleum Geology*, *108*, 619-638. https://doi.org/10.1016/j.marpetgeo.2018.10.047

Nole, M., Daigle, H., Cook, A. E., & Malinverno, A. (2016). Short-range, overpressure-driven methane migration in coarse-grained gas hydrate reservoirs. *Geophysical Research Letters*, *43*, 9500-9508. https://doi.org/10.1002/2016GL070096

Phillips, S. C., Flemings, P. B., Holland, M. E., Schultheiss, P., Waite, W. F., Jang, J., Petrou, E. G., & Helen, H. (2020). High concentration methane hydrate in a silt reservoir from the deep-water Gulf of Mexico. *AAPG Bulletin*, *104*(9), 1971-1995. https://doi.org/https://doi.org/10.1306/01062018280

Phillips, S. C., Flemings, P. B., You, K., Meyer, D. W., & Dong, T. (2019). Investigation of in situ salinity and methane hydrate dissociation in coarse-grained sediments by slow, stepwise depressurization. *Marine and Petroleum Geology*, *109*, 128-144. https://doi.org/10.1016/j.marpetgeo.2019.06.015

Priest, J. A., Rees, E. V. L., & Clayton, C. R. I. (2009). Influence of gas hydrate morphology on the seismic velocities of sands. *Journal of Geophysical Research: Solid Earth*, *114*(B11), B11205. https://doi.org/10.1029/2009JB006284

Spangenberg, E. (2001). Modeling of the influence of gas hydrate content on the electrical properties of porous sediments. *Journal of Geophysical Research: Solid Earth*, *106*(B4), 6535-6548. https://doi.org/10.1029/2000JB900434

van Genuchten, M. T. (1980). A Closed-form Equation for Predicting the Hydraulic Conductivity of Unsaturated Soils. *Soil Science Society of America Journal*, *44*(5), 892-898. https://doi.org/10.2136/sssaj1980.03615995004400050002x

Waite, W. F., Santamarina, J. C., Cortes, D. D., Dugan, B., Espinoza, D. N., Germaine, J., Jang, J., Jung, J. W., Kneafsey, T. J., Shin, H., Soga, K., Winters, W. J., & Yun, T. S. (2009b). Physical properties of hydrate-bearing sediments. *Reviews of Geophysics*, *47*(4), RG4003. https://doi.org/10.1029/2008rg000279

You, K., Flemings, P. B., Malinverno, A., Collett, T. S., & Darnell, K. (2019). Mechanisms of Methane Hydrate Formation in Geological Systems. *Reviews of Geophysics*, *0*(ja). https://doi.org/https://doi.org/10.1029/2018rg000638

Chapter 3: Gas and water relative permeability in CH_4 hydrate systems

3.1 ABSTRACT

[2]We introduce a new approach to predict the gas and water flow properties of methane hydrate-bearing sediments. Previous models of relative permeability, based on heuristic concepts like "pore filling" or "grain coating," do not accurately represent the complex nature of geologic media and overlook three-phase scenarios involving gas, water, and hydrate. In contrast, our approach is grounded in thermodynamics, specifically the phase occupancy of pores. We conduct gas and water flow experiments with and without hydrate, comparing the results to both our physical model and existing models. We show that the flow properties of gas and water in the presence of hydrate can be determined using measurements from sediment without hydrate.

3.2 INTRODUCTION

At high pressures and low temperatures, water and methane will form hydrates that occupy the pore space of coarse-grained sediments (Sloan & Koh, 2007). The presence of hydrate will reduce the permeability (relative permeability) of the sediment to gas or water (e.g., Kleinberg et al., 2003; Liu & Flemings, 2011; Waite et al., 2009b). This behavior has long been recognized, and many models and measurements of permeability reduction

---

[2] This chapter was submitted to Transport in Porous Media in October 2023. The paper is under review as of 10/23/2023.
I conceived and designed this study, performed the experiments, gathered the data, conducted the analysis, made the figures, and wrote the manuscript. David DiCarlo, Kehua You, and Peter Flemings edited the manuscript for clarity and provided valuable feedback on the manuscript contents.

caused by hydrate have been undertaken (e.g., Boswell, 2009; Konno et al., 2017; Moridis, Kowalsky, et al., 2007).

Most of the models (Moridis, Kowalsky, et al., 2007; White et al., 2020) and measurements (Dai & Seol, 2014; Kneafsey et al., 2011; Murphy et al., 2020; Yoneda et al., 2019) have been on systems that contain only two-phases – hydrate with water or gas. Here we focus on how both water and gas flow in the presence of hydrates in coarse porous media. This three-phase (gas, water, and hydrate) scenario is common and relevant; it drives the formation of deposits with high hydrate saturations near the base of the hydrate stability zone (Nole et al., 2018; You & Flemings, 2021), and is crucial for modeling any production scenario (Moridis, Kowalsky, et al., 2007; White et al., 2020).

In terms of measurements of gas and water relative permeability in the presence of hydrates, these limited works have focused on unsteady state experiments (Jaiswal et al., 2009) or have faced experimental challenges where limited measurements were made (Johnson et al., 2011). These works highlight the challenges of conducting three-phase flow experiments and the importance of all three phase saturations on relative permeability.

In terms of models of gas and water relative permeability in the presence of hydrates, two main ideas have been proposed. The evolving porous medium (EPM) model considers hydrate to be like any other precipitated solid phase. This changes the pore structure of the medium (i.e., it evolves), with a change in permeability (Moridis et al., 2005; White et al., 2020). The water and gas move within this evolved porous medium, and for simplicity, the functional forms of the water and gas are taken to be the same as for the medium without hydrate. Alternatively, the original porous medium (OPM) model considers hydrate to take up positions in the porous medium similar to that of a liquid phase (Moridis, Kowalsky, et al., 2007; White et al., 2020). The pore structure does not change (i.e., original), and the permeability to gas and water are estimated from the two-phase permeabilities.

The pore habit of hydrate will determine which type of model will more closely represent reality. Field observations have shown that very high hydrate saturations are found in coarse sediments adjacent to finer sediments with no hydrate saturation (Fang et al., 2020; Lei et al., 2022), and laboratory measurements have found that hydrate that nucleates at the water/gas interface will disintegrate and reform in the center of pores on the time scale of days (Chen et al., 2020). These observations are consistent with rapid Ostwald ripening of the hydrate, which effectively causes the hydrate to emplace itself as a non-wetting phase in the porous medium (Chen & Espinoza, 2018; Murphy et al., 2020).

Here, we use this idea to obtain gas and water relative permeability in the presence of hydrate from two-phase gas and water measurements without hydrate. We present two scenarios for how hydrate behaves in a three-phase system: 1) the hydrate acts as the least-wetting phase and 2) the hydrate acts as the intermediate-wetting phase. We obtain functional forms for the relative permeability and capillary pressure for both scenarios and discuss at which pressure and temperature conditions each scenario is likely to be valid.

We first measure water and gas relative permeability in a sandstone core in the presence of hydrate. We then compare these measurements to these above scenarios as well as widely-used heuristic models. We find that the new model matches the gas and water relative permeabilities in the presence of hydrates by only using measured gas and water relative permeabilities without hydrate. The latter are much easier to measure, suggesting that we can derive both three-phase relative permeability and three-phase capillary pressure curves for hydrate-bearing sediment from two-phase experiments.

3.3 MODEL DEVELOPMENT

We begin by reviewing how the pore occupancy of fluids in two-phase systems results in certain two-phase flow properties. This is then extended to three-phase (gas/water/hydrate) systems. We concentrate on coarse-grained systems where the grains, and thus the structure of the porous medium, are fixed. The resulting pore space can be conceptualized as a broad distribution of irregularly shaped large openings (pores) connected by a broad distribution of irregularly shaped smaller openings (throats). This pore space is unique to each porous medium.

In multiphase systems, each phase (i) will occupy a fraction of the pore space, which is defined as saturation,

$$S_i = \frac{V_i}{V_p}, \tag{1}$$

where S_i is saturation of phase i, V_i is the volume of phase i, and V_p is the pore volume. If there are two phases in the medium (e.g., gas and water), the total saturation must sum to one,

$$S_w + S_g = 1. \qquad (2)$$

The surface energy between the phases determines the pore scale emplacement of the fluid phases. Most important is the energy associated with fluid/solid interactions. In mineral sediments, the solid/water interfacial tension (IFT) is much lower than the solid/gas IFT, and thus water wets all of the solid surfaces, and is known as the wetting phase (e.g., Blunt, 2017; Henry et al., 1999).

The fluids will position themselves to minimize the gas/water interfacial area within the confines of the geometry of the porous medium. This is achieved by gas emplacing itself in the largest pores, as this achieves less gas/water interface than dividing up the same volume of gas in smaller pores. With increasing gas saturation, the gas enters smaller and smaller pores, increasing the curvature of the gas/water interface. This curvature causes a pressure difference between the phases - the capillary pressure - which is proportional to the interfacial tension between the phases. For two-phase (2ϕ) gas/water systems the capillary pressure is related to the saturation through,

$$P_c^{2\Phi}(\mathrm{S_w}) = \mathrm{P_g} - \mathrm{P_w} = \sigma_{\mathrm{gw}}\mathrm{J}^*(\mathrm{S_w}), \qquad (3)$$

where $P_c^{2\phi}$ is the two-phase capillary pressure, σ_{gw} is the interfacial energy between gas and water, and J^* is a non-linear function to describe the relationship between interface curvature and water saturation that depends on the pore-size distribution and connectivity of the particular porous media (Bear, 1972).

Importantly, the pore occupancy controls how each phase flows through the porous media. Generally, as the saturation of a given phase is reduced, the effective permeability of that phase is reduced. The ratio of the effective permeability ($\mathrm{k_{eff}}$) to the intrinsic permeability ($\mathrm{k_0}$) is the relative permeability ($\mathrm{k_r}$),

$$\mathrm{k_r} = \frac{\mathrm{k_{eff}}}{\mathrm{k_0}}. \tag{4}$$

Every porous medium has a unique geometry controlled by geology (parent material, depositional environment, diagenesis, etc.), and thus the shape of the relative permeability curves will be unique to each porous medium (Blunt, 2017).

Figure 8 shows relative permeability data measured for a gas/water system in a Berea sandstone. Also shown are fits to the data using a Brooks and Corey (1964) fit where the two-phase water ($k_{rw}^{2\phi}$) and gas ($k_{rg}^{2\phi}$) relative permeability are modeled by:

$$\mathrm{k_{rw}^{2\Phi}(S_w)} = \left(\frac{\mathrm{S_w - S_{wr}}}{\mathrm{1 - S_{wr}}}\right)^{\mathrm{n_w}}, \tag{5}$$

$$k_{rg}^{2\Phi}(S_g) = \left(\frac{S_g - S_{gr}}{1 - S_{gr}}\right)^{n_g}, \tag{6}$$

where S_{wr} is residual water saturation, S_{gr} is residual gas saturation, and n_w and n_g are the gas and water fitting parameters.

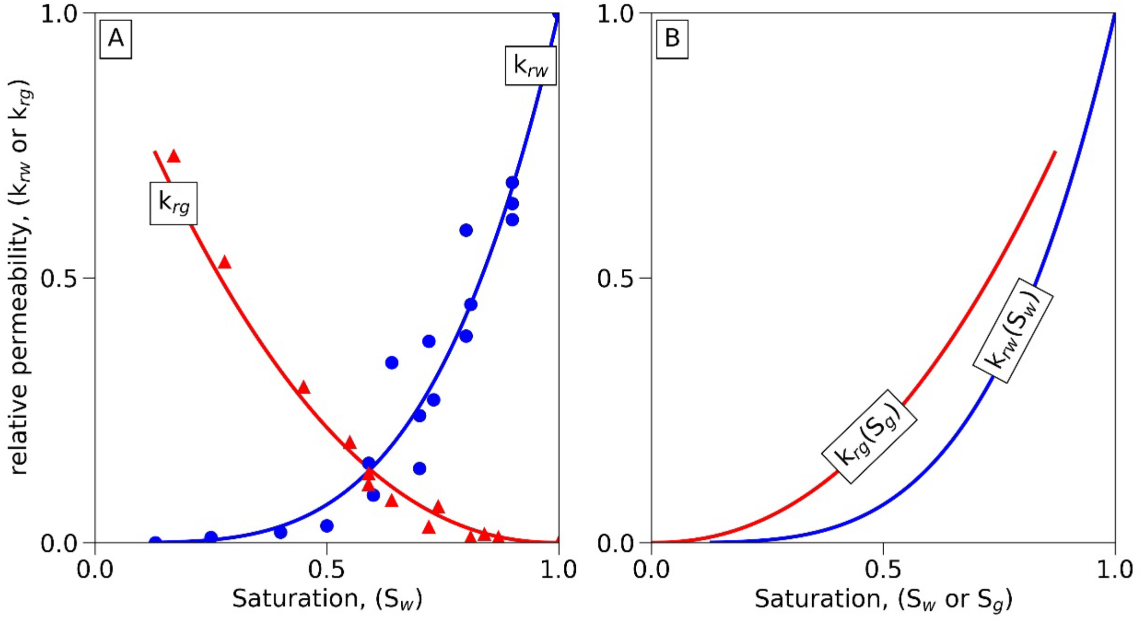

Figure 8. A) Two-phase (gas-water) relative permeability as function of water saturation. Water (blue dots) and gas (red triangle) are experimental data measured in a Berea Sandstone with the steady-state method (Murphy et al., 2020). A Brooks-Corey model (equation 2 and 3) are fit to the data (n_w=3.8, n_g=2.2, S_{wr}=0, S_{gr}=0). B) The Brooks-Corey models from A are presented as a function of the relevant saturation $k_{rw}^{2\phi}(S_w)$ and $k_{rg}^{2\phi}(S_g)$.

As seen in Figure 8, the water relative permeability decreases faster with decreasing water saturation than the gas relative permeability with gas saturation. This is because the largest pore spaces are the best conduits for fluid flow, and the large pores are the first to empty of water for decreasing water saturation, and the last to empty of gas for decreasing gas saturation. These concepts are valid for any non-wetting/wetting pairs in porous media. For a hydrate/water system or a gas/water system, water will be the wetting phase, and gas or hydrate will be the non-wetting phase (Murphy et al., 2020).

We extend the concepts from the two-phase discussion above to three-phase systems. We borrow liberally from the petroleum literature, as many reservoirs consist of a three-phase gas/oil/water system (Blunt, 2017). As hydrate occupies a portion of the pore space, the hydrate phase will have its own saturation. There are now three saturations, with two of them being independent with the constraint,

$$\mathrm{S_w} + \mathrm{S_g} + \mathrm{S_h} = 1. \tag{7}$$

Energetically, there is a most-wetting phase, a least-wetting phase, and an intermediate-wetting phase. In water/hydrate/gas systems, water will act as the wetting phase (Murphy et al., 2020). Therefore, gas and hydrate will compete for the larger pores. Liu and Flemings (2011) and others have proposed that hydrate and gas will split occupancy of the largest pores. However, recent work suggests that the phase with the higher CH_4 density will be the least-wetting phase (DiCarlo et al., 2023; in review). In a companion paper, we give the thermodynamic argument on how the expected gas and hydrate pore occupancy changes based on depth. Therefore, we examine both situations where 1) hydrate is the least-wetting phase and 2) hydrate is the intermediate-wetting phase. Since hydrate behaves as fluid phase, these models can be classified as OPM models (Moridis, Kowalsky, et al., 2007). We explore the implications on relative permeability and capillary pressure for both scenarios as well as commonly used models in the following sections.

3.3.1 Hydrate least-wetting phase

We examine the implications for flow (relative permeability) in a reservoir where hydrate will preferentially exist in the largest pores (least-wetting) and gas will occupy the intermediate-sized pores (Figure 9A). We refer to this model as the three-phase least model (abbreviated as *3ϕ-least*) since hydrate will act as the least-wetting phase in this three-phase conceptualization.

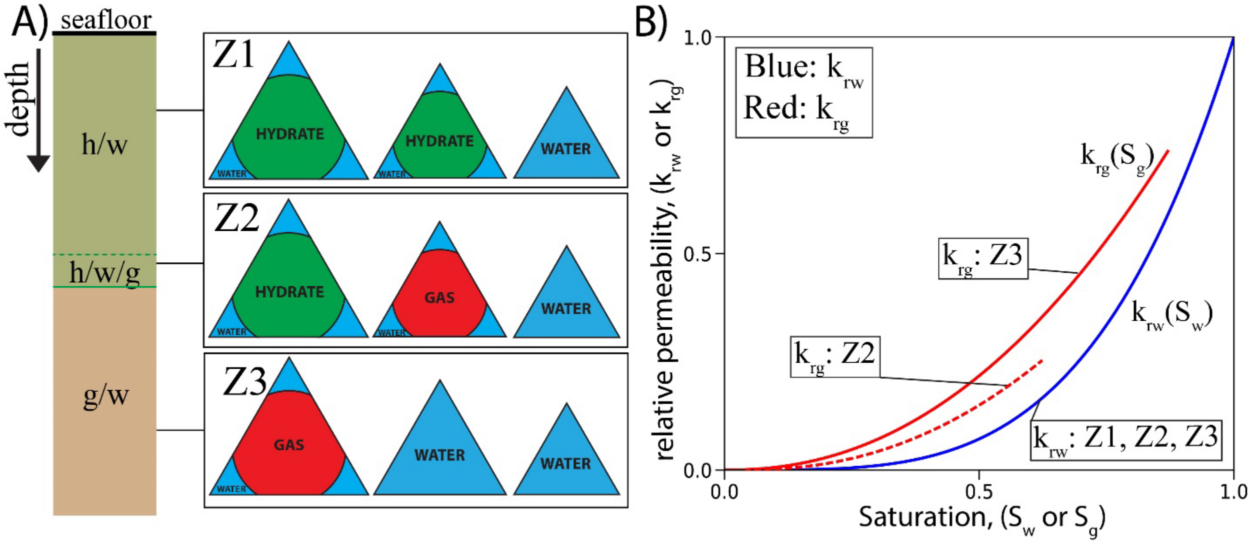

Figure 9. A) Water, gas, and hydrate pore occupancy in distribution of pore sizes with hydrate as least-wetting phase. These cartoons use triangular pores, as pores within porous media are not spherical. At all depths, water is the wetting phase. At depth Z1, hydrate is the non-wetting phase. At depth Z2, hydrate will be the least-wetting phase (big pores) and gas will be the intermediate phase. At depth Z3, gas is the non-wetting phase. B) Relative permeability of gas and water in the presence of hydrate. Blue line is water relative permeability for all depths. Solid red line is the two-phase gas relative permeability at depth Z3. The dashed red line is the gas relative permeability at depth Z2 (*3ϕ-least*). The gas is the intermediate phase and therefore the relative permeability is interpolated between the water (blue) and gas (red) based on the hydrate and water saturation (eq. 9).

The most-wetting phase in the three-phase system will position itself in the same pores as the wetting phase in the two-phase system for a particular saturation. Thus, the three-phase (3ϕ) water relative permeability case will behave the same as the wetting case for the two-phase system (Murphy et al., 2020),

$$\mathrm{k_{rw}^{3\phi}(S_w, S_h) = k_{rw}^{2\phi}(S_w)}. \tag{8}$$

The intermediate-wetting phase will not have a two-phase equivalent. However, the limits are known. If the saturation of the least-wetting phase goes to zero, then the intermediate-wetting phase will behave as the non-wetting phase. If the saturation of the most-wetting phase goes to zero, the intermediate-wetting phase behaves as the wetting phase. If not at the limit, many models have been proposed to estimate the relative permeability of the intermediate phase (Eleri et al., 1995; Kralik et al., 2000; Oak, 1991). The simplest - a linear interpolation between the two end members – is called saturated weighted interpolation (SWI), which gives a three-phase gas relative permeability of (Baker, 1988):

$$k_{rg}^{3\phi}(S_g, S_h) = \left(\frac{S_h}{1-S_g}\right) k_{rw}^{2\phi}(S_g) + \left(1 - \frac{S_h}{1-S_g}\right) k_{rg}^{2\phi}(S_g). \tag{9}$$

Note that this is a weighted average of the two-phase gas and water relative permeability but with the gas saturation input into these relative permeabilities. In the limit that $S_h = 0$, the three-phase gas relative permeability is given by the two-phase gas relative permeability curve (Figure 9B, red line); in the limit $S_w = 0$ (i.e. $\mathrm{S_h} = 1 - \mathrm{S_g}$), the three-phase gas relative permeability is given by the water relative permeability curve (at that gas saturation) (Figure 9B, blue line).

Finally, the least-wetting hydrate phase should have a non-wetting phase relative permeability, but since the hydrate does not flow as a fluid, any discussions of hydrate relative permeability are immaterial.

In addition to the relative permeability, the curvatures between the phases give the three-phase capillary pressures ($P_c^{3\Phi}$):

$$P_{cgw}^{3\Phi} = P_g - P_w = \sigma_{gw} J^*(S_w), \tag{10}$$

$$P_{chw}^{3\Phi} = P_h - P_w = \sigma_{hw} J^*(1 - S_h). \tag{11}$$

Here the gas/water curvature is set by the water saturation, and the hydrate/water curvature is set by the sum of the gas and water saturations.

We predict hydrate will be the least-wetting phase at conditions where P< 14.2 MPa due to the thermodynamic arguments presented in DiCarlo et al. (2023; in review).

3.3.2 Hydrate is intermediate-wetting phase

We next explore the scenario where gas will preferentially exist in the largest pores (least-wetting) and hydrate will occupy the intermediate-sized pores (Figure 10A). We refer to this as the three-phase intermediate model (abbreviated as *3ϕ-int*) since hydrate will act as the intermediate-wetting phase.

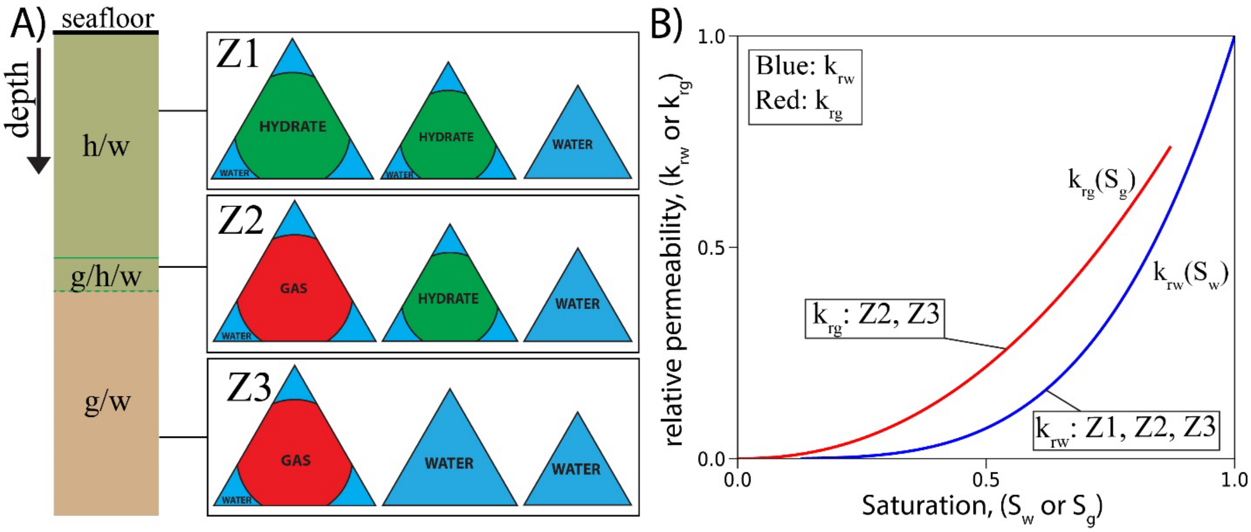

Figure 10. A) Water, gas, and hydrate pore occupancy when gas is the least-wetting phase. Z1 and Z3 are the same as Figure 9. At Z2, gas will be the least-wetting phase and hydrate will be the intermediate-wetting phase. B) Relative permeability of gas and water in the presence of intermediate-wetting hydrate. The water relative permeability is unchanged. Since gas is always the least wetting phase (with or without hydrate), the gas relative permeability (red line) is the same for two-phase or three-phase conditions (eq. 12).

Again, as water is the most-wetting phase, the three-phase water relative permeability will be the same as the previous case (eq. 8). The intermediate-wetting hydrate phase does not flow as a fluid, and thus any discussions of hydrate relative permeability are immaterial.

Similar to the wetting-phase, the three-phase least-wetting phase will position itself in the same pores as the two-phase non-wetting phase at the same saturation. Again, the connections, interface curvature, and relative permeability of the three-phase least-wetting phase will behave the same as the two-phase non-wetting case. As gas is the least-wetting phase, the three-phase gas relative permeability is the same as the two-phase gas relative permeability,

$$k_{rg}^{3\phi}(S_g, S_h) = k_{rg}^{2\phi}(S_g). \tag{12}$$

In addition to the relative permeability, the curvatures between the phases give the three-phase capillary pressures,

$$P_{cgw}^{3\phi} = P_g - P_w = \sigma_{gw} J^*(1 - S_g), \tag{13}$$

$$P_{chw}^{3\phi} = P_h - P_w = \sigma_{hw} J^*(S_w). \tag{14}$$

Here the gas/water curvature is set by sum of the water and hydrate saturation, and the hydrate/water curvature is set by the water saturations.

Thermodynamic arguments predict that hydrate will be the intermediate-wetting phase if the pressure is greater than 14.2 MPa (DiCarlo et al., 2023; in review).

3.3.3 Solid model

A previous and commonly used model for gas and water flow in the presence of hydrate assumes that hydrate forms like a precipitated solid phase and thus is just part of the mineral matrix (EPM model; Moridis, Kowalsky, et al., 2007). In practical terms, hydrate creates a reduction of effective porosity (ϕ^*),

$$\phi^* = (1 - S_h)\phi, \tag{15}$$

where ϕ is the porosity (Kleinberg et al., 2003; Liu & Flemings, 2006; Moridis et al., 2019). There is a corresponding reduction in the permeability to the fluid phases, which is a function of the hydrate saturation, $k(S_h)$. This model has also been called the evolving porous media (EPM) model (Moridis, Kowalsky, et al., 2007). Heuristic models have been proposed to describe the reduced permeability in these situations. The widely used models are termed 'pore filling' or 'grain coating' and result in different functional forms (Delli & Grozic, 2014; Katagiri et al., 2017; Kleinberg et al., 2003).

Because these models treat the hydrate as a precipitated solid phase, we define this approach as the *solid model*. In the case of gas/water relative permeability in the presence of hydrate, the solid model first apportions the remaining pore space between the water and gas phases leading to “effective” saturations,

$$S_w^* = \frac{S_w}{1-S_h}, \tag{16}$$

$$S_g^* = \frac{S_g}{1-S_h}. \tag{17}$$

These effective saturations are then used as inputs to the two-phase relative permeability curves. Putting it all together, the solid model gives the three-phase relative permeabilities of gas and water in the presence of hydrate,

$$k_{rw}^{3\phi} = k_{rw}^{2\phi}(S_w^*)k(S_h), \tag{18}$$

$$k_{rg}^{3\phi} = k_{rg}^{2\phi}(S_g^*)k(S_h). \tag{19}$$

In terms of capillary pressure in the presence of hydrate, the standard scaling of the square root of the ratio of porosity to permeability is used (Liu & Flemings, 2011; Moridis, Kowalsky, et al., 2007).

$$P_{cgw}^{3\phi} = P_g - P_w = \sigma_{gw}J(S_w^*)\sqrt{\frac{(1-S_h)\phi}{k(S_h)}} \tag{20}$$

Numerous models to predict reductions in permeability due to hydrate formation have been built under this concept and most flow simulators of hydrate systems use this model (Kleinberg et al., 2003; Liu & Flemings, 2011; Moridis et al., 2019; You & Flemings, 2018).

3.3.4 Model comparison

In Figure 11, we plot the models presented above at two different hydrate saturations (S_h=0.3 and 0.6). The fitting parameters for all models are from the measured two-phase data from Figure 8. Both three-phase models predict the water relative permeability to be the same as the measured two-phase data with different end values of S_w that are controlled by the hydrate saturation. The three-phase gas relative permeability is controlled by the pore occupancy – hydrate as intermediate-wetting phase or hydrate as least-wetting phase. The three-phase intermediate model is the same as the two-phase fit since gas will be the least-wetting phase in both cases. However, the three-phase least model is a saturation weighted interpolation between the two-phase fit for water and gas. Also shown are solid models for gas and water. The solid-grain model generally predicts a higher relative permeability because the hydrate occupies/blocks the small pores, and the gas and water then flow through the larger pores. In contrast, the solid-pore model predicts a lower relative permeability because the larger pores are blocked with hydrate and the fluids flow through the small pores.

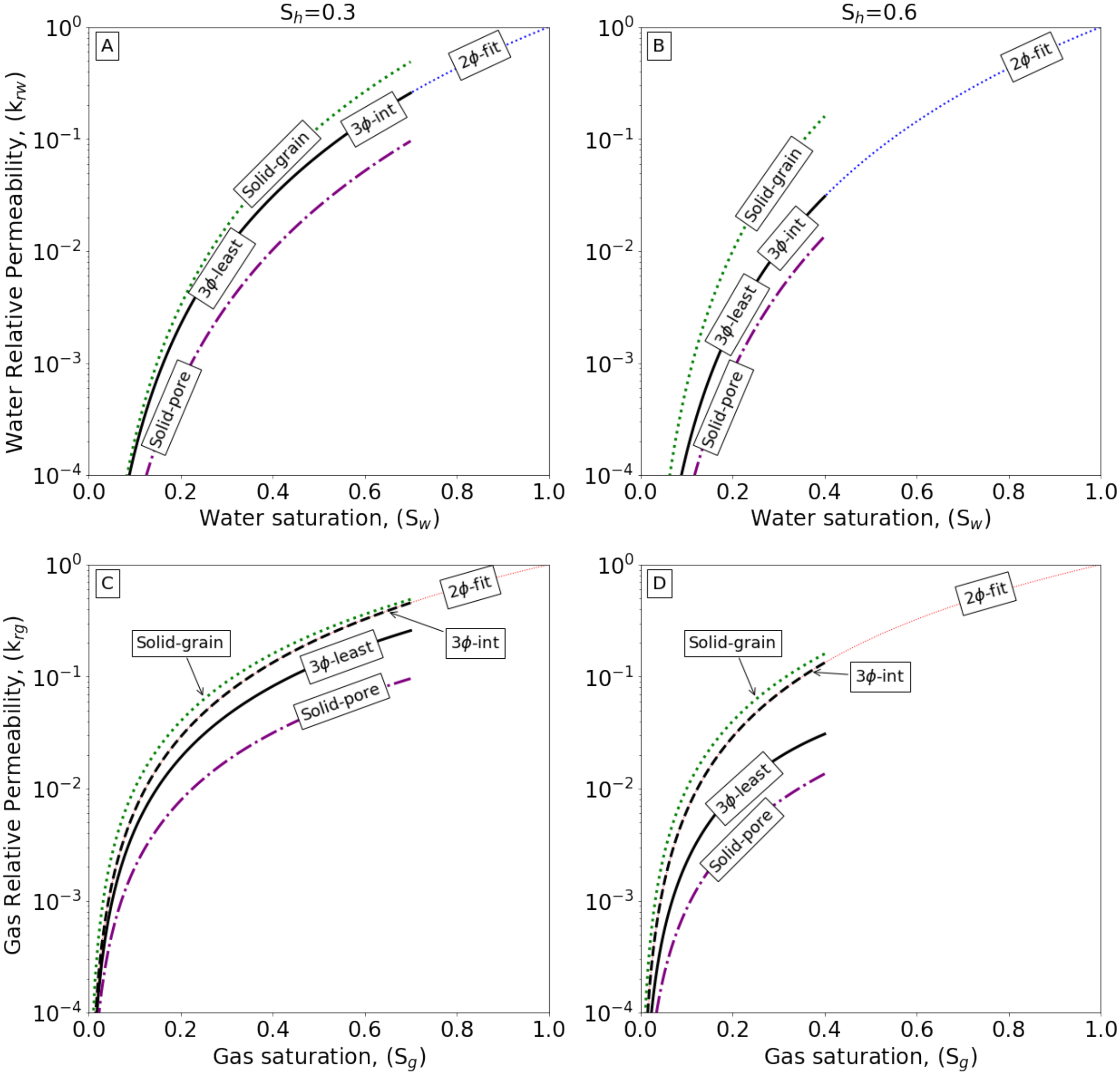

Figure 11 Comparison of models at different hydrate saturations. In all figures, we show the 2ϕ fit (red/blue line), 3ϕ-least (black solid line), 3ϕ-int (black dashed line), solid-pore (purple dash-dot line), and solid-grain (green dot line). A) Water relative permeability as function of water saturation with a hydrate saturation of 0.3. B) Gas relative permeability as function of gas saturation with a hydrate saturation of 0.3. C) Water relative permeability as function of water saturation with a hydrate saturation of 0.6. D) Gas relative permeability as function of gas saturation with a hydrate saturation of 0.6.

3.4 EXPERIMENTS

We measure steady-state gas-water relative permeability in both hydrate free and hydrate-bearing cores. We use a Berea sandstone core (length: 55 cm, diameter: 3.8 cm) with a measured bulk porosity of 0.22. The core is placed in a core holder with 5 pressure taps spaced 4 cm apart that are connected to differential pressure transducers (Murphy et al., 2020). The pressure taps are necessary to reduce the influence of capillary end effects (Chen et al., 2017).

We first measure gas/water relative permeability using the method and system used by Murphy et al. (2020). The core is saturated with brine (3.5wt% NaCl) and the single-phase permeability is measured by flowing brine and measuring the pressure drop across each section. Gas/water relative permeability is then obtained by co-injecting gas at a specified fractional flow rate of water (f_w),

$$f_w = \frac{Q_w}{Q_w + Q_g}, \tag{21}$$

where Q_w is the flow rate of water and Q_g is the flow rate of gas. At each fractional flow rate, we reach steady state and the internal pressure drops are recorded. Steady state is determined when the pressure drop remains constant ($\Delta P < 1\text{kPa}$). The saturation of each phase is determined based on mass balance at each fractional flow rate. The relative permeability is calculated using the Darcy-Buckingham equation for each phase (i),

$$k_{r(i)} = -\left(\frac{Q_i \cdot \mu_i}{k_{abs} \cdot A}\right) \cdot \left(\frac{L}{\Delta P}\right), \tag{22}$$

where Q_i is the flow rate of phase i, μ_i is the viscosity of phase i, A is the cross-sectional area, L is the length between pressure taps, and ΔP is the pressure drop along length L. The gas/water experiments were replicated multiple times to account for the variability in relative permeability measurements (Figure 8).

To measure gas and water relative permeability in the presence of hydrate, we next form hydrate in the same Berea Sandstone core using the high-water saturation method (Murphy et al., 2020). The high saturation method begins with a fully brine-saturated core. Methane gas is then injected until the water saturation decreases to approximately 75%. The system is then shut-in, and methane gas is injected with a syringe pump until the sample reaches ~8.5 MPa. Gas is injected to maintain a constant pore pressure throughout the entire experiment, and the amount of gas injected is recorded by the pump. The system is then cooled to 6°C and held constant for the entire experiment as the system enters the hydrate stability zone. Hydrate nucleation occurs after ~10 hours, and hydrate formation is allowed to continue until the desired hydrate saturation is reached (~14 days). We calculate the final hydrate saturation using the mass balance analysis from Murphy et al. (2020). This formation method is described in detail in Murphy et al. (2020) and is adapted from You et al. (2015) and Meyer et al. (2018).

To measure the gas/water relative permeability in the hydrate-bearing sample, a similar procedure to the hydrate-free sample is followed. We use high salinity brine (~13wt% NaCl) that is close to the three-phase stability boundary to prevent additional hydrate formation (You et al., 2015). We then flow the brine through the core $\big(\mathrm{f_w} =$

$1, \mathrm{f_g} = 0\big)$ and measure the water effective permeability $\big(\mathrm{k_{eff,w}}\big)$ in the presence of hydrate (Murphy et al., 2020). Gas and water are then co-injected into the core to decrease the f_w value, and steady state is reached at each value of f_w (eq. 21). We reach steady state at 5 different values of f_w. The pressure drop is measured at each f_w, and the gas/water relative permeability values are calculated at each f_w (eq. 22).

3.5 RESULTS

In Figure 12, we present gas/water relative permeability measurements in the presence of hydrate (S_h=0.3). We were unable to reliably measure gas and water saturation during flow due to the large volumes of fluids used and the reactivity of the system. Therefore, we plot relative permeability as a function of the fractional flow rate of water (eq. 21). Since the flow rates are set throughout the experiment, f_w is an experimental parameter that is known at all points during each experiment.

The models from Figure 11 are plotted as a function of fractional flow of water or gas at a particular hydrate saturation. S_w are converted into f_w by combining equation (21) and (22),

$$f_w = \frac{\frac{k_{rw}}{\mu_w}}{\frac{k_{rw}}{\mu_w}+\frac{k_{rg}}{\mu_g}}, \tag{23}$$

where the water and gas viscosity (μ_w and μ_g) and the water and gas relative permeability (k_{rw} and k_{rg}) are known for each model.

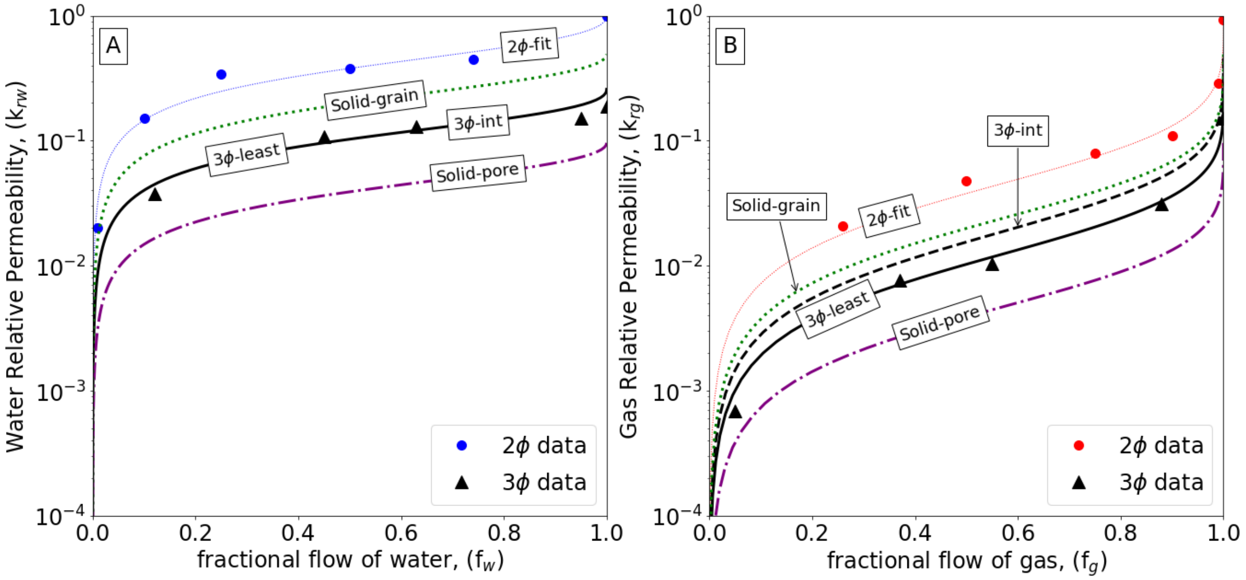

Figure 12. Experimental data and models for water and gas relative permeability in the presence of hydrate (S_h=0.3). In all figures, we show models: *2ϕ-fit* (red/blue line), *3ϕ-least* (black solid line), *3ϕ-int* (black dashed line), solid-pore (purple dash-dot line), and solid-grain (green dot line). A) Measured water relative permeability in hydrate free (blue dot) and hydrate saturated (black triangle) sample as a function of fractional flow of water (f_w). B) Experimentally measured gas relative permeability in hydrate free (red dot) and hydrate saturated (black triangle) sample as a function of fractional flow rate of gas (f_g).

3.7 DISCUSSION

The results in Figure 12A show that the water relative permeability in the presence of hydrate (two- or three-phase) behaves the same as in the presence of gas or oil (two-phase). The measured three-phase data falls right on the three-phase models which suggests that water is indeed acting as the wetting phase and occupying the smallest pores. The solid-pore model predicts hydrate will occupy the pore center, which forces the water into smaller and smaller pores and thus underpredicts the water relative permeability. Conversely, the solid-grain model suggests that hydrate will force water into the larger pores and thus overpredicts the water relative permeability.

In Figure 12B, we present models where hydrate is both the least-wetting (black solid) or intermediate-wetting (black dashed) phase. The three-phase least model (eq. 8, black dashed line) predicts that gas will be the intermediate phase and thus the gas relative permeability is a weighted interpolation between the wetting ($k_{rw}^{2\phi}$) and least-wetting $\left(k_{rg}^{2\phi}\right)$ relative permeability. If gas were the least-wetting phase, the measured three-phase gas relative permeability (black triangles) would be higher since the gas would flow through the larger pores. However, the data clearly shows that three-phase gas relative permeability is reduced which suggests the gas is flowing through the intermediate pores. Similar to the water relative permeability, the solid-pore model underpredicts and the solid-grain model overpredicts the gas relative permeability when using the two-phase parameters.

These results suggest that three-phase water relative permeability can easily be determined from any two-phase experiment (e.g., gas/water) for any other two-phase pair (e.g., hydrate/water). Similarly, if the gas/hydrate pore occupancy is known, the three-phase gas relative permeability can be determined using the same two-phase parameters. Two-phase gas/water experiments are much easier, faster, and cheaper than three-phase experiments or experiments in the presence of hydrate. This method will allow for water relative permeability curves to be developed quickly for various hydrate systems.

To further test this method, experiments should be run at conditions where we predict hydrate will be the intermediate phase and gas will be the least-wetting phase. This scenario is easier to model since the gas and water relative permeability will be the same as the two-phase (gas/water) relative permeability since gas will be the least-wetting phase and water will be the wetting-phase in both cases.

3.8 CONCLUSION

We introduce a thermodynamically based approach for predicting the gas and water flow properties of methane hydrate bearing sediments. By departing from heuristic concepts such as "pore filling" or "grain coating" and instead focusing on thermodynamics and phase occupancy of pores, we achieve a more accurate representation of the complex nature of geologic media, particularly in three-phase scenarios involving gas, water, and hydrate.

To validate our model, we conduct gas and water flow experiments both with and without hydrate. By comparing the results obtained from these experiments to both our physical model and existing models, we were able to assess the effectiveness of our approach.

Notably, our findings demonstrate that the water and gas relative permeability in the presence of hydrate can be determined using measurements from two-phase experiments conducted on sediment without hydrate. This discovery has significant implications as it allows for a more streamlined and efficient assessment of flow properties in methane hydrate bearing sediments. By bypassing the need for hydrate-bearing samples, our approach simplifies the experimental procedure while still providing accurate predictions. This advancement addresses a key limitation of previous models that relied on direct measurements from hydrate-bearing samples.

Beyond relative permeability prediction, this work offers valuable insights into the formation and stability of methane hydrates in geologic settings. Understanding the flow properties of gas and water in the presence of hydrate is crucial for assessing the potential for methane extraction or sequestration, as well as for evaluating the stability of hydrate-bearing sediments.

3.9 REFERENCES

Baker, L. (1988). Three-phase relative permeability correlations. SPE Improved Oil Recovery Conference,

Bear, J. (1972). *Dynamics of Fluids in Porous Media*. American Elservier Publishing Company, Inc.

Blunt, M. J. (2017). *Multiphase Flow in Permeable Media: A Pore-Scale Perspective*. Cambridge University Press. https://doi.org/10.1017/9781316145098

Boswell, R. (2009). Is gas hydrate energy within reach? *Science*, *325*(5943), 957-958. https://doi.org/10.1126/science.1175074

Brooks, R. H., & Corey, A. T. (1964). Hydraulic Properties of Porous Media. *Hydrology Papers*.

Chen, X., & Espinoza, D. N. (2018). Ostwald ripening changes the pore habit and spatial variability of clathrate hydrate. *Fuel*, *214*, 614-622. https://doi.org/10.1016/j.fuel.2017.11.065

Chen, X., Espinoza, D. N., Luo, J. S., Tisato, N., & Flemings, P. B. (2020). Pore-scale evidence of ion exclusion during methane hydrate growth and evolution of hydrate pore-habit in sandy sediments. *Marine and Petroleum Geology*, *117*. https://doi.org/10.1016/j.marpetgeo.2020.104340

Chen, X., Kianinejad, A., & A. DiCarlo, D. (2017). Measurements of CO2-brine relative permeability in Berea sandstone using pressure taps and a long core. *Greenhouse Gases: Science and Technology*, *7*(2), 370-382. https://doi.org/10.1002/ghg.1650

Dai, S., & Seol, Y. (2014). Water permeability in hydrate-bearing sediments: A pore-scale study. *Geophysical Research Letters*, *41*(12), 4176-4184. https://doi.org/10.1002/2014GL060535

Delli, M. L., & Grozic, J. L. H. (2014). Experimental determination of permeability of porous media in the presence of gas hydrates. *Journal of Petroleum Science and Engineering*, *120*, 1-9. https://doi.org/http://dx.doi.org/10.1016/j.petrol.2014.05.011

Eleri, O., Graue, A., & Skauge, A. (1995). Steady-state and unsteady-state two-phase relative permeability hysteresis and measurements of three-phase relative permeabilities using imaging techniques. SPE Annual Technical Conference and Exhibition, Dallas, Texas.

Fang, Y., Flemings, P. B., Daigle, H., Phillips, S. C., Meazell, P. K., & You, K. (2020). Petrophysical properties of the Green Canyon Block 955 hydrate reservoir inferred from reconstituted sediments: Implications for hydrate formation and production. *AAPG Bulletin*, *104*(9), 1997-2028. https://doi.org/10.1306/01062019165

Henry, P., Thomas, M., & Ben Clennell, M. (1999). Formation of natural gas hydrates in marine sediments 2. Thermodynamic calculations of stability conditions in porous sediments. *Journal of Geophysical Research*, *104*(B10), 23005-23022. https://doi.org/10.1029/1999jb900167

Jaiswal, N. J., Dandekar, A. Y., Patil, S. L., Hunter, R. B., & Collett, T. S. (2009). Relative permeability measurements of gas-water-hydrate systems. In T. Collett, A. Johnson, C. Knapp, & R. Boswell (Eds.), *Natural gas hydrates—Energy resource potential and associated geologic hazards: AAPG Memoir 89*.

Johnson, A., Patil, S., & Dandekar, A. (2011). Experimental investigation of gas-water relative permeability for gas-hydrate-bearing sediments from the Mount Elbert Gas Hydrate Stratigraphic Test Well, Alaska North Slope. *Marine and Petroleum Geology*, *28*(2), 419-426. https://doi.org/https://doi.org/10.1016/j.marpetgeo.2009.10.013

Katagiri, J., Konno, Y., Yoneda, J., & Tenma, N. (2017). Pore-scale modeling of flow in particle packs containing grain-coating and pore-filling hydrates: Verification of a Kozeny–Carman-based permeability reduction model. *Journal of Natural Gas Science and Engineering*, *45*, 537-551. https://doi.org/https://doi.org/10.1016/j.jngse.2017.06.019

Kleinberg, R. L., Flaum, C., Griffin, D. D., Brewer, P. G., Malby, G. E., Peltzer, E. T., & Yesinowski, J. P. (2003). Deep sea NMR: Methane hydrate growth habit in porous media and its relationship to hydraulic permeability, deposit accumulation, and submarine slope stability. *Journal of Geophysical Research: Solid Earth*, *108*(B10), 2508. https://doi.org/10.1029/2003JB002389

Kneafsey, T. J., Seol, Y., Gupta, A., & Tomutsa, L. (2011). Permeability of laboratory-formed methane-hydrate-bearing sand: measurements of observations using X-ray computed tomography. *SPE Journal*, *16*(1), 78-94.

Konno, Y., Fujii, T., Sato, A., Akamine, K., Naiki, M., Masuda, Y., Yamamoto, K., & Nagao, J. (2017). Key Findings of the World's First Offshore Methane Hydrate Production Test off the Coast of Japan: Toward Future Commercial Production. *Energy & Fuels*, *31*(3), 2607-2616. https://doi.org/10.1021/acs.energyfuels.6b03143

Kralik, J., Manak, L., Jerauld, G., & Spence, A. (2000). Effect of trapped gas on relative permeability and residual oil saturation in an oil-wet sandstone. SPE Annual Technical Conference and Exhibition, Dallas, Texas.

Lei, L., Park, T., Jarvis, K., Pan, L., Tepecik, I., Zhao, Y., Ge, Z., Choi, J. H., Gai, X., Galindo-Torres, S. A., Boswell, R., Dai, S., & Seol, Y. (2022). Pore-scale observations of natural hydrate-bearing sediments via pressure core sub-coring and micro-CT scanning. *Sci Rep*, *12*(1), 3471. https://doi.org/10.1038/s41598-022-07184-6

Liu, X., & Flemings, P. B. (2006). Passing gas through the hydrate stability zone at southern Hydrate Ridge, offshore Oregon. *Earth and Planetary Science Letters*, *241*(1–2), 211-226. https://doi.org/doi:10.1016/j.epsl.2005.10.026

Liu, X., & Flemings, P. B. (2011). Capillary effects on hydrate stability in marine sediments. *Journal of Geophysical Research-Solid Earth*, *116*(B07102), 24. https://doi.org/10.1029/2010jb008143

Meyer, D. W., Flemings, P. B., & DiCarlo, D. (2018). Effect of Gas Flow Rate on Hydrate Formation Within the Hydrate Stability Zone. *Journal of Geophysical Research-Solid Earth*, *123*(8), 6263-6276. https://doi.org/10.1029/2018jb015878

Moridis, G. J., Kowalsky, M. B., & Pruess, K. (2007). Depressurization-Induced Gas Production From Class 1 Hydrate Deposits. *SPE Reservoir Evaluation & Engineering*, *10*(05), 458-481.

Moridis, G. J., Reagan, M. T., Queiruga, A. F., & Boswell, R. (2019). Evaluation of the performance of the oceanic hydrate accumulation at site NFHP-02-09 in the Krishna-Godavari Basin during a production test and during single and multi-well production scenarios. *Marine and Petroleum Geology*, *108*, 660-696. https://doi.org/10.1016/j.marpetgeo.2018.12.001

Moridis, G. J., Seol, Y., & Kneafsey, T. J. (2005). Studies of Reaction Kinetics of Methane Hydrate Dissocation in Porous Media. In: Lawrence Berkeley National Laboratory.

Murphy, Z. W., DiCarlo, D. A., Flemings, P. B., & Daigle, H. (2020). Hydrate is a Nonwetting Phase in Porous Media. *Geophysical Research Letters*, *47*(16), e2020GL089289. https://doi.org/https://doi.org/10.1029/2020GL089289

Nole, M., Daigle, H., Cook, A. E., Malinverno, A., & Flemings, P. B. (2018). Burial-driven methane recycling in marine gas hydrate systems. *Earth and Planetary Science Letters*, *499*, 197-204. https://doi.org/10.1016/j.epsl.2018.07.036

Oak, M. (1991). Three-phase relative permeability of intermediate-wet Berea sandstone. SPE Annual Technical Conference and Exhibition?, Dallas, Texas.

Sloan, E. D., & Koh, C. A. (2007). *Clathrate Hydrates of Natural Gases*. CRC Press.

Waite, W. F., Santamarina, J. C., Cortes, D. D., Dugan, B., Espinoza, D. N., Germaine, J., Jang, J., Jung, J. W., Kneafsey, T. J., Shin, H., Soga, K., Winters, W. J., & Yun, T. S. (2009b). Physical properties of hydrate-bearing sediments. *Reviews of Geophysics*, *47*(4), RG4003. https://doi.org/10.1029/2008rg000279

White, M. D., Kneafsey, T. J., Seol, Y., Waite, W. F., Uchida, S., Lin, J. S., Myshakin, E. M., Gai, X., Gupta, S., Reagan, M. T., Queiruga, A. F., Kimoto, S., Baker, R. C., Boswell, R., Ciferno, J., Collett, T., Choi, J., Dai, S., De La Fuente, M., . . . Zyrianova, M. (2020). An international code comparison study on coupled thermal, hydrologic and geomechanical processes of natural gas hydrate-bearing sediments. *Marine and Petroleum Geology*, *120*, 104566. https://doi.org/https://doi.org/10.1016/j.marpetgeo.2020.104566

Yoneda, J., Oshima, M., Kida, M., Kato, A., Konno, Y., Jin, Y., Jang, J., Waite, W. F., Kumar, P., & Tenma, N. (2019). Pressure core based onshore laboratory analysis on mechanical properties of hydrate-bearing sediments recovered during India's

National Gas Hydrate Program Expedition (NGHP) 02. *Marine and Petroleum Geology*, *108*, 482-501. https://doi.org/10.1016/j.marpetgeo.2018.09.005

You, K., & Flemings, P. B. (2018). Methane Hydrate Formation in Thick Sandstones by Free Gas Flow. *Journal of Geophysical Research: Solid Earth*, *123*(6), 4582-4600. https://doi.org/10.1029/2018jb015683

You, K., & Flemings, P. B. (2021). Methane Hydrate Formation and Evolution During Sedimentation. *Journal of Geophysical Research-Solid Earth*, *126*(4). https://doi.org/10.1029/2020JB021235

You, K., Kneafsey, T. J., Flemings, P. B., Polito, P., & Bryant, S. L. (2015). Salinity-buffered methane hydrate formation and dissociation in gas-rich systems. *Journal of Geophysical Research: Solid Earth*, *120*(2), 643-661. https://doi.org/10.1002/2014JB011190

Chapter 4: CO_2 hydrate formation and CH_4 hydrate dissociation during flue gas injection

4.1 ABSTRACT

[3]CH_4 hydrate reservoirs are a potential energy source and a CO_2 storage opportunity. We perform flow experiments in a 7.6-meter tube packed with sand and saturated with CH_4 hydrate and water. We flow flue gas through the sample and collect and analyze the effluent gas using gas chromatography to study the spatial variation of phases and composition during injection. The effluent gas composition records three distinct zones: 1) N_2 and CH_4, 2) CH_4, CO_2, and N_2, and 3) N_2 and CO_2. The changing effluent composition corresponds to three zones of varying composition. The initial CH_4 hydrate is first invaded by N_2 and a mixed N_2-CH_4 hydrate is formed. Behind this zone, a three component (CO_2-N_2-CH_4) hydrate forms. Lastly, a hydrate free zone is formed with a vapor component equal to the injected gas composition. This chromatographic separation and reactive transport process, commonly understood in other fields, drives the process of mixed hydrate formation. We present evidence of systematic CO_2 mixed hydrate formation during injection and compare our results to previously developed models of flow during guest molecule exchange. These experiments illuminate a solidification and dissociation process where hydrate replacement is comprised of a complex series of steps that is driven by the combination of fluid flow and thermodynamics. We infer the process also applies to the formation of natural mixed (e.g. CH_4 and CH_6) hydrate systems.

---

[3] This chapter was submitted to Transport in Porous Media in September 2023. The paper is under review as of 10/23/2023.
I conceived and designed this study, performed the experiments, gathered the data, conducted the analysis, made the figures, and wrote the manuscript. David DiCarlo, Daniel Breecker, and Peter Flemings edited the manuscript for clarity and provided valuable feedback on the manuscript contents.

4.2 INTRODUCTION

The global carbon cycle consists of ~10,000 billion tons of organic carbon that cycle through the Earth, ocean, and atmosphere (e.g. Ruppel & Kessler, 2017). There are ~800 billion tons of carbon present in the atmosphere today and any changes to the cycle can significantly impact greenhouse gas concentration and the global climate (Schuur et al., 2008). It is generally agreed that CO_2 emissions are warming the planet, and we are heading towards a 1.5 °C increase by 2050 if behaviors are not altered (e.g. Masson-Delmotte et al., 2018). Thus, as energy demand and CO_2 emissions increase, the need for low-carbon energy alternatives is critical. There is now a global effort to focus on cost-effective methods to reduce CO_2 emissions such as carbon sequestration. We investigate a near-carbon-neutral strategy to produce CH_4 gas from naturally occurring CH_4 hydrate reservoirs while simultaneously sequestering CO_2 as a solid hydrate.

Gas hydrates are a solid consisting of gas and water that are stable at high pressure and low temperature (Sloan & Koh, 2007). Approximately 5-22% of the global carbon budget is stored as CH_4 hydrate (e.g. R. Boswell & T. Collett, 2011; Milkov, 2004; Ruppel & Kessler, 2017). The vast amount of CH_4 gas stored in hydrate-bearing reservoirs has motivated significant research on hydrate systems that spans energy resources (Boswell, 2009; Konno et al., 2017), climate change (Archer et al., 2008; Dickens et al., 1995), and CO_2 sequestration (e.g. Darnell et al., 2019; House et al., 2006; Koh et al., 2016).

Hydrates are generally stable at low temperatures and high-pressures, but the stability conditions also depend on the guest (gas) molecule (Figure 13). For example, CH_4 hydrate is stable at lower pressures and higher temperatures than N_2 hydrate (N_2 (purple) vs CH_4 (red), Figure 8). While much hydrate research has focused on single component systems, there are cases where hydrates will form from a mixture of components, called mixed hydrates. Mixed hydrates can form naturally when CH_4 and heavier hydrocarbons move toward the seafloor (Paganoni et al., 2016) or at CO_2 vents near the seafloor (Sakai et al., 1990). In addition to natural occurrences, mixed hydrates can form if multiple components are injected into the hydrate stability zone.

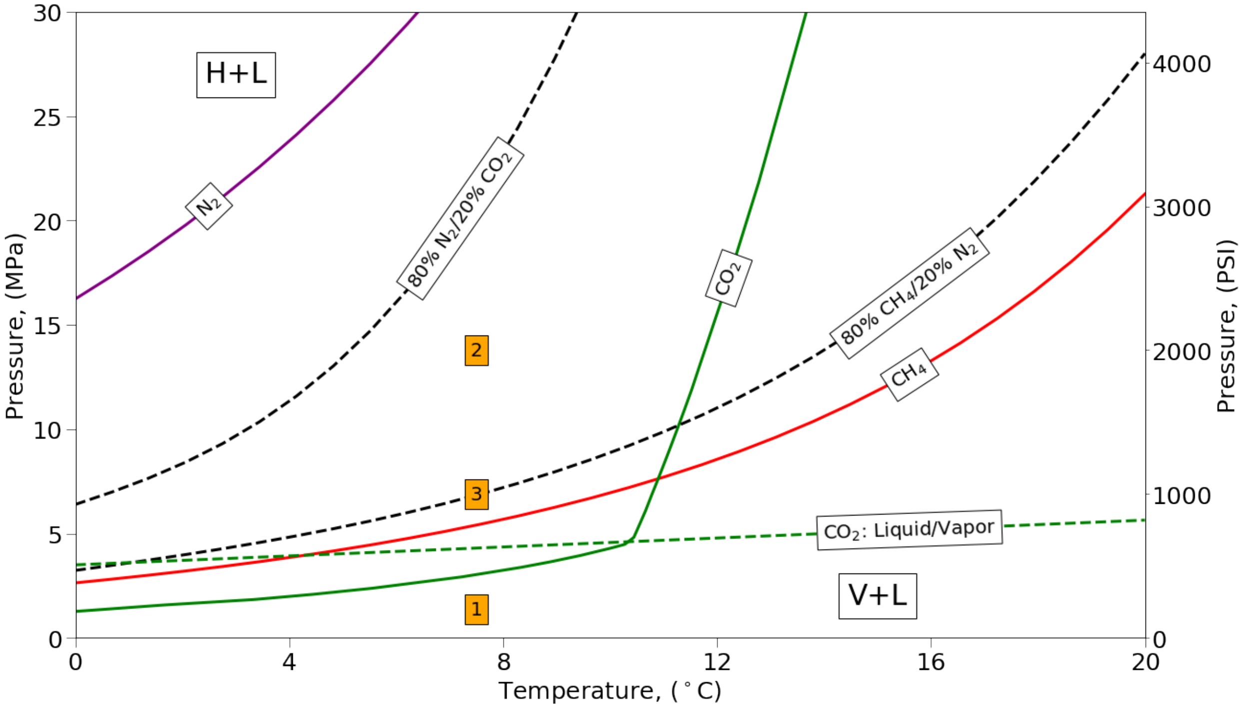

Figure 13 Hydrate phase diagram for CH_4, N_2, CO_2, and gas mixtures. Dashed green line is pure-CO_2 liquid-vapor stability (above this line pure-CO_2 is in liquid phase). Hydrate + Liquid is stable above the lines (i.e., higher pressure and lower temperature). Vapor + Liquid is stable below the lines (i.e., lower pressure and higher temperature). Numbered boxes illustrate specific pressure and temperature conditions used in this study.

A possible production and sequestration strategy is to swap CH_4 for CO_2 in the hydrate phase during multicomponent gas injection. This injection process is called 'guest molecule exchange' and has long been proposed as a method for producing CH_4 hydrate while sequestering CO_2 hydrate (e.g. Birkedal et al., 2015; Kang et al., 2014; Ohgaki et al., 1996; Smith et al., 2001). The feasibility of guest molecule exchange has been explored in the lab (Birkedal et al., 2015; Kang et al., 2014; Park, 2006) and in field tests on the Alaskan north slope (Boswell et al., 2017; Schicks et al., 2018).

Pure CO_2 injection into CH_4 hydrate reservoirs was first proposed as an injection strategy (Ohgaki et al., 1996; Park, 2006). In this method, a pure-CO_2 hydrate region will quickly form and then exchange occurs as a solid-solid diffusion process between CO_2 hydrate and CH_4 hydrate (Figure 14a) (Ota et al., 2005). Since the hydrate-hydrate direct exchange process is very slow, pure-CO_2 injection can limit the ability to inject or cause blockages in the pore space (e.g. Birkedal et al., 2015; Lee et al., 2003).

To address the challenges with pure CO_2 injection, both field experiments (Schoderbek & Boswell, 2011) and laboratory studies (Kang et al., 2014; Park, 2006) have demonstrated that co-injection of N_2 and CO_2 may facilitate the exchange process. These efforts suggest that co-injection of CO_2 and N_2 results in improved guest molecule exchange and that greater fractions of N_2 results in more rapid exchange. Kang (2014) proposed that co-injection can be described as a ‘replacement and decomposition’ process as opposed to pure-CO_2 injection which is just a ‘replacement’ process. This process combines CH_4 hydrate dissociation with CO_2 mixed hydrate formation, but its mechanics are poorly understood (Anderson et al., 2014; Birkedal et al., 2015; Boswell et al., 2017).

During ‘replacement and decomposition’, the system begins with pure CH_4 hydrate (red line, Figure 13). As multiple components are injected, H_2O, CH_4, CO_2, and N_2 will form mixed hydrates at conditions where single phase (CO_2 or CH_4) hydrate will also form if the N_2 concentration is low (e.g., CH_4/N_2 mixture, Figure 13). As the amount of N_2 present in the system increases, hydrate will be less stable (e.g., N_2/CO_2 mixture, Figure 13). With enough N_2, the components will separate into a vapor and aqueous phase as hydrate will only be stable at very high pressure and low temperature (N_2 (purple), Figure 13). Thus, at optimal conditions, a multicomponent system could result in a produced vapor phase that is enriched in CH_4, and a stored mixed hydrate phase enriched in the injected gas (e.g., CO_2).

Darnell et al. (2019) developed a local equilibrium model that consists of advective gas and liquid flow through the medium combined with phase equilibrium (hydrate, liquid, and gas at every spatial position. Unlike other work that suggest simultaneous swapping of CH_4 for CO_2 (e.g. Park, 2006), the equilibrium model offered a new conceptual model based on multicomponent phase behavior that suggests guest molecule exchange occurs in separate but simultaneous processes (Figure 14B). N_2 causes CH_4 hydrate dissociation independently of CO_2 and allows for a connected vapor phase throughout the system which allows for the much faster vapor-solid exchange process to dominate instead of diffusion (e.g. Lee et al., 2003).

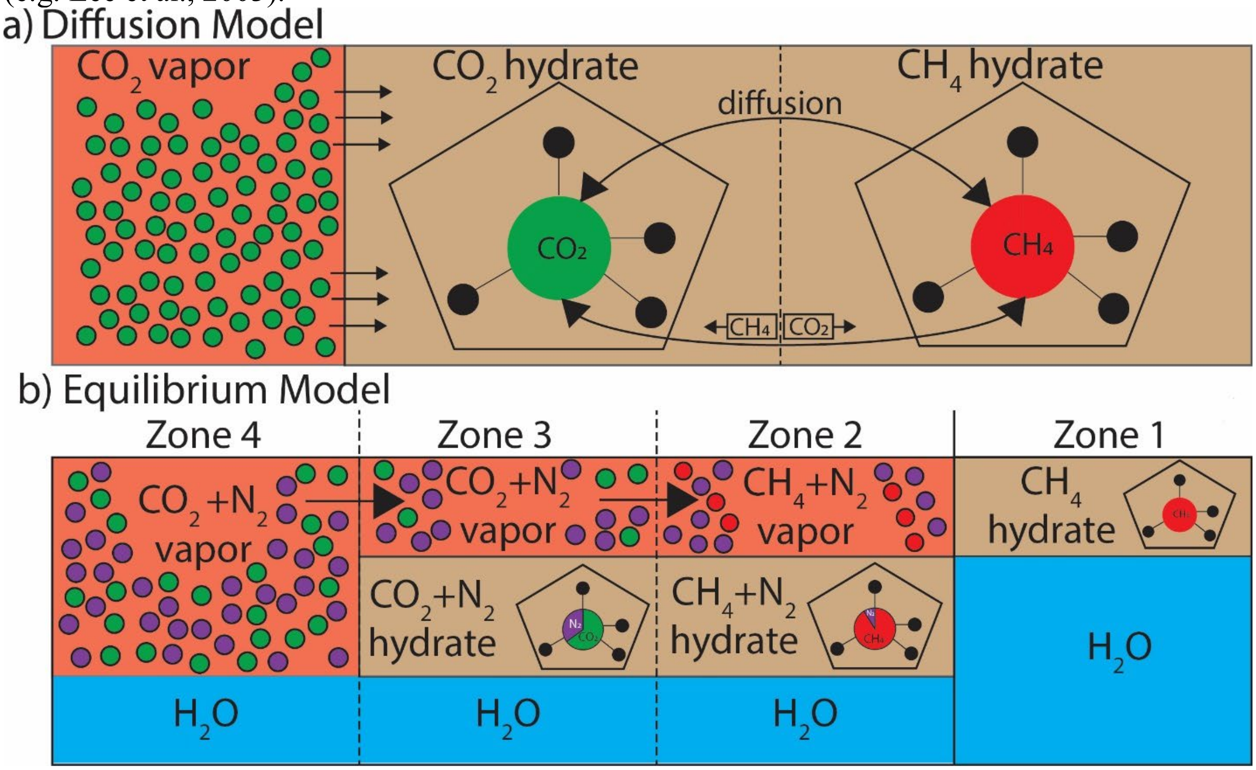

Figure 14 Cartoon representation of two different 'guest molecule exchange' models. Diffusion model shows solid-solid diffusive exchange of CO2 and CH4 in hydrate phase. Equilibrium model shows four zones that will appear in the system: zone 1) initial conditions (pure CH4 hydrate), zone 2) N2-CH4 hydrate and vapor (no CO2), zone 3) N2-CO2 hydrate and vapor (no CH4), zone 4) N2 and CO2 vapor at injection composition. Some or all these zones will appear depending on the conditions (P, T, and composition).

The distinct regions from the equilibrium model suggest that guest molecule exchange is composed of two sequential processes that are facilitated by chromatographic separation of a N_2 rich vapor phase. This chromatographic separation is essentially catalyzed by the N_2 and may explain why injections into hydrate-bearing reservoirs with more N_2 have been more successful than those with little to no N_2 (e.g. Boswell et al., 2017; Schicks et al., 2018). Separation occurs since each component will partition into its equilibrium phase (liquid, gas, hydrate) at varying compositions (Darnell, 2017). The presence of N_2 will allow for a separate vapor phase that facilitates the exchange process. If there is no vapor phase (Figure 14A), exchange becomes diffusion-limited and essentially stops (Lee et al., 2003). However, if there is a vapor phase, exchange will occur much more rapidly (Figure 14B). Therefore, Darnell (2019) and others have suggested that injecting a mixture of CO_2 and N_2 (flue gas) will create connected three-phase regions where guest molecule exchange can occur and not be slowed by blockages or limited by diffusion.

We seek to understand the evolution of mixed hydrate systems during multiphase flow in multicomponent systems with varying hydrate stability conditions. We develop new experiments to illuminate chromatographic separation in hydrate-forming systems during guest molecule exchange. We flow a CO_2 and N_2 gas mixture through a CH_4 hydrate reservoir and measure the effluent vapor composition and pressure and temperature conditions. From these experiments, we can understand the phase behavior and composition during flue gas injection in a hydrate reservoir and compare our results to previously established models. This work provides insight into reactive transport processes in hydrate systems and how mixed hydrates will form in natural geologic systems.

4.3 EXPERIMENTAL METHODS

We develop a 'slimtube' apparatus, a long tube that is packed with sand, to examine one-dimensional flow of a N_2-CO_2 mixture into a CH_4 hydrate bearing reservoir. Slimtubes are used in porous media research to simulate one-dimensional flow through a reservoir (e.g., Khan et al., 1992). Our slimtube is 7.9 m in length and 4.9 mm in diameter (Figure 15). We use the slimtube because 1) it is long enough to allow flow and reaction fronts to develop as would occur in a reservoir, 2) it is thin enough that the flow can be approximated to be one-dimensional, and 3) it is representative of the flow properties of porous media.

To create repeatable experiments, we develop a method for forming hydrates in this slimtube apparatus resulting in a two-phase system (liquid + hydrate). We then perform flow experiments in the presence of hydrates.

4.3.1 System Overview

To prepare the sample, the slimtube is packed with sand (d50=250 micron) to a porosity of 39%. After packing, the pore volume of the system is 60 ml. The stainless-steel tube is outfitted with absolute pressure transducers at the upstream and downstream ends. A gas injection pump, brine injection pump, and mass flow controller (MFC) are connected to the upstream end. A back-pressure regulator (BPR), gas/water separator, scale, and gas flow meter are connected to the downstream end. The apparatus is kept in a temperature-controlled facility (±1°C) where the room, upstream, and downstream temperature are monitored. A schematic of the experimental apparatus is shown in Figure 15.

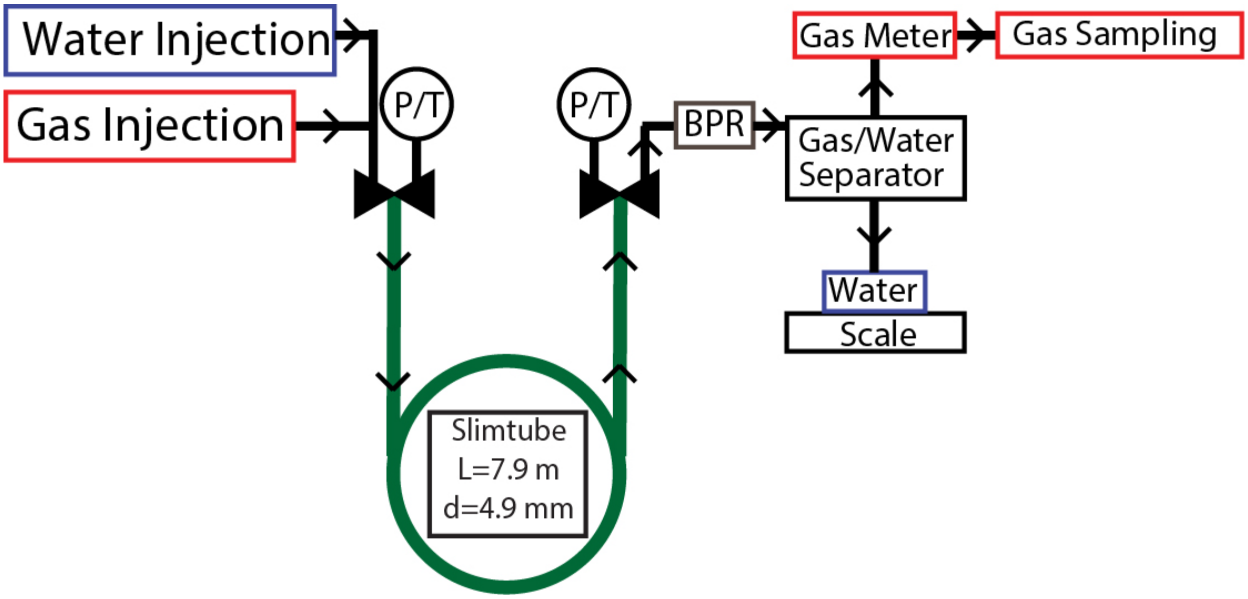

Figure 15 Schematic of system showing injection, slimtube, and effluent setup. Water injection is from ISCO syringe pump. Gas injection is from a mass flow controller (MFC). Pressure and temperature are measured at upstream and downstream ports (P/T). Coiled slimtube apparatus is 7.9m long and 4.9mm in diameter and is packed with sand. System pressure is maintained with back-pressure-regulator (BPR). Effluent travels through gas/water separator where gas moves to gas flow meter and gas sampling point, and water is collected and measured on a scale.

4.3.2 Phase saturation calculation

During the experiment, we measure the upstream and downstream pressure, average system temperature, and quantity (volume or mass) of every component injected or removed from the system. At the upstream end, we meter the amount and composition of every phase injected into the core. At the downstream end, we meter the produced liquid and vapor, and at periodic intervals, sample the vapor for analysis by gas chromatography. From this, we calculate and track the moles (or mass) of every component in the column.

There are five components present: CH_4, N_2, CO_2, H_2O, and NaCl. NaCl and H_2O are defined as water components and are measured as moles of water component molecules (m_w). NaCl is only present in the liquid phase, and H_2O can be present in the liquid or hydrate phase. We define the remaining components (CH_4, CO_2, and N_2) as the vapor component molecules, and they are measured as moles of vapor component (m_v). The vapor component molecules can be present in any phase (gas, liquid, or hydrate) in the system but will be in the vapor phase at atmospheric conditions (effluent). All three vapor components can act as guest molecules in the hydrate phase (mixed or pure hydrate) and can dissolve into the liquid phase (CO_2 more than others).

Using the mole balance, we can calculate the bulk phase saturation of each phase (gas, liquid, hydrate) within the core at any point during the experiment. The bulk phase saturation is defined as the pore space occupied by each phase over the entire core and is calculated from the following three equations:

$$1 = S_h + S_l + S_g, \tag{1}$$

$$m_w = \left(X_w^l \rho_l S_l + X_w^h \rho_h S_h\right) V_p, \tag{2}$$

$$m_v = \left(X_v^l \rho_l S_l + X_v^g \rho_g S_g + X_v^h \rho_h S_h\right) V_p, \tag{3}$$

where S_i is saturation of phase i, X_u^i is the mole fraction of component u in phase i, ρ_i is molar density of phase i, and V_p is pore volume. The observed salinity ranges from 2-6% through the experiment, which has a very small impact on the saturation calculation (ΔS_i <1%). We therefore assume the salinity to be constant at 3.5wt% for all mass balance calculations. While the solubility difference between CH_4, CO_2, and N_2 is not insignificant (X_v^g ranges from 0.0016-0.02), the impact of solubility changes on the saturation calculation is very minor (ΔS_i<0.5%). For simplicity in the mass balance calculation, we assume the vapor density (ρ_g) and solubility (X_v^l) are independent of composition. All other variables are known or measured except for the three saturations. The detailed mole balance method is found in Appendix A.

Table 2 Nomenclature and dimensions used in this study.

Symbol	Name	Unit
l	liquid phase	(-)
g	free gas phase	(-)
h	hydrate phase	(-)
m_w	moles of water components	(mole)
m_v	moles of vapor components	(mole)
S_l	liquid phase saturation	(-)
S_g	gas phase saturation	(-)
S_h	hydrate phase saturation	(-)
V_p	pore volume	(m^3)
ρ_g	gas phase density	(mole/m^3)
ρ_l	liquid phase density	(mole/m^3)
ρ_h	hydrate phase density	(mole/m^3)
X_u^i	mass fraction of component (u) in phase (i)	(-)
k_{abs}	absolute permeability	(m^2)
Q	flow rate	(m^3/s)
μ	viscosity	(Pa·s)
P	pressure	(Pa)
L	length	(m)
A	area	(m^2)

4.3.3 Sample preparation and hydrate formation

The hydrate formation and sample preparation methods are modified from Murphy (2020). To best mimic natural deposits, we form a sample with a known CH_4 hydrate concentration that contains only water and hydrate. Creating a hydrate-saturated core with only water and hydrate is a multistep process that includes initial saturation, hydrate formation, and brine flood.

Initially, the slimtube is fully saturated with brine (3.5wt% NaCl). The absolute permeability is measured by flowing brine across the brine saturated slimtube at a constant flow rate and using Darcy's law:

$$k_{abs} = \frac{-Q \cdot \mu}{A}\left(\frac{L}{\Delta P}\right) \tag{4}$$

where Q is the flow rate, μ is the viscosity, L is the length, A is the area, and ΔP is the pressure drop. The absolute permeability was determined to be 2.96e-12 m^2 (~3 D).

Once the core is brine-saturated, we inject CH_4 gas at a constant flowrate (10-50 standard cm^3/min (sccm)). We do so at a pressure and temperature where hydrate is unstable (2 MPa and 7°C) (Orange Box 1, Figure 13). We measure the mass of brine displaced and gas injected and continue injection until a desired gas saturation is reached (S_g=20-40%).

After displacement, the gas pressure is increased to ~12 MPa and the sample enters the hydrate stability zone (Orange Box 2, Figure 13). The sample is shut-in, and the pressure is allowed to equilibrate throughout the core. The sample is then left for hydrate formation to occur. As hydrate forms, the pressure decreases (Figure 16A). Formation generally begins within 1-2 days and can continue for more than 7 days. The pressure will continuously decrease until the pressure is close the three-phase stability zone where no additional hydrate will form (You et al., 2015). If a higher hydrate saturation is desired, the gas pressure is increased (1 or more times) to provide more potential for hydrate formation and then left for a longer period (>7 days) to facilitate additional hydrate formation.

From the pressure, temperature, and mole balance, we calculate the bulk phase saturation for the duration of the experiment (Figure 16B). Although the core is 7.9 meters long and likely heterogeneous in composition, the saturation calculation gives a good bulk approximation of the phases present in the core at each time during the experiment.

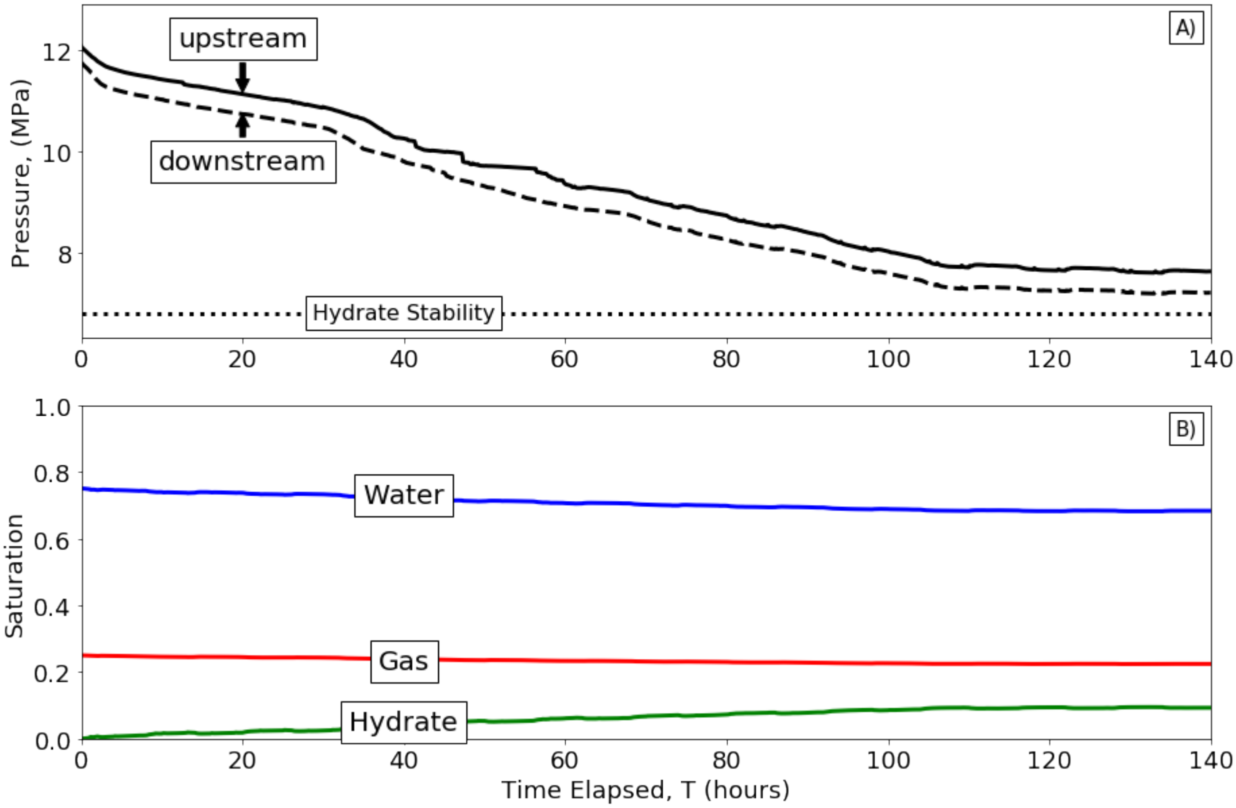

Figure 16 Example experimental results of hydrate formation. **A)** Measured pressure during hydrate formation and estimated hydrate stability. The pressure was increased to enter the hydrate stability zone (0 hours). The system is shut in and hydrate is allowed to form for 7 or more days. The system is closed so any pressure drop is caused by hydrate formation. In our many hydrate experiments, the upstream pressure is generally above the downstream pressure, and we infer this behavior is due to capillary effects. **B)** Calculated phase saturation from mole balance analysis and measured pressure. At the completion of the hydrate formation stage, there are three phases (liquid, gas, hydrate) present in the core.

During formation, the system approaches but does not reach three-phase stability and hydrate formation slows as higher saturations are reached (Figure 16A). Once hydrate forms in the sample, there are three stable phases present in the core (gas, liquid, hydrate). As hydrate forms, salt will be excluded which slightly increases the pore water salinity (5-6%).

To achieve a two-phase (hydrate and liquid) system, we inject 3.5% NaCl brine at a constant flow rate (0.1-0.5 ml/min) for ~1 pore volume (60 mL) or until no additional gas is displaced from the sample. During the brine flood, gas is displaced until brine breaks through. Once ~20 mL (0.33 pore volumes) of brine flows out of the system, the core is shut in and allowed to equilibrate for ~24 hours. We resume brine injection and allow brine to flow through the core for an additional 30 ml (0.5 pore volumes). If we see no additional vapor removed from the system and brine flows at steady state, we infer that all vapor has been removed, formed additional hydrate, or dissolved into the pore water. We also assume that the salinity returns to 3.5% during the brine injection. At the end of the brine flood, the bulk hydrate saturation slightly increases, and the gas saturation is zero from the mole balance calculation. We also measure the water effective permeability (equation 4). Based on Murphy (2020) and the effective permeability, we confirm our calculated hydrate saturation calculation (e.g., if $k_{eff,w}$=74 mD then S_h=0.25).

4.3.4 Flue gas injection

After the core is initialized with brine and hydrate, flue gas (80% N_2 / 20% CO_2) is injected using the MFC at a constant flow rate (Q_g=30-100 sccm). The effluent gas/water mixture passes through a gas/water separator where the water drops out onto a scale for measurement, and the gas continues to the flow meter and sample collection point. At regular intervals (every 0.05-0.1 pore volume of gas injected), gas samples are taken in 15 mL gas bags. The gas sample composition is measured using gas chromatography that is calibrated to detect CO_2, N_2, and CH_4. The gas chromatograph determines the moles of each gas present in the sample of effluent gas.

4.3.5 Experiment replication

The flow experiment was replicated multiple times at different hydrate saturations and in a hydrate free sample. We conducted the gas injection in a hydrate free sample to isolate which behavior is caused by the presence of hydrate versus other factors.

For the hydrate free experiment, a similar procedure is followed with different initial conditions (L+V instead of H+L) and the pressure remains below the hydrate stability zone for the duration of the experiment (Orange Box 1, Figure 13). At the lower pressure, flue gas is injected, and the effluent collected.

4.4 RESULTS

4.4.1 Gas injection results

We present the results of flue gas injection for the experiment where the initial hydrate saturation is interpreted to be ~25%. Flue gas is injected at the upstream end at 75 sccm (0.5 ml/min at 7-7.5 MPa and 6-7°C) for 5 hours. Figure 17 shows the measurements and saturation calculations for the duration of the gas flood experiment.

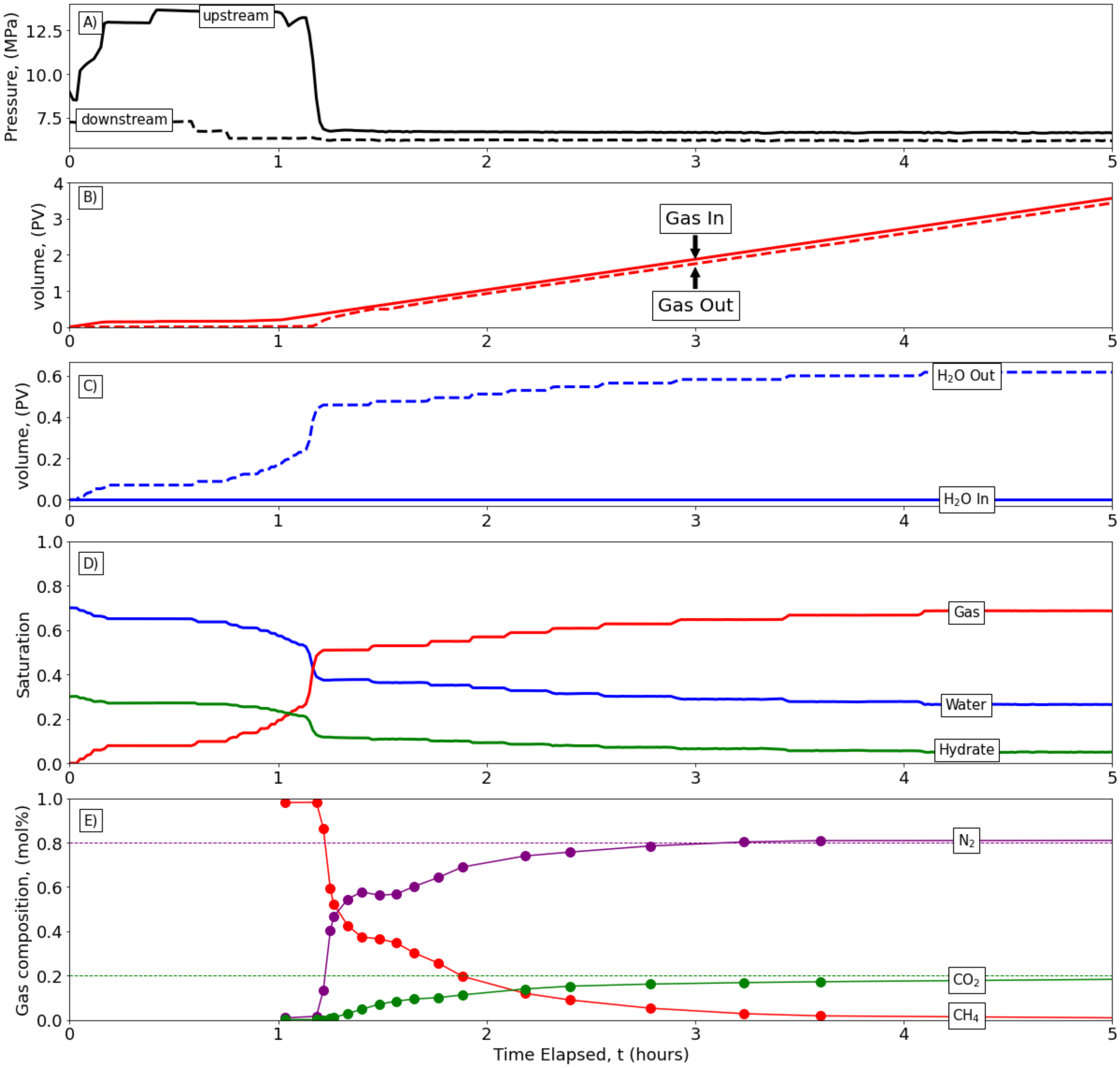

Figure 17 Experiment S_h=0.25: gas flood experimental results and saturation calculation. **A)** Upstream and downstream pressure. **B)** Gas injected and removed from system in pore volumes (1 PV=60 mL at 7°C and 7 MPa). **C)** Water injected and removed in pore volumes. **D)** Calculated bulk phase saturation from mass balance analysis. **E)** Measured gas effluent composition from gas chromatography (solid lines). Dashed lines represent injection composition of N_2 (purple) and CO_2 (green).

Pre-breakthrough: At t=0, we begin injecting flue gas. From t=0-1.2 hours, a small amount of gas is injected (Figure 17A) into the system to pressurize the system (Figure 17A) and a small amount of water flows out (Figure 17C). As gas is injected, the system pressure reaches 13.8 MPa, which is the maximum allowable pressure of the equipment. Since the pressure cannot be increased and no flow is observed, the system is likely clogged by hydrate. To remove the clog and resume flow, the downstream pressure is dropped in small intervals (~0.15 MPa) using the BPR (Figure 17A, t=0.6 hours and 0.7 hours). At t=0.8 hours, gas flow slowly resumes, and full flow resumes at t=1.0 hours (Figure 17B/C). Gas injection continues from t=1-1.2 hours and only water is removed from the system (Figure 17B/C).

Breakthrough and after: At t=1.2 hours, gas breakthrough occurs when gas first flows out of the system (Figure 17B). At breakthrough, there is now a connected gas phase throughout the system which results in the upstream pressure rapidly dropping to a value comparable with the downstream pressure (Figure 17A). As the pressure drops, a large amount of gas moves through the core, which results in gas and water being quickly removed from the system (t=1.25 hours, Figure 17B/C). Little water is displaced after gas breakthrough (Figure 17C), and gas flows through the core with the total amount injected equal to the amount eluted (Figure 17B).

To examine the bulk properties of the system, we assume that the composition within the core is homogenously mixed (composition independent gas density and solubility). From the pressure measurements and mass balance calculation (section 4.2), the calculated bulk phase saturation of each phase is shown (Figure 17D). Before t=1.2 hours, there are no major changes in saturation since there is very little flow. At t=1.2 hours, a large amount of gas is injected, and water is removed, which results in an instantaneous increase in gas saturation and decrease in water and hydrate saturation. As gas injection continues, the gas saturation continues to rise and the water and hydrate saturation decrease. By the end of the gas flood, the bulk saturation calculation predicts that some hydrate has been destroyed ($S_{h,final}$= ~8%) and the system contains mostly gas and water (t=5 hours, Figure 17D).

From the gas bag analysis, the effluent composition of the vapor phase component is shown (Figure 17E). Gas effluent begins at t=1.2 hours, and the effluent is initially only CH_4 (red). After the short pure CH_4 front (t=1-1.2 hours), N_2 (purple) first appears in the effluent but no CO_2 (green) is observed. From t=1.2-1.6 hours, the effluent composition is predominantly N_2 and CH_4 with a small amount of CO_2 appearing. During t=1.6-3.5 hours, the CO_2 and N_2 concentration gradually increase, and CH_4 is removed from the system until almost no CH_4 remains (t=3.5 hours). After t=3.5 hours, the CO_2 and N_2 reach the injection composition (dashed line), which means the composition of the injected fluid is the same as the effluent fluid.

4.4.2 Additional experiments

We present two additional gas flood experiments: one with a higher initial hydrate saturation (S_h=33%) and one that is hydrate free (S_h=0%). To easily compare the different experiments since each experiment has different timescales, we convert elapsed time (hours) to pore volumes of gas out (PV gas out). This is the amount of gas removed from the system in pore volumes (1 PV=60 ml) at core conditions (7 MPa and 7°C). The vapor effluent composition for all three experiments is shown below.

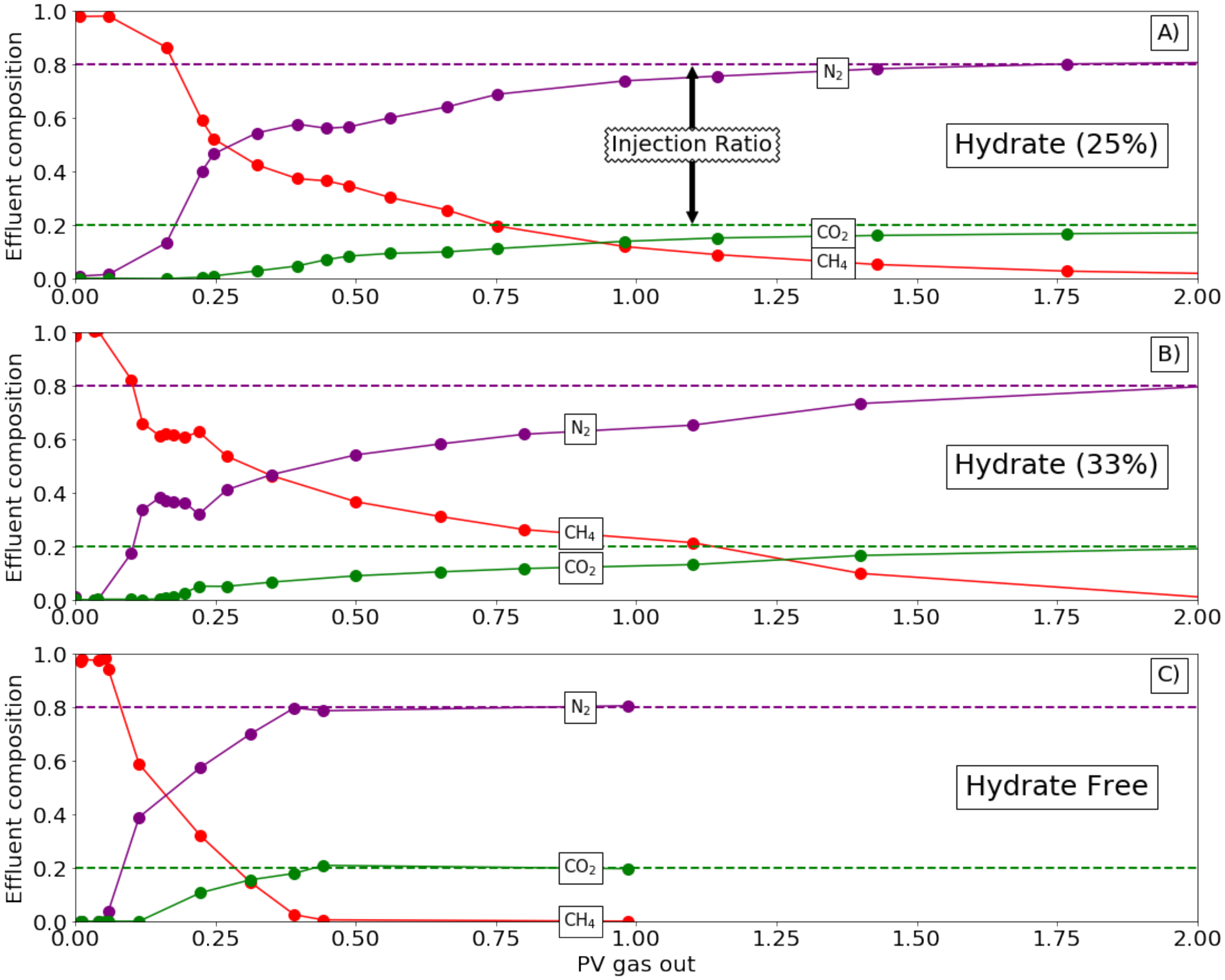

Figure 18 Effluent composition from gas chromatography for three separate experiments. **A)** Hydrate saturation of 25%. **B)** Hydrate saturation of 33%. **C)** Hydrate free experiment.

In all experiments, the effluent begins with the composition initially present in the core (CH_4+H_2O) then transitions to the injected fluid composition (CO_2+N_2). However, the transition from the initial to final composition is fundamentally different in the with hydrate and without hydrate experiments. In the hydrate cases, after an initial pure CH_4 displacement, there is a clear bench where there is a constant ratio of CH_4 and N_2 (Figure 6A/B, PV=0.04-0.25). After the bench, CO_2 begins to appear and increases in concentration until all CH_4 is removed and the injection composition is reached. In the hydrate free case, there is simply a gradual transition from initial composition to final composition. In addition to the composition path, the injection composition is reached much faster in the hydrate free experiment compared to the experiments with hydrate. While the initial composition varies slightly between cases, these differences are likely caused by hydrate formation and dissociation.

4.5 EVIDENCE OF MIXED HYDRATE FORMATION

Three aspects of the bulk average behavior suggest mixed hydrate formation: 1) the CO_2-N_2 effluent ratio in hydrate-saturated and hydrate-free experiments, 2) the maximum amount of CO_2 that can be stored in the core before hydrate formation occurs, and 3) the vapor phase component composition in core throughout the experiment.

4.5.1 CO_2-N_2 ratio in vapor effluent

We compare the ratio of CO_2 to N_2 in the effluent in a hydrate-bearing and hydrate-free samples (Figure 19). In each experiment (with or without hydrate), the effluent vapor composition initially has less CO_2 relative to the injection fluid (i.e., CO_2 preferentially remains in the core). This indicates that CO_2 and N_2 are travelling at different rates through the core, a process called chromatographic separation. This separation may occur because of mixed hydrate formation and/or preferential dissolution of CO_2 into the pore water relative to N_2. Since the solubility of CO_2 is approximately 10x that of N_2 at the pressure and temperature conditions, chromatographic separation is expected as more CO_2 will dissolve into the pore water than N_2. The solubility is constant between the hydrate-free and hydrate-bearing samples, which suggests the differences are caused by CO_2 hydrate formation.

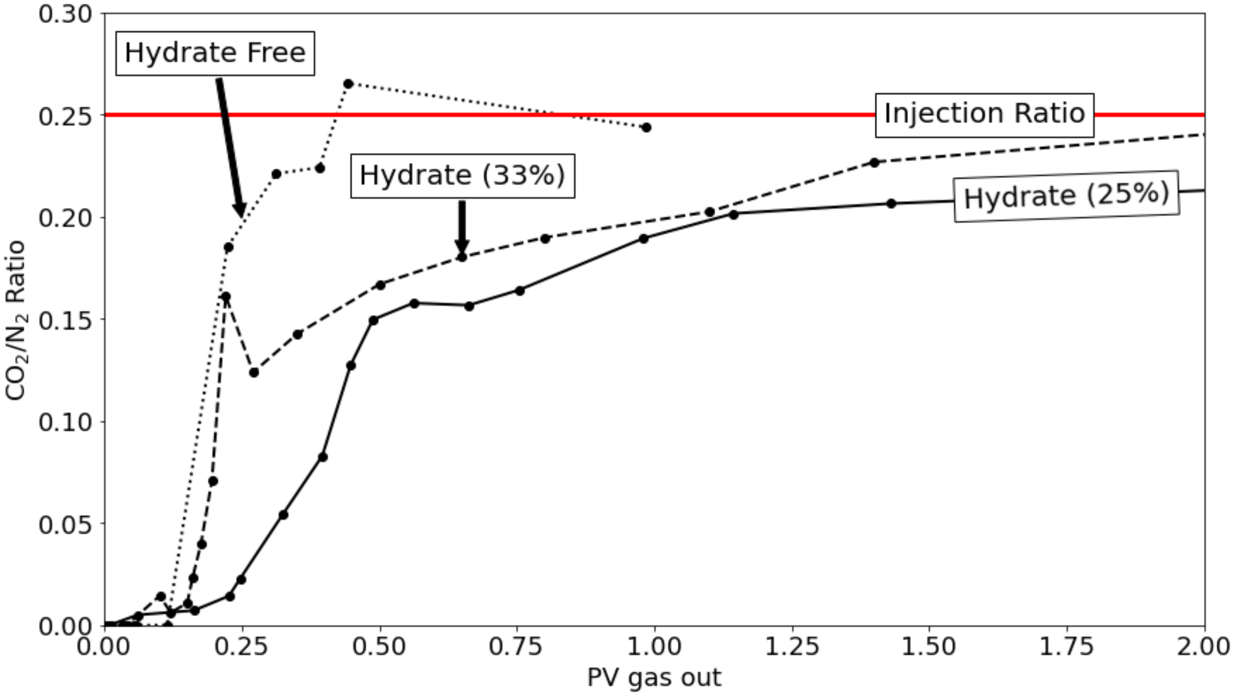

Figure 19 Comparison of hydrate free (dotted) and hydrate saturated (dashed: 33%, solid: 25%) CO_2-N_2 ratio in effluent to injection ratio (red solid). The effluent is undersaturated in CO_2 for longer in the hydrate samples relative to the hydrate free sample (i.e. more CO_2 is left behind in the core).

In the hydrate free experiment, the CO_2/N_2 ratio is achieved after injection of 0.4 pore volumes. This lag is caused only by preferential dissolution of CO_2 into the pore water. In contrast, the input CO_2/N_2 ratio is achieved after two pore volumes in the hydrate-bearing case. The simplest explanation for the increased CO_2 left in the core is that mixed hydrate is forming.

4.5.2 Maximum CO_2 that can be stored in core without forming hydrate

For further evidence that mixed hydrate forms in the column, we calculate the maximum CO_2 that can be stored in the pore volume of the core at two conditions (**P2 (hydrate unstable):** 2.5 MPa and 7°C and **P1 (hydrate stable):** 7.5 MPa and 7°C). If the pore space is fully saturated with the flue gas mixture, there will be 0.021 moles at P2 conditions (dashed black line, Figure 20) and 0.036 moles at P1 conditions (dashed blue line, Figure 20) of CO_2 in the core. We then compare these values of maximum CO_2 (dashed lines) to the measured moles of CO_2 (solid lines) in the core during our experiments (Figure 20).

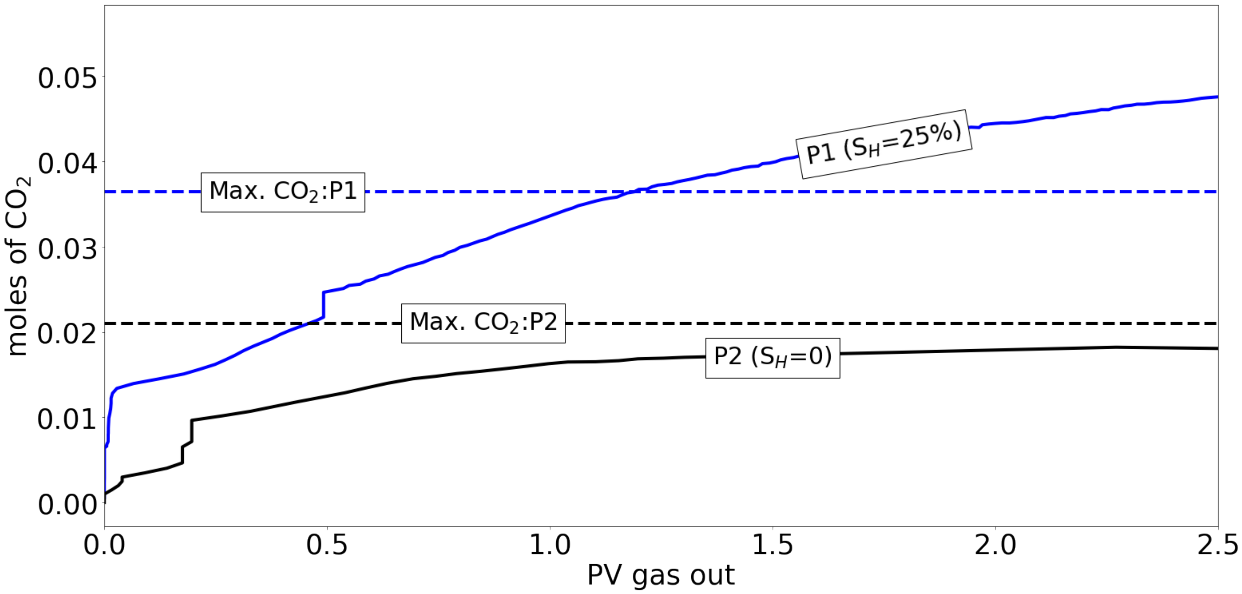

Figure 20 Maximum CO_2 that can be stored in core at experimental conditions. Maximum CO_2 lines (dashed lines) are moles of CO_2 present in core if fully saturated with flue gas mixture at experimental conditions (P1 (7 MPa) or P2 (2.5 MPa)). The total moles of CO_2 present in the core are presented for two experiments (blue solid: S_h=0.25 and black solid: S_h=0).

At P2 conditions, the measured CO_2 (black solid line) converges toward, but does not reach, the maximum CO_2 line (black dashed). We infer that hydrate did not form, as expected, because we are not at hydrate forming conditions. However, at P1 conditions, the measured CO_2 (blue solid line) exceeds the maximum CO_2 line (blue dashed) after ~1 PV of gas out. Since more gas can be stored in the mixed hydrate phase than in the vapor phase per unit volume, CO_2 hydrate must have formed. Based on this analysis, we interpret there to be CO_2 hydrate present in the bulk system after ~1 PV of gas out (i.e., when solid blue line is above dashed blue line).

4.5.3 Bulk saturation and composition in core

We next examine the bulk phase saturation and the vapor molecule composition in the core to understand if mixed hydrates should form (Figure 21). For this calculation, we assume all vapor component molecules have the same properties (density and hydrate stoichiometry) and a homogenous composition throughout the column. The bulk saturation (liquid, vapor, and hydrate) is calculated using our mole balance analysis (Appendix A) which ignores any phase or component partitioning but provides insight to the bulk phase behavior (Figure 21A). Since we know the initial composition of the vapor molecules (pure CH_4), all inputs (flue gas), and outputs (gas chromatography), we also determine the bulk vapor component molecule (CH_4, CO_2, and N_2) composition of the sample at any time (Figure 21B).

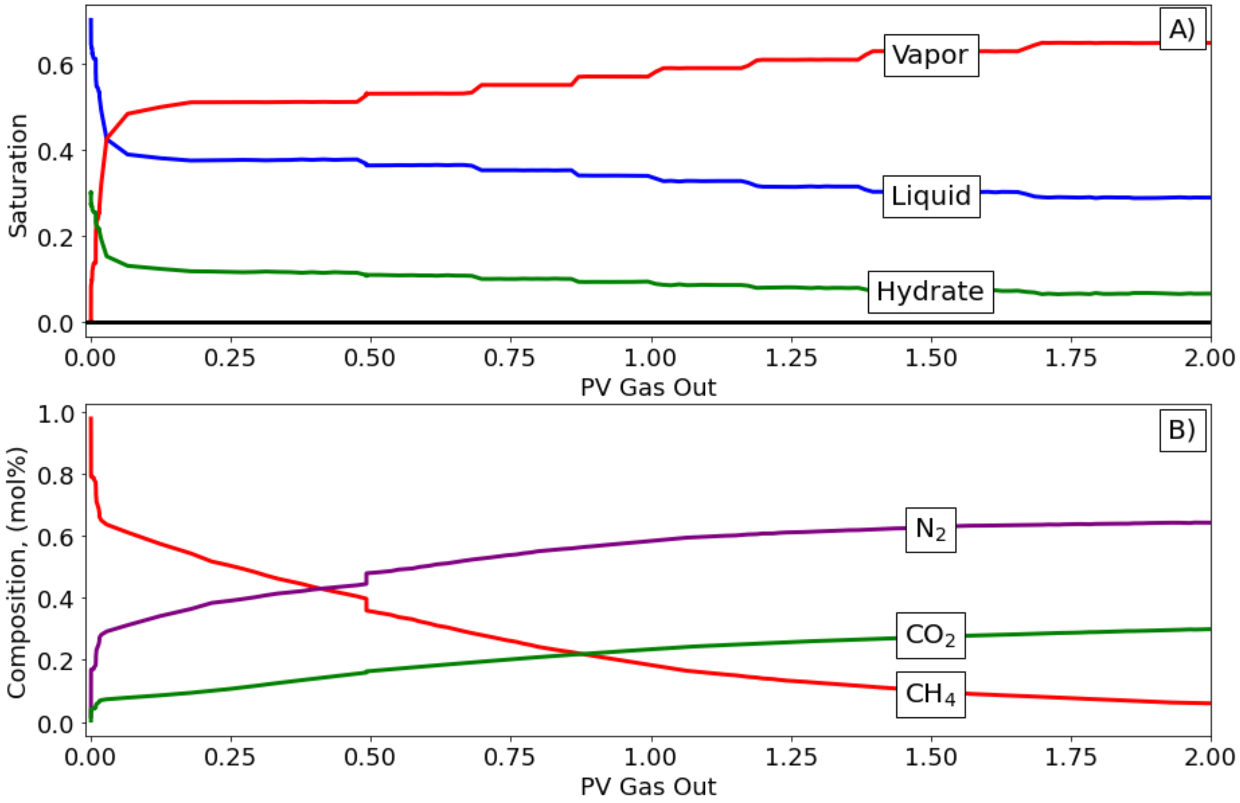

Figure 21 Saturation and vapor molecule composition in core. **A)** Bulk saturation calculation in core. We assume even distribution of components within core. **B)** Vapor molecule composition in core. Initially, only CH_4 is present in the core. We inject 80% N_2-20% CO_2 and measure all effluent gas. We then calculate the total mol% present of each component.

Given the total number of moles of H_2O, CH_4, N_2, and CO_2 present in the core at the pressure and temperature conditions, we predict a bulk mixed-hydrate phase to be present in the core (Figure 21A). This implies that if the core is homogenously distributed, we predict an evenly distributed hydrate phase that contains CH_4, CO_2, and N_2 (Figure 21B). These calculations do not capture the expected heterogenous behavior of mixed hydrate formation but highlight the bulk stability of mixed hydrate.

4.5.4 Evolution of hydrate and vapor composition through the experiment

Figure 22A and 20B present ternary phase diagrams for N_2-CH_4-CO_2 mixtures in the presence of water at two different pressure and temperature conditions (PT-1: 7 MPa and 7°C and PT-2: 7.5 MPa and 6 °C) are shown. Given the variability of temperature and pressure in our laboratory (particularly temperature), we view these as equally possible representations of our experimental conditions.

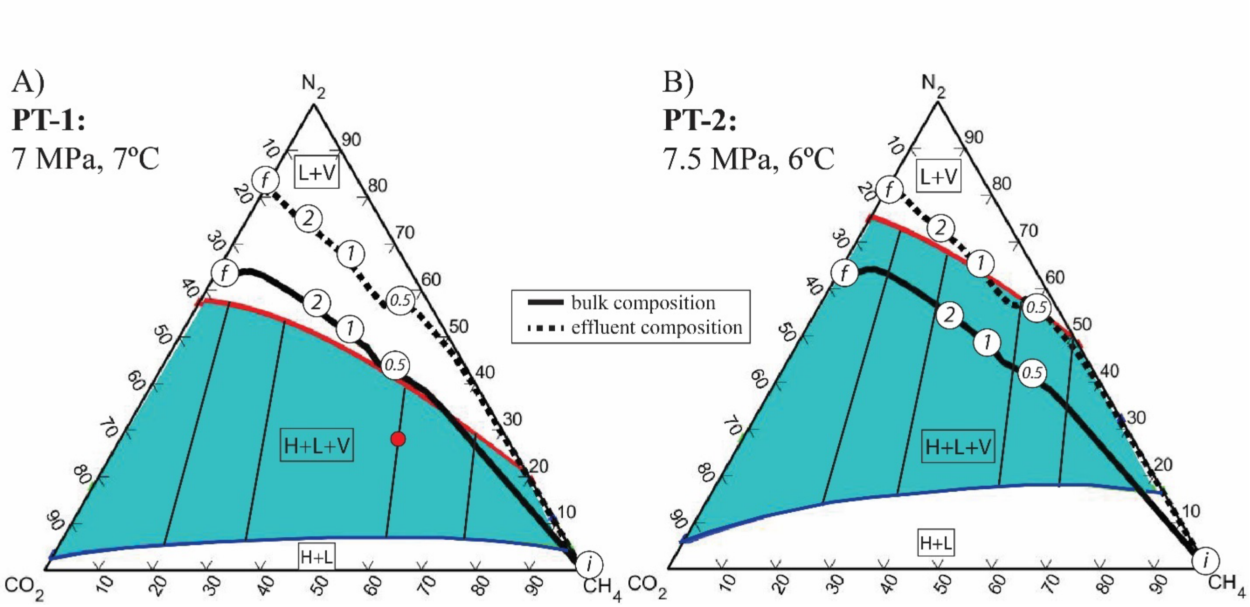

Figure 22 Ternary diagrams of hydrate stability and composition at two PT conditions. The bulk composition (solid black line) and effluent composition (dotted black line) are shown at initial conditions (i), 0.5 PV of gas out, 1 PV of gas out, 2 PV of gas out, and final conditions (f). The shaded region represents the three-phase zone where vapor, liquid and hydrate are present. Above the red line only liquid and vapor are present. Below the blue line, only hydrate and liquid are present. Within the teal region, the vapor and hydrate phase composition are determined by following the tie lines to the respective line: vapor line (red) and hydrate line (blue). For example, at red dot, tie lines can be followed up to vapor and down to hydrate phase composition.

In the teal region, hydrate, liquid, and vapor are stable. Below the blue line, hydrate and liquid are stable. Above the red line, vapor and liquid are stable. Within the three-phase zone, the vapor composition can be determined by projecting the tie line up to the vapor-liquid boundary (red line), and the hydrate composition can be determined by the tie line down to the hydrate-liquid boundary (blue line).

We overlie the bulk vapor molecule composition and the effluent composition during the gas flood (Figure 21B) on the phase diagrams (Figure 22). The solid black line represents the bulk composition determined by our mass balance from initial (i) to final (f) (numbers represent pore volumes of gas out of system). The dotted black line shows the effluent composition from initial (i) to final (f). As we inject flue gas, the bulk composition (black line) becomes more enriched in N_2 and CO_2, and the system enters the three-phase stability zone (teal region, Figure 10). The effluent composition is generally more enriched in N_2 than the bulk composition (compare dotted line to solid line, Figure 22). Initially (until a pore volume of almost 0.5), the effluent becomes more enriched in N_2 but does not have significant CO_2. Thereafter, the effluent becomes more enriched in CO_2 and ultimately it approaches its injection composition.

At PT-1 conditions (Figure 22A), the composition path (solid black line) initially moves through the three-phase stability zone but quickly enters and remains in the V+L zone. At equilibrium conditions for PT-1, we do not predict hydrate to be stable through much of the experiment or at the final composition. However, as the bulk composition initially moves through the three-phase zone (i to 0.5 PV out, Figure 22A), we predict that a mixed hydrate composed of CO_2, N_2, and CH_4 was forming.

In contrast, at PT-2 conditions (Figure 22B), the composition path (solid black line) stays within the three-phase stability zone for the duration of the experiment. Therefore, at

PT-2 conditions, we expect a mixed CO_2, N_2, and CH_4 hydrate to form throughout the experiment and to be stable at the conclusion of the experiment (as predicted by Figure 20 and Figure 21).

Importantly, the final effluent composition lies within the liquid-vapor zone whereas the bulk composition lies within the hydrate-liquid-vapor zone which suggests that this system is not at bulk equilibrium. If injection continued, we expect that the bulk composition would eventually reach the effluent composition causing the remaining hydrate to dissociate.

4.6 MULTIPHASE FLOW MODEL

4.6.1 Interpreted behavior

We interpret the following behavior in our experiments (Figure 23). During injection, three key zones will form. At the front (zone 2, Figure 23), CH_4 and N_2 vapor advance through the medium. In this zone, N_2 invades the initial CH_4 hydrate and causes pure-CH_4 hydrate dissociation and formation of mixed CH_4 and N_2 hydrate and vapor phases. Behind this front, there is a broad three-component zone (CH_4+CO_2+N_2 zone, Figure 23). This new zone will contain CH_4, CO_2, and N_2 which will all be present in the hydrate, vapor, and liquid phase and is where the majority of CO_2 hydrate will form. Finally, there is a tailing CO_2-N_2 region (no CH_4) that will form a mixed CO_2-N_2 hydrate at certain PT conditions (zone 3, Figure 23).

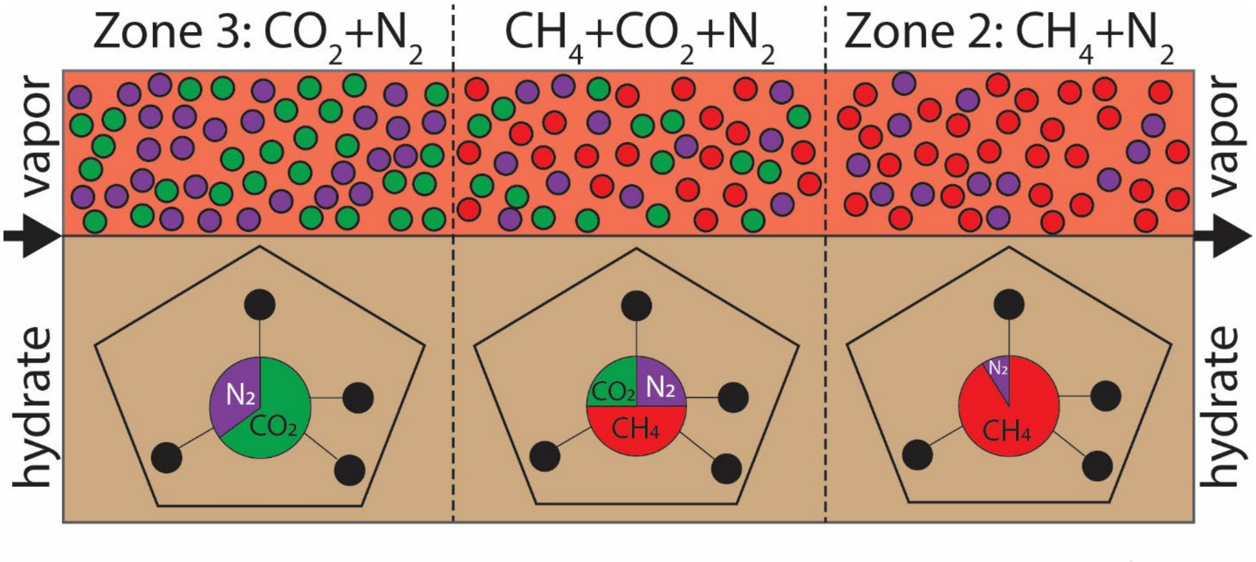

Figure 23 Conceptual cartoon of vapor component molecule partitioning during flue gas injection in slimtube reservoir. The upper (vapor) portion shows the composition of the gas phase (CH_4 (red), N_2 (purple), and CO_2 (green)) during injection. The lower (hydrate) portion shows the composition of the hydrate phase where the center circle represents the composition of the hydrate. As we move from right to left, the CH_4 (red) percentage decreases and the CO_2 (green) percentage increases. The middle section is the three-component zone where all three components (CH_4, CO_2, and N_2) are present in all three phases. We end with a hydrate phase that is composed mostly of CO_2 and vapor phase that is composed mostly of N_2.

4.6.2 Modeled effluent composition

We compare our results to Darnell et al.'s (2019) model of vapor injection into a CH_4 hydrate reservoir at local equilibrium. In the equilibrium model, as in our experiment, the system initially contains water and CH_4 hydrate. Flue gas (N_2 and CO_2) is injected, and the evolving phase saturations and phase compositions are calculated assuming local equilibrium. As the partitioned zones/fronts move through the system, they manifest in the effluent fluid composition (i.e., CO_2 free zone will first appear with only CH_4 and N_2 in effluent). We compare our experimental effluent (S_h=25%) (Figure 24A) with the local equilibrium model with an initial hydrate saturation of 25%. We consider the two pressure and temperature conditions illustrated in Figure 24 (**PT-1**=7 MPa, T=7° C, Figure 24B, and **PT-2**=7.5 MPa, T=6° C, Figure 24C).

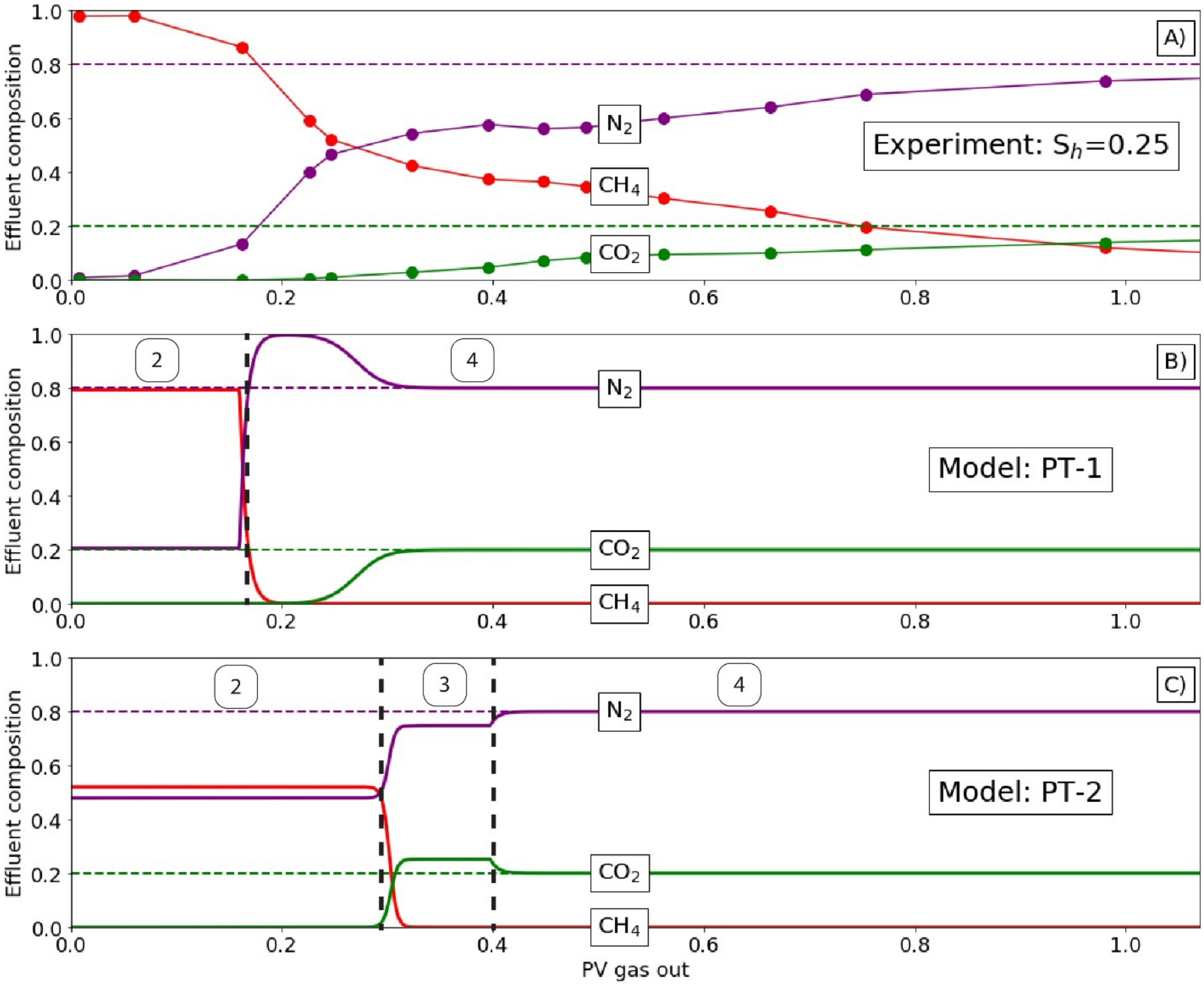

Figure 24 Comparison of experimental gas effluent composition to flow model at two PT conditions (Darnell 2019). **A)** Effluent vapor composition from experiment. **B)** Model effluent composition: $S_{h,initial}$=25%, P=7 MPa, T=7°C. **C)** Model effluent composition: $S_{h,initial}$=25%, P=7.5 MPa, T=6°C.

In all models (Figure 24B/C), the effluent vapor is initially composed of CH_4 and N_2. This zone corresponds to the presence of a CH_4-N_2 mixed hydrate in the downstream region of the core (zone 2, Figure 14B). In PT-1 (Figure 24B), the effluent then abruptly transitions to the injection composition (zone 4, Figure 14B) where no hydrate is stable. Therefore, at PT-1 conditions, no CO_2-N_2 hydrate forms (zone 3, Figure 14B).

However, at PT-2 (Figure 24C), there is zone of CO_2-N_2 and no CH_4 which records the presence of a mixed N_2-CO_2 hydrate (zone 3, Figure 14B). In contrast to PT-1, there is less N_2 and more CO_2 in the system and therefore hydrate remains stable (i.e., the system remains in the hydrate stability zone (teal region, Figure 22B)). After the CO_2 mixed hydrate zone, the system reaches the input mixture and no hydrate is present (zone 4, Figure 14B).

4.6.3 Comparison of flow model to experimental results

The experimental effluent composition (Figure 24A) does not precisely follow the model results (Figure 24B and 22C). As is observed in the model, there is an initial effluent composed of N_2 and CH_4 (Figure 24A, PV=0-0.3). However, with time, a zone of CO_2, CH_4, and N_2 are all present in the effluent (Figure 24A, PV=0.3-2.0). This broad three-component effluent zone is the main difference between the model and experiments. Eventually after multiple pore volumes of gas out, all CH_4 has been removed from the system and the effluent matches the injection composition in both the experiments and model.

It is not surprising that the behavior inferred from our experiments differs from the equilibrium model by Darnell et al (2019). That model does not consider diffusion, temperature or pressure effects of hydrate formation/dissociation, two-dimensional flow behavior, or heterogenous geological properties. Perhaps most importantly, the model assumes instantaneous hydrate formation/dissociation and therefore neglects rate-limiting mass transfer effects and kinetic effects.

Because of these assumptions, all the modeled fronts are shocks (e.g., all CH_4 leaves before CO_2 observed in effluent) and all reactions take place within one pore volume of injected fluid. Since hydrate dissociation and formation are not instantaneous (as the model predicts), the experimental fronts are smoothed out over multiple pore volumes of gas out. Thus, a three-component zone forms in the experiments but not model because of the kinetic effects of hydrate formation/dissociation (Figure 23).

4.6.4 Geophysical implications

The fractionation we study in the laboratory provides insight into how mixed hydrate systems form naturally. For example, Paganoni et al. (2016) found vapor and mixed hydrate (CH_4 & CH_6) below the bottom-simulating reflector and pure methane hydrate above it. They inferred that chemical fractionation of the upward migrating hydrocarbons produced this distribution. This sequential fractionation is the same process we invoke to describe the evolution of the injection of flue gas into a hydrate reservoir. More broadly, the application of reactive transport models to the understanding of how hydrates form and dissociate will further contribute to our understanding of the carbon cycle.

4.7 CONCLUSION

We present experiments where we inject flue gas into a CH_4 hydrate saturated slimtube and measure the effluent vapor composition. The experiments show that the injection of flue gas causes CH_4 hydrate dissociation and production followed by CO_2 mixed hydrate formation and storage. The presence of N_2 is crucial to facilitate flow and initial dissociation of CH_4 hydrate through a connected gas phase. We perform experiments at a range of hydrate saturations that all display similar behavior. The experiments show that hydrate replacement is a multistep process that is controlled by fluid flow and thermodynamic behavior in a multicomponent system. In comparing our experimental results to the multiphase flow simulator developed by Darnell et al. (2019), we show that our results display key differences from previously developed models. Our experiments show the development of a broad three-phase, three-component zone where CH_4, CO_2, and N_2 are stable in the hydrate, liquid, and vapor phase. This three-phase zone develops because of the kinetic effects of hydrate formation and dissociation that previous models do not account for. We present an updated conceptual model for the observed phase and component partitioning during co-injection (Figure 23). Broadly, these results suggest that flue gas injection is a valid method for simultaneous production of CH_4 hydrate and CO_2 storage in a hydrate reservoir.

4.8 REFERENCES

Archer, D., Buffett, B. A., & Brovkin, V. (2008). Ocean methane hydrates as a slow tipping point in the global carbon cycle. *Proceedings of the National Academy of Sciences*, *106*(49), 20596-20601. https://doi.org/10.1073/pnas.0800885105

Birkedal, K. A., Hauge, L. P., Graue, A., & Ersland, G. (2015). Transport mechanisms for co2-ch4 exchange and safe co2 storage in hydrate-bearnig sandstone. *Energies*, *8*. https://doi.org/doi: 10.3390/en8054073

Boswell, R. (2009). Is gas hydrate energy within reach? *Science*, *325*(5943), 957-958. https://doi.org/10.1126/science.1175074

Boswell, R., & Collett, T. (2011). Current prospective on gas hydrate resources. *Energy & Environmental Science*, *4*, 10.

Boswell, R., Schoderbek, D., Collett, T. S., Ohtsuki, S., White, M., & Anderson, B. J. (2017). The Iġnik Sikumi Field Experiment, Alaska North Slope: Design, Operations, and Implications for CO2–CH4 Exchange in Gas Hydrate Reservoirs. *Energy & Fuels*, *31*(1), 140-153. https://doi.org/10.1021/acs.energyfuels.6b01909

Darnell, K. N., Flemings, P. B., & DiCarlo, D. (2019). Nitrogen-Driven Chromatographic Separation During Gas Injection Into Hydrate-Bearing Sediments. *Water Resources Research*. https://doi.org/10.1029/2018wr023414

Darnell, K. N. F., P.B.; DiCarlo, D. (2017). Subsurface injection of combustion power plant effluent as a solid-phase carbon dioxide storage strategy. *Geophysical Research Letters*, *44*, 5521-5530. https://doi.org/10.1002/2017GL073663

Dickens, G. R., O'Neil, J. R., Rea, D. K., & Owen, R. M. (1995). Dissociation of oceanic methane hydrate as a cause of the carbon isotope excursion at the end of the Paleocene. *Paleoceanogr.*, *10*, 965-971.

House, K. Z., Schrag, D. P., Harvey, C. F., & Lackner, K. S. (2006). Permanent carbon dioxide storage in deep-sea sediments. *Proceedings of the National Academy of Sciences*, *103*(33), 12291-12295. https://doi.org/10.1073/pnas.0605318103

Kang, H., Koh, D.-Y., & Lee, H. (2014). Nondestructive natural gas hydrate recovery driven by air and carbon dioxide. *Sci Rep*, *4*. https://doi.org/dx.doi.org/10.1038/srep06616

Khan, S. A., Pope, G. A., & Sepehrnoori, K. (1992). Fluid Characterization of Three-Phase CO2/Oil Mixtures. SPE/DOE Enhanced Oil Recovery Symposium,

Koh, D.-Y., Kang, H., Lee, J.-W., Park, Y., Kim, S.-J., Lee, J., Lee, J. Y., & Lee, H. (2016). Energy-efficient natural gas hydrate production using gas exchange. *Applied Energy*, *162*(Supplement C), 114-130. https://doi.org/https://doi.org/10.1016/j.apenergy.2015.10.082

Konno, Y., Fujii, T., Sato, A., Akamine, K., Naiki, M., Masuda, Y., Yamamoto, K., & Nagao, J. (2017). Key Findings of the World's First Offshore Methane Hydrate Production Test off the Coast of Japan: Toward Future Commercial Production. *Energy & Fuels*, *31*(3), 2607-2616. https://doi.org/10.1021/acs.energyfuels.6b03143

Lee, H., Seo, Y., Seo, Y.-T., Moudrakovski, I. L., & Ripmeester, J. A. (2003). Recovering Methane from Solid Methane Hydrate with Carbon Dioxide. *Angewandte Chemie International Edition*, *42*(41), 5048-5051. https://doi.org/https://doi.org/10.1002/anie.200351489

Masson-Delmotte, V., Zhai, P., Pörtner, H.-O., Roberts, D., Skea, J., Shukla, P. R., Pirani, A., Moufouma-Okia, W., Péan, C., Pidcock, R., Connors, S., Matthews, J. B. R., Chen, Y., Zhou, X., Gomis, M. I., Lonnoy, E., Maycock, T., Tignor, M., & Waterfield, T. (2018). *Global Warming of 1.5°C. An IPCC Special Report on the impacts of global warming of 1.5°C above pre-industrial levels and related global greenhouse gas emission pathways, in the context of strengthening the global response to the threat of climate change, sustainable development, and efforts to eradicate poverty* (IPCC, Issue. https://www.ipcc.ch/sr15/

Milkov, A. V. (2004). Global estimates of hydrate-bound gas in marine sediments: how much is really out there? *Earth-Science Reviews*, *66*(3–4), 183-197. https://doi.org/https://doi.org/10.1016/j.earscirev.2003.11.002

Murphy, Z. W., DiCarlo, D. A., Flemings, P. B., & Daigle, H. (2020). Hydrate is a Nonwetting Phase in Porous Media. *Geophysical Research Letters*, *47*(16), e2020GL089289. https://doi.org/https://doi.org/10.1029/2020GL089289

Ohgaki, K., Takano, K., Sangawa, H., Matsubara, T., & Nakano, S. (1996). Methane exploitation by carbon dioxide from gas hydrates—phase equilibria for CO2-CH4 mixed hydrate system—. *Journal of chemical engineering of Japan*, *29*(3), 478-483.

Ota, M., Abe, Y., Watanabe, M., Smith, R. L., & Inomata, H. (2005). Methane recovery from methane hydrate using pressurized CO2. *Fluid Phase Equilibria*, *228-229*, 553-559. https://doi.org/https://doi.org/10.1016/j.fluid.2004.10.002

Paganoni, M., Cartwright, J. A., Foschi, M., Shipp, R. C., & Van Rensbergen, P. (2016). Structure II gas hydrates found below the bottom-simulating reflector. *Geophysical Research Letters*, *43*(11), 5696-5706. https://doi.org/10.1002/2016GL069452

Park, Y., Kim, D.-Y., Lee, J-W., Hyh, D.-G., Park, K.-P., Lee, J., & Lee, H. (2006). Sequestering carbon dioxide into complex structures of naturally occuring gas hydrates. *Proceedings of the National Academy of Sciences*, *103*, 12,690-12694. https://doi.org/https://doi.org/10.1073/pnas.0602251103

Ruppel, C. D., & Kessler, J. D. (2017). The interaction of climate change and methane hydrates. *Reviews of Geophysics*, *55*(1), 126-168. https://doi.org/https://doi.org/10.1002/2016RG000534

Sakai, H., Gamo, T., Kim, E.-S., Tsutsumi, M., Tanaka, T., Ishibashi, J., Wakita, H., Yamano, M., & Oomori, T. (1990). Venting of Carbon Dioxide-Rich Fluid and Hydrate Formation in Mid-Okinawa Trough Backarc Basin. *Science*, *248*(4959), 1093-1096. https://doi.org/doi:10.1126/science.248.4959.1093

Schicks, J. M., Strauch, B., Heeschen, K. U., Spangenberg, E., & Luzi-Helbing, M. (2018). From Microscale (400 µl) to Macroscale (425 L): Experimental Investigations of the CO2/N2-CH4 Exchange in Gas Hydrates Simulating the Iġnik Sikumi Field Trial. *Journal of Geophysical Research: Solid Earth*, *123*(5), 3608-3620. https://doi.org/https://doi.org/10.1029/2017JB015315

Schoderbek, D., & Boswell, R. (2011). Iġnik Sikumi# 1, gas hydrate test well, successfully installed on the Alaska North Slope. *Natural Gas & Oil*, *304*, 285-4541.

Schuur, E. A. G., Bockheim, J., Canadell, J. G., Euskirchen, E., Field, C. B., Goryachkin, S. V., Hagemann, S., Kuhry, P., Lafleur, P. M., Lee, H., Mazhitova, G., Nelson, F. E., Rinke, A., Romanovsky, V. E., Shiklomanov, N., Tarnocai, C., Venevsky, S., Vogel, J. G., & Zimov, S. A. (2008). Vulnerability of Permafrost Carbon to Climate Change: Implications for the Global Carbon Cycle. *BioScience*, *58*(8), 701-714. https://doi.org/10.1641/b580807

Sloan, E. D., & Koh, C. A. (2007). *Clathrate Hydrates of Natural Gases*. CRC Press.

Smith, D. H., Seshadri, K., & Wilder, J. W. (2001). *Assessing the Thermodynamic Feasibility of the Conversion of Methane Hydrate into Carbon Dioxide Hydrate in*

Porous Media Conference: National Conference on Carbon Sequestration, Washington DC, (United States), 15-17 May 2001; Related Information: Presentation given at the First National Conference on Carbon Sequestration, United States.

You, K., Kneafsey, T. J., Flemings, P. B., Polito, P., & Bryant, S. L. (2015). Salinity-buffered methane hydrate formation and dissociation in gas-rich systems. *Journal of Geophysical Research: Solid Earth*, *120*(2), 643-661. https://doi.org/10.1002/2014JB011190

Appendix A: Supplemental material for Chapter 2

All experimental data and code for this chapter can be found at:

https://github.com/zwmurphy/hydrate_non_wetting_data.

A1. NOMENCLATURE

Symbol	Name	Unit
l	liquid phase	(-)
g	free gas phase	(-)
h	hydrate phase	(-)
w	water	(-)
m	methane	(-)
ΔP	pressure drop	(Pa)
μ	viscosity	(Pa·s)
ρ_l	liquid phase density	(g m^{-3})
ρ_g	gas phase density	(g m^{-3})
ρ_h	solid hydrate density	(g m^{-3})
k_{abs}	absolute permeability	(m^2)
$k_{eff,w}$	effective permeability of water	(m^2)
$k_{eff,g}$	effective permeability of gas	(m^2)
$k_{r,w}$	relative permeability of water	(-)
$k_{r,g}$	relative permeability of gas	(-)
M_w	water molecular mass	(g mol^{-1})
M_m	methane molecular mass	(g mol^{-1})
M_h	hydrate molecular mass	(g mol^{-1})
m_w	mass of water	(g)
m_m	mass of methane	(g)
m_h	mass of hydrate	(g)
mol_w	mol of water	(mol)
mol_g	mol of gas	(mol)
mol_h	mol of hydrate	(mol)
n_w	water fitting parameter	(-)
n_g	gas fitting parameter	(-)
N	hydrate number for SI methane hydrate	(-)
Q_w	volumetric flow rate of water	(m^3 s^{-1})
Q_g	volumetric flow rate of gas	(m^3 s^{-1})
f_w	fractional flow rate of water	(-)
S_w	water phase saturation	(-)

$S_{w,i}$	initial water phase saturation	(-)
$S_{w,f}$	final water phase saturation	(-)
S_{rw}	Residual water saturation	(-)
S_g	methane gas phase saturation	(-)
$S_{g,i}$	initial gas phase saturation	(-)
$S_{g,f}$	final gas phase saturation	(-)
S_{rg}	residual gas saturation	(-)
S_h	solid hydrate phase saturation	(-)
ϕ	sample porosity	(-)
r	sample radius	(m)
L	sample length	(m)
A	cross-sectional area	(m^2)
V_{pore}	pore volume	(m^3)
V_{tot}	total sample volume	(m^3)
V_{eff}	total effective volume	(m^3)
V^w	volume of water	(m^3)
V^m	volume of methane	(m^3)
V^h	volume of hydrate phase	(m^3)

A2. SAMPLE PREPARATION AND HYDRATE FORMATION PROCEDURE

A step-by-step procedure for forming hydrates and running a steady state relative permeability measurement is given below. Parts of this procedure were originally publish in my master's thesis. The same sample preparation and hydrate formation procedure were used for both Chapter 2 and Chapter 3.

Sample preparation

1. Place core sample (24" length, 1.5" diameter) in core holder
2. Insert porous stones and filters at top and bottom of core
3. Insert bottom and top cap of core holder
4. Attach pump and flow 1-2 PV of 3.5% NaCl brine through core
5. Close downstream end of core and attach vacuum pump to upstream end
6. Pull vacuum on core to remove all remaining air
7. Release vacuum and allow brine to be pulled into core
8. May need to repeat 1-2 more times
9. At this point, core is fully brine saturated and ready for experiments

Low saturation method

1. Once sample is fully brine saturated, attach gas pump to upstream end of core
2. Flow gas at constant rate and collect water on downstream
3. Flow gas until approx.. 15-25 ml of water is removed from system (~.2-.3 PV)
4. Sample is partially saturated with gas and methane
5. Proceed to transducer preparation and pressurization

High saturation method

1. Sample should begin fully dry (baked in oven to remove all water)
2. Gas is injected to fully saturate core with methane
3. Inject desired amount of water (~25-50 mL)
    a. Highest hydrate saturation is achieved when initial gas saturation is ~0.5
    b. Water should be injected at low flow rate to better distribute water
4. Proceed to transducer preparation and pressurization

Transducer preparation

1. Close transducer valves to core
2. Open all transducer valves so transducer system is open
3. Connect ISCO pump to transducer line
4. Inject >10% NaCl brine into transducer lines until pressurized to >1400 psi
5. Open vent fitting on each transducer to purge all air from system
a. Must be completed for each side on each transducer
6. Allow system to return to 1400 psi
7. Zero all transducers on Labview VI
8. Close of pump valve
9. Shut valve (green) on each transducer
a. dP should remain 0 psi for each transducer
10. Disconnect pump from transducer line

Pressurization Technique

1. With cart at room temperature, close outlet valve and open gas inlet valve (attached to ISCO pump)
2. Begin ALL data collection
3. Completely purge ISCO pump, then refill with air so pump reads completely full but is empty
4. Connect ISCO methane pump to methane source
    a. Pump will be connected to methane tank on one side and core on other side
    b. Pump will not be running
5. Attach Quizix pump to bottom confining inlet
6. Add confining fluid until confining volume is completely purged of air
    a. Seal confining fluid
7. Increase confining pressure to ~400 psi

8. Open methane source and increase pressure with regulator slowly to ~75 psi
    a. Monitor pump psi (not regulator) to confirm pressure
9. Increase confining and pore pressure in alternating steps of 100 psi until desired pressure is reached
    a. Always make sure pore pressure is always below confining, this core holder WILL leak if pore pressure>confining pressure
    b. Go as slowly as possible to insure that sand is not disturbed
10. Once desired pressure is reached (1250 psi) close off valve to methane supply
11. Detach system from methane supply
12. Set ISCO pump to constant pressure mode and maintain pore pressure of 1250 psi
13. Perform leak test on set up and make sure the pump holds 1250 psi with very little/no leaks
14. Open pressure transducer lines and allow system to reach equilibrium
15. Once pressure transducer are reading a dP of zero and system is leak free, prepare to move cart into cold room
16. Unplug power supply and wheel cart (minimum 2 ppl) into cold room
17. Immediately plug in power supply (can only run for ~10 min on battery)
18. Make sure pump is still operating and maintaining pressure of 1250 psi and data collection is enabled
19. Leave cart in cold room for minimum 2 days to allow for hydrate formation
    a. Ideally 5+ days to allow more conversion

Pressure cycling and reaching three-phase stability

1. Using code from You (2015), estimate three-phase salinity
2. Make brine of that salinity
3. Set BPR to three-phase pressure
4. Using Quizix pump, inject brine for 2-3 pore volumes
5. To ensure three-phase stability, lower pressure very slowly and watch for pressure rebounds
6. Hydrate should just begin to dissociate and then pressure rebound will be at three-phase stability
    a. I have noticed that three-phase stability pressure is slightly below (25-50 psi) what is estimated from code
7. Gas should be purged from the sample and should be only hydrate and water
8. Change pump to constant pressure at three-phase pressure
9. Shut in valve before BPR so no flow will occur
10. Allow sample to sit at three-phase conditions
11. Decrease pressure to 50-100 psi below stability
12. Allow sample to sit for ~8 hours
13. Increase pressure to three-phase conditions
14. Allow sample to sit for ~8 hours
15. Increase pressure to 50-100 psi above stability
16. Allow sample to sit for ~8 hours

17. Return sample to three-phase conditions
18. Allow sample to equilibrate for 8 hours
19. This cycling can be completed multiple times to improve distribution
20. After cycling, the transducers should still be reading 0 psi
    a. If not, transducers must be re-zeroed

Injection of gas and brine

1. Connect Quizix pump to brine inlet
2. Have supply of three-phase brine
3. Connect MFC to gas inlet
4. Connect MFC to gas supply
5. Pressurize MFC line to above pore pressure before opening valve to core
6. Zero scale at effluent collection point to begin mass balance tracking
7. Begin brine flow and open BPR to maintain pressure in core
8. Open gas valve and allow gas to flow
9. Run at multiple injection ratios to change gas and brine ratio
10. Start with low gas saturation (high brine flow/low gas flow) and move to high gas saturation (high gas flow/low brine flow)
11. Allow each injection ratio to reach steady state (1-2 pore volumes of fluid injected)

Data collection

1. Data collection must be run through entire experiment
2. During hydrate formation, must collect data for ISCO pump volume
3. During injection, MFC, flow meter, and Quizix pump flow rates and injection volumes must be logged
4. During flow, there should be a scale to measure the effluent from the core to determine the saturation using mass balance

Degassing

1. Once all flow experiments have been conducted sample must be degassed to determine hydrate saturation
2. Shut in all valves to core (inlet, outlet, pressure taps)
3. Make sure outlet pressure transducer is collecting data
4. Connect degassing vessel to outlet and to vent
5. Using degassing method from Phillips 2018, slowly drop pressure in core and measure amount of methane released
6. There will be small amounts of free gas before hydrate dissociation
7. Pressure will not rebound
8. Once hydrate is dissociating, pressure will rebound
9. Once pressure rebounds, continue slowly degassing until the pressure is zero
10. Record all pressures and volumes of methane released
11. After initial free gas, all remaining methane is from hydrate

12. Using volume of methane, hydrate saturation can be determined
13. Compare with estimates from initial saturation from excess gas method

A3. MASS BALANCE ANALYSIS

To calculate the phase saturations throughout our experiments, we monitored all fluid inputs and outputs to the core. This methodology allowed us to determine the phase saturation at each timestep (Figure 5B).

In a methane hydrate system, there are **three** phases (liquid, gas, and hydrate) and **three** components (water, methane, and salt). The liquid brine (S_l), methane gas (S_g), and solid hydrate (S_h) bulk phase saturations all sum to 1. The pore volume (V_p) is known for the sample. The total mass (N_w, N_m, N_s) of each component can be calculated:

$$1 = S_h + S_l + S_g \tag{1}$$

$$N_w = \left(X_w^l \rho_l S_l + X_w^g \rho_g S_g + X_w^h \rho_h S_h\right) V_p \tag{2}$$

$$N_m = \left(X_m^l \rho_l S_l + X_m^g \rho_g S_g + X_m^h \rho_h S_h\right) V_p \tag{3}$$

$$N_s = \left(X_s^l \rho_l S_l + X_s^g \rho_g S_g + X_s^h \rho_h S_h\right) V_p \tag{4}$$

X is the mass fraction of a single component in each phase. The mass fractions for each phase must sum to 1:

$$1 = X_w^l + X_m^l + X_s^l \tag{5}$$

$$1 = X_w^g + X_m^g + X_s^g \tag{6}$$

$$1 = X_w^h + X_m^h + X_s^h \tag{7}$$

The mass fraction of gas and water in hydrate (X_w^h, X_m^h, X_s^h) are assumed based on Structure I hydrate. The mass fraction of water and salt (X_w^g , X_s^g) in the gas phase are assumed to be 0. The solubility of methane in water (X_m^l) is assumed to be 0.

Hydrate is assumed to be incompressible and has a known density ($\rho_h = 912\ kg\ m^{-3}$). The density of brine and gas can be calculated at each step based on pressure (P), temperature (T), and salinity (X_s^l):

$$\rho_g = \frac{m}{\underline{V}} = \frac{P}{ZRT} \quad (8)$$

$$Z^3 + (-1 + B)Z^2 + (A - 3B^2 - 2B)Z - AB + B^2 + B^3 = 0 \quad (9)$$

$$\rho_l = \rho_w + \frac{N_s}{S_l V_p} \quad (10)$$

The Peng-Robinson equation of state (PREOS) is used to solve for molar density (mol m^{-3}) of CH$_4$. R is the specific gas constant (R=8.314 J/mol-K), and pressure and temperature are variables. Z is the compressibility factor at each P-T condition. The density of brine is calculated as a function of temperature and salinity.

Appendix B: Supplemental material for Chapter 3

All experimental data and code for this chapter can be found at: https://github.com/zwmurphy/three_phase_rel_perm.

B1. NOMENCLATURE

Symbol	Name	Unit
l	liquid phase	(-)
g	free gas phase	(-)
h	hydrate phase	(-)
w	water	(-)

ΔP	pressure drop	(Pa)
μ	viscosity	(Pa·s)
ρ_l	liquid phase density	(g m^{-3})
ρ_g	gas phase density	(g m^{-3})
ρ_h	solid hydrate density	(g m^{-3})
k_{abs}	absolute permeability	(m^2)
$k_{eff,w}$	effective permeability of water	(m^2)
$k_{eff,g}$	effective permeability of gas	(m^2)
k_{rw}	relative permeability of water	(-)
k_{rg}	relative permeability of gas	(-)
n_w	water fitting parameter	(-)
n_g	gas fitting parameter	(-)
N	hydrate number for SI methane hydrate	(-)
Q_w	volumetric flow rate of water	(m^3 s^{-1})
Q_g	volumetric flow rate of gas	(m^3 s^{-1})
f_w	fractional flow rate of water	(-)
S_w	water phase saturation	(-)
S_{rw}	residual water saturation	(-)
S_g	methane gas phase saturation	(-)
S_{gr}	residual gas saturation	(-)
S_h	solid hydrate phase saturation	(-)
ϕ	phase (e.g., 2ϕ or 3ϕ)	(-)
r	sample radius	(m)
L	sample length	(m)
A	cross-sectional area	(m^2)
V_p	pore volume	(m^3)
V_i	volume of phase i	(m^3)
σ_{iy}	interfacial energy between phase i and y	(J m^{-2})
P_c	capillary pressure	(Pa)

B2. SUPPLEMENTAL FIGURES FROM CHAPTER 3

These figures are supplemental to Chapter 3: Gas and water relative permeability in CH_4 hydrate systems. These figures provide more context, a different visualization, or additional analyses that were not included in the final publication submission.

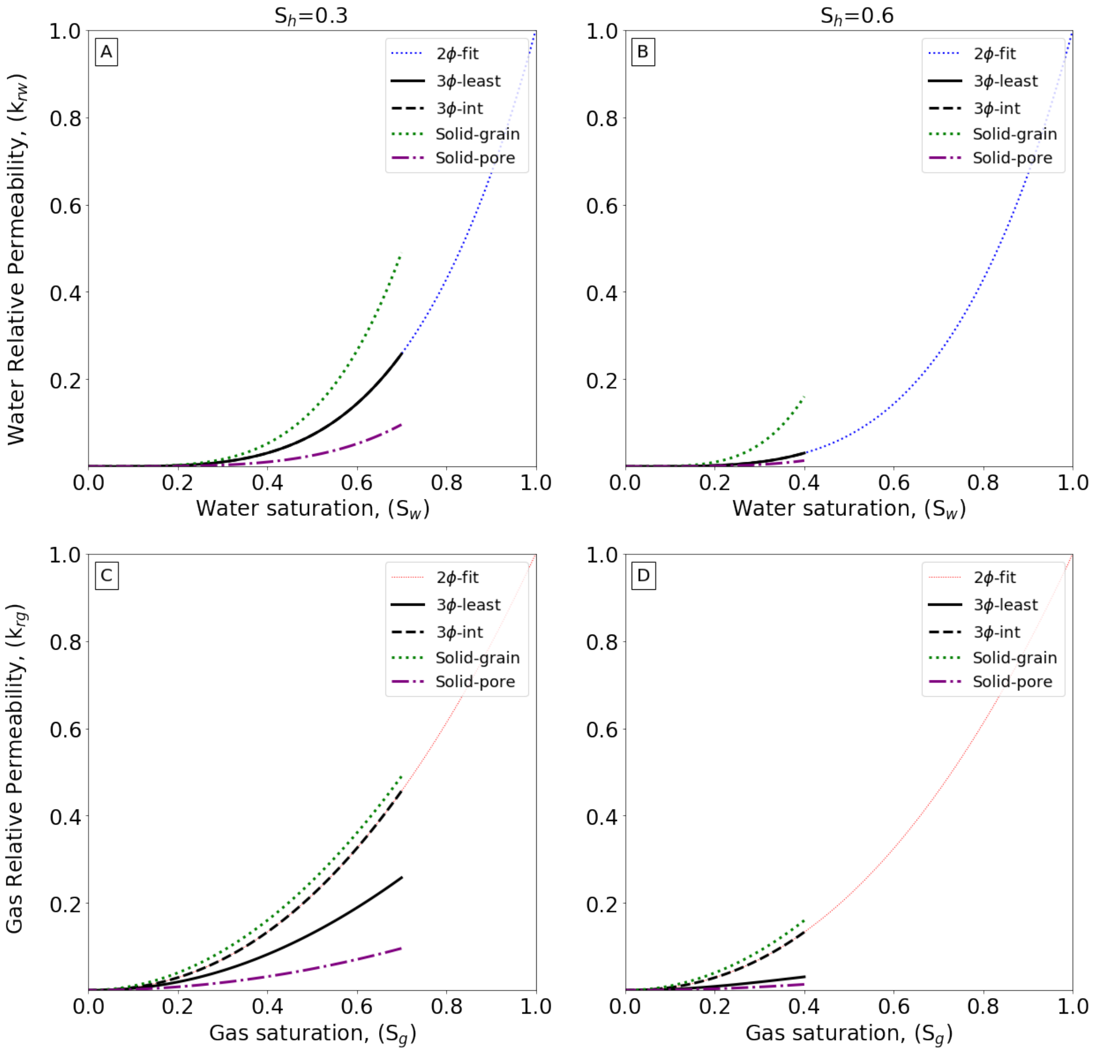

Figure 25 Model comparison (Figure 11) with linear-linear axis. Relative permeability is traditionally plotted on linear axes so readers may be more accustomed to seeing relative permeability plots like this. These plots also highlight the difference in permeability at higher gas or water saturation.

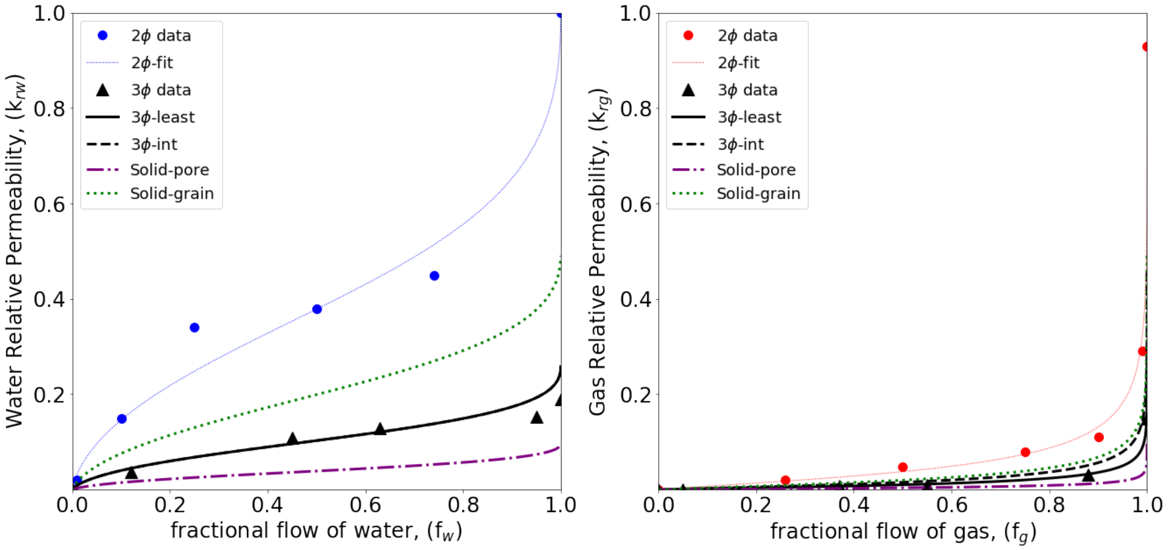

Figure 26 Figure 12 with a linear axis. This figure is included as a different visualization of the data presented in Chapter 3.

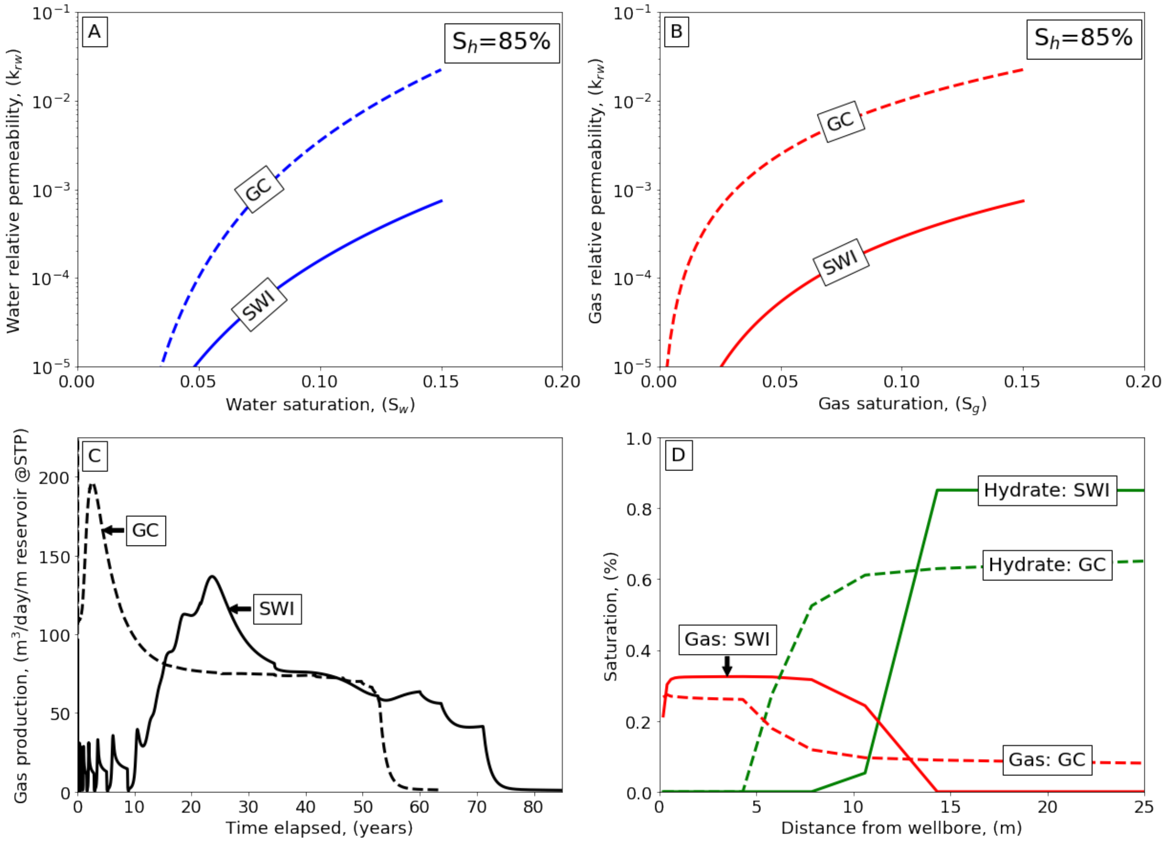

Figure 27 Comparison of production model using the three-phase least model (SWI) and the solid-grain (GC) model. A) Comparison of SWI (3Φ-int) model to the GC (solid-grain) model for water relative permeability. B) Comparison of SWI (3Φ-int) model to the GC (solid-grain) model for gas relative permeability. C) Modeled gas production rate using each permeability model. The model is developed by Kehua You. The SWI model predicts much lower gas production rates. This is controlled by the lower water relative permeability. This low permeability causes blockages at the beginning which is why flow starts and stops from year 0-10. D) Comparison of the modeled saturation front of gas and hydrate moving away from the wellbore.

Appendix C: Supplemental material for Chapter 4

All experimental data and code for this chapter can be found at: https://github.com/zwmurphy/CO2_mixed_hydrate_slimtube.

C1. NOMENCLATURE

Symbol	Name	Unit
l	liquid phase	(-)
g	free gas phase	(-)
h	hydrate phase	(-)
m_w	moles of water components	(mole)
m_v	moles of vapor components	(mole)
S_l	liquid phase saturation	(-)
S_g	gas phase saturation	(-)
S_h	hydrate phase saturation	(-)
V_p	pore volume	(m^3)
ρ_g	gas phase density	($mole/m^3$)
ρ_l	liquid phase density	($mole/m^3$)
ρ_h	hydrate phase density	($mole/m^3$)
X_u^i	mass fraction of component (u) in phase (i)	(-)
k_{abs}	absolute permeability	(m^2)
Q	flow rate	(m^3/s)
μ	viscosity	(Pa·s)
P	pressure	(Pa)
L	length	(m)
A	area	(m^2)

C2. SLIMTUBE SAMPLE PREPARATION

This section presents an overview for building the slimtube apparatus, packing it with sand, and forming hydrate in the slimtube.

Slimtube Assembly

1. Select a pressure transducer for the upstream and downstream end of sample
    a. Calibrate transducers and ensure compatible with labview software
2. Silver solder both pressure transducers to a HiP connection
3. Attach each pressure transducers to a HiP valve

4. Measure the ID of the slimtube and calculate the total volume using the length from the manufacturer, subtracting out anything that was cut off
5. Attach a ¼” swage fitting to both ends of the slim tube
6. Run compressed air through the tube to get rid of any metal shavings from cutting the tube
7. Add a ¼” T union to both ends of slimtube
8. To one side add a ¼” to 1/16” reducing tube stub then add filter
9. To the filtered end, feed a 1/16” SS thermocouple through the ¼” to 1/16” tube stub and ¼” T union into the tube
   a.

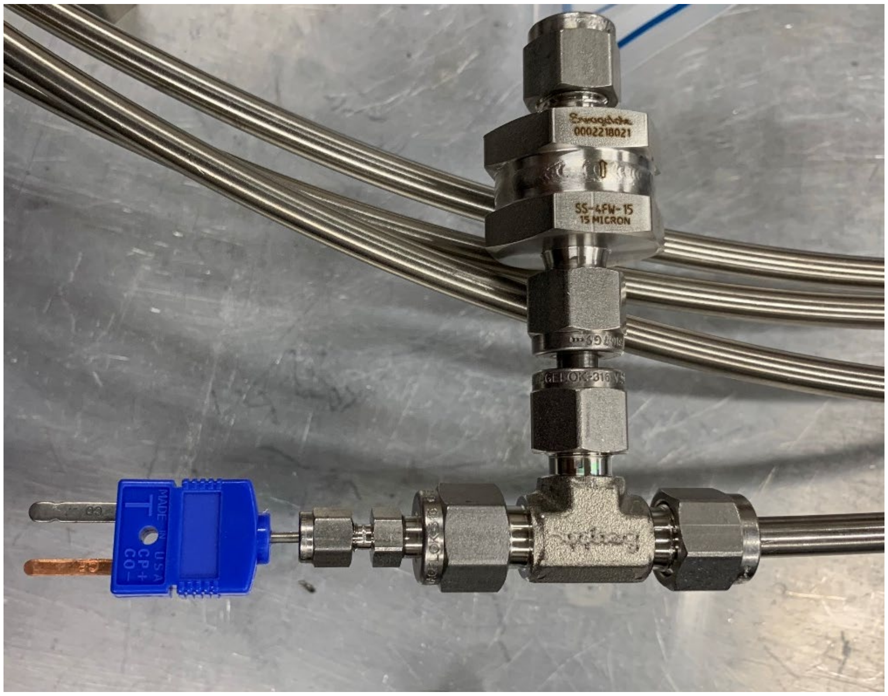

10. *REPEAT AT BOTH ENDS AFTER FILLING WITH SAND*

Sand Packing

1. Fill sand at end without filter (Step 9 above)
2. Calculate the mass of dry 250-micron sand required for 30% porosity
3. Weigh sand so that there is at least 1.5 times the mass required for 30% porosity in slimtube
4. Lay out a tray to catch any sand that falls out while pouring
5. Pour the sand into the tube using a funnel until the funnel fills, then pour any sand in the funnel back into the pouring device, cover the filling end with tape, hold the tube vertically with the filling end on the left, and slowly rotate clockwise facing the tube 5 times
6. After 5 rotations check if you can see sand down the filling end then hang the tube on a ring stand with the filling end covered

7. Use a pneumatic vibrator for 10 minutes to consolidate sediment
8. Repeat step 5 until you are left with ~40% porosity (from total sand in tube)
9. Weigh the mass of the sand remaining in the pouring device and the tray
10. Put the data into the porosity calculation
11. Porosity calculation:
    a. $n = \frac{V_{total} - V_{sand}}{V_{total}}$ $V_{sand} = \frac{m_{sand\ total} - m_{sand\ remaining}}{\rho_{sand}}$
12. Once you reach <40% porosity cap the filling end clean any remaining sand and attach the remaining filter to the filling end

Hydrate formation in slimtube

1. Begin ALL data collection
2. Completely purge ISCO pump, then refill with air so pump reads completely full but is empty
3. Connect ISCO methane pump to methane source
    a. Pump will be connected to methane tank on one side and core on other side
    b. Pump will not be running
4. Set BPR to desired pressure (~1200 psi) and SHUT in above BPR so no flow will occur
5. Open methane source and increase pressure with regulator slowly to ~75 psi
    a. Monitor pump psi (not regulator) to confirm pressure
6. Increase confining and pore pressure in alternating steps of 100 psi until desired pressure is reached
    a. Go as slowly as possible to ensure that sand is not disturbed
7. Once desired pressure is reached (2000 psi) close off valve to methane supply
8. Detach system from methane supply
9. Completely shut in slimtube system so upstream and downstream end are closed
10. Perform leak test on set up and make sure the system holds pressure
11. Leave sample to allow for hydrate formation
    a. Hydrate formation is observed by pressure decrease
    b. As pressure continues to decrease, hydrate formation rate will slow
    c. Leave sample for 14+ days to allow more hydrate conversion
12. If a higher hydrate saturation is desired, the pressure can be increased to 2000 psi again by reconnecting the methane source and starting at Step 5.
    a. Make sure pressure in methane source is ABOVE sample pressure before opening
    b. Make sure to note beginning pressure (low) and end pressure (high) to calculate the additional moles added to the system
    c. Repeat as many times as necessary to reach a higher hydrate saturation

*NOTE: this increases uncertainty in hydrate saturation calculation since you must know exactly how many moles of CH_4 are in system to calculate saturation

C3. GAS SAMPLING AND CHROMATOGRAPHY PROCEDURE

This section is an overview of the gas sampling protocol for the Chapter 4. This describes the gas collection method, the sampling plan, and the gas chromatography analysis.

Gas collection

To understand the composition of the effluent gas, I collected gas samples at regular intervals to be run in the gas chromatography lab. This procedure was developed after much testing and countless experiments.

1. **Prepare gas bags:** Collect ~30 gas bags (15 ml) and place each bag on a vacuum pump for ~ 1 minute to remove any air/contamination. Make sure bags are sealed and no additional air enters the bags. Creaete labels for each bag that have test and sample number. (e.g., ST001-1, ST001-2)
2. **Prepare gas collection point**: Gas samples are collected downstream of the gas/water separator and the gas flow meter. There is a three-way valve that sends gas to the gas sample or to be vented. Before beginning gas flow, ensure gas sampling system is set up and purged of any remaining gas. Do not put a gas bag on the collection point until gas flow has started.
3. **Collect samples**: Once gas flow begins, initially only water will be removed from the system. During this step, ensure that the three-way valve goes to the vent. Immediately when the first gas is observed, switch the valve to the sampling point. NO SAMPLE BAG SHOULD BE ATTACHED. Allow the gas to flow through the sampling point for ~10 seconds to purge the system. After 10 seconds, attach a

sampling bag and fill. The bag will fill very quickly during the initial gas breakthrough. Once sample is collected, write the time of collection on the label. The final label should read something like: **ST001-1, 14;22** or **ST001-5, 14;25.**

4. **Sampling interval:** Repeat this sampling procedure at regular intervals during the gas flood. At the beginning of gas breakthrough, samples should be taken consecutively. Once the flow rate stabilizes (~10 minutes after gas breakthrough), samples should be taken every ~0.1 PV of gas out. Based on the flow rate, this is about 1 sample every 10 minutes. It is most important to collect samples over the first 90 minutes. After 90 minutes, the sampling rate can be decreased to approximately 1 per hour until the end of gas injection. For each test, there should be about 25-30 samples collected.

Gas chromatography analysis

Once the samples have been collected and gas flow has ended, the samples should be run in the gas chromatography lab. Ideally, these should be run within 24-48 hours as the gas bags are not perfectly sealed and can leak or be contaminated over time.

1. **Calibrate GC:** Before running any samples in the GC, the system must be calibrated for the desired fluids (CH_4, N_2, and CO_2). There are three standards to be used for calibration: **1.** 80% CO_2-19% CH_4 -1% N_2, **2.** 80% N_2-19% CO_2 -1% CH_4, and, **3.** 80% CH_4-19% N_2 -1% CO_2. These standards are purchased with exact known concentrations. Before running the standards, two ‘blanks’ should be run to purge the system. With the sample inlet closed, a sample should be loaded and

labeled ‘blank’. Next, one sample should be run for each standard. These standards are then used for the calibration curve for each test (e.g., Figure 28).

2. **Run Samples:** Run each sample in GC using established lab methodology. The pressure of the sample before and after loading should be noted. Each sample is loaded, injected into GC, then run. Each sample takes ~20 minutes to run. The data file is automatically saved to the computer and the peak values for each gas should be input to the spreadsheet with the time, sample number, N_2 peak, CO_2 peak, and CH_4 peak. Using the calibration from Step 1. The percentage of each gas is determined. Examples of the spreadsheet, calibration, and datasheet are shared below.

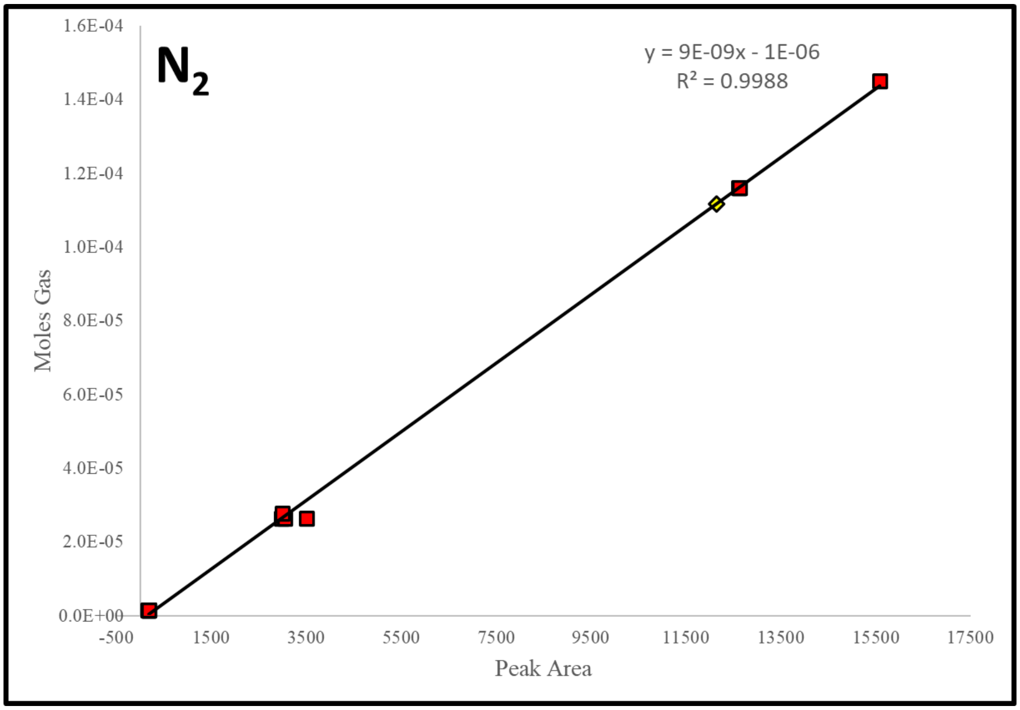

Figure 28 Example calibration data for N_2. These points are all taken from standard samples. There is a calibration curve for each gas of interest: CO_2, N_2, and CH_4. Since each gas sample has a known concentration (from Airgas), the calibration curve should give the exact % concentration for each gas from the standard. For example, the N_2 values above at ~3500 corresponds to a N_2 concentration of 19% which is exactly the concentration of the standard.

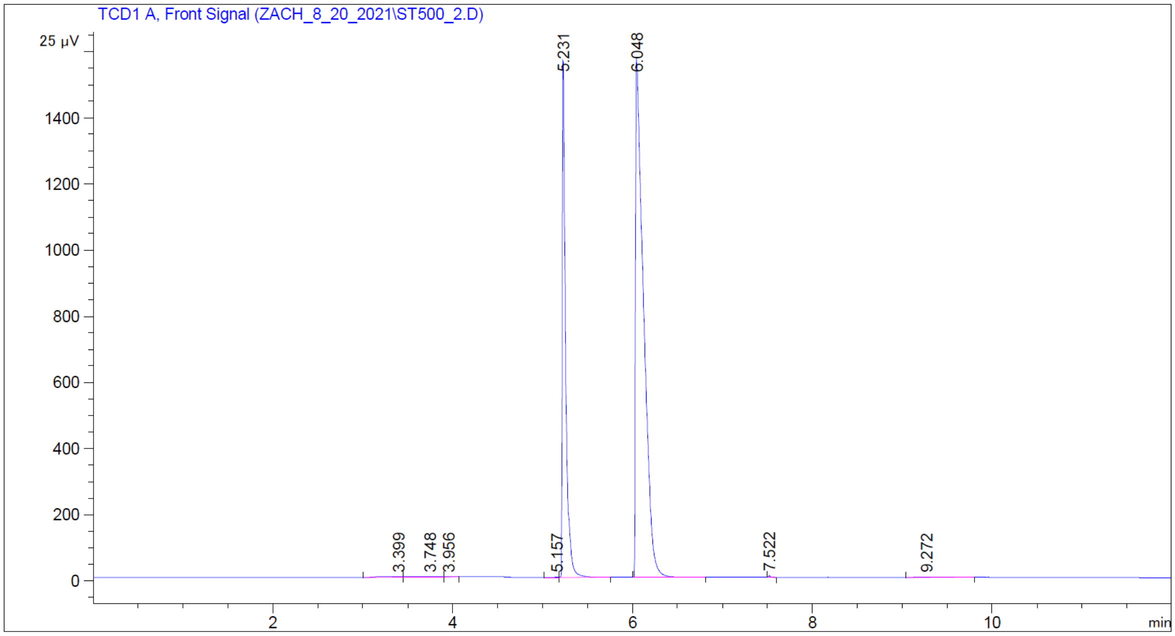

Figure 29 Results from GC report. Area under each peak represents the amount of each phase present in each sample. The first peak (5.321) represents CH_4 and the second peak (6.048) represents N_2.

C4. MOLE BALANCE

This mole balance analysis is modified from Murphy (2020). In our mixed hydrate system, there are three phases (liquid, gas, and hydrate) and five components (H_2O, CH_4, CO_2, N_2, and NaCl). We define the water components as NaCl and H_2O. NaCl can be present only in the water phase. H_2O can be present in the liquid or hydrate phase. The remaining components (CH_4, CO_2, and N_2) are defined as the vapor component molecules. The vapor component molecules can be present in the liquid, gas, or hydrate phase.

The liquid brine (S_l), vapor (S_g), and solid hydrate (S_h) bulk phase saturations in the sample can be calculated using a mole balance analysis. The saturations of all phases sum to 1. The total moles (m_w, m_v) of each component(s) can be calculated with a mole balance:

$$1 = S_h + S_l + S_g \tag{1}$$

$$m_w = \left(X_w^l \rho_l S_l + X_w^g \rho_g S_g + X_w^h \rho_h S_h\right) V_p \tag{2}$$

$$m_v = \left(X_v^l \rho_l S_l + X_v^g \rho_g S_g + X_v^h \rho_h S_h\right) V_p \tag{3}$$

where V_p is the pore volume, X is the mole fraction of a single component in each phase, ρ_g is the gas density (eq. 10), ρ_l is the brine density (eq. 11), and ρ_h is the hydrate density (Table 1).

X is the mole fraction of a component(s) in each phase. The mole fractions for each phase must sum to 1:

$$1 = X_w^l + X_v^l + X_s^l \tag{5}$$

$$1 = X_w^g + X_v^g \tag{6}$$

$$1 = X_w^h + X_v^h \tag{7}$$

The mole fraction of gas and water in hydrate (X_w^h, X_m^h) are assumed based on Structure-I hydrate and do not change as the composition of the vapor component changes. The solubility of gas in water (X_v^l) is assumed to be constant for the duration of the experiment (Table 2).

The sample begins fully brine saturated with an initial water saturation of $S_{w,i} = 1$. Therefore, the initial moles of each component in the sample are known $(m_{w,i}, m_{v,i})$. The initial pressure and temperature of the system are P_i and T_i, respectively. After initial saturation, any input into the system is measured with pumps or MFC (m_w^{in}, m_v^{in}) and any output is measured using a scale and gas flow meter (m_w^{out}, m_v^{out}). The moles of salt removed from the system (m_s^{out}) is unknown, and we therefore assume the effluent has a constant salinity of 3.5% NaCl. The total moles of each component in the system (m_w, m_v) can be solved at all time steps of the experiment (eqs. 8-10).

$$m_w = m_{w,i} + m_w^{in} - m_w^{out} \tag{8}$$

$$m_v = m_{v,i} + m_v^{in} - m_v^{out} \tag{9}$$

There is a known volume of tubing, fittings, and other dead space that has been estimated and accounted for in the mass balance calculations.

Hydrate is assumed to be incompressible and has a known density ($\rho_h = 912\ kg\ m^{-3}$) . The density of gas (eq. 10) is calculated from the pressure (P) and temperature (T):

$$\rho_g = \frac{1}{\underline{V}} = \frac{P}{ZRT}, \tag{10}$$

where R is the specific gas constant (R=8.314 J/mol-K) and Z is the compressibility factor. Since the salinity is assumed constant, the brine density is also assumed to be constant ($\rho_l = 1025\ kg\ m^{-3}$).

Table 3 Constants in phase saturation calculations

Parameter	**Value**
Stoichiometric hydration number (N)	5.75
Methane hydrate density (ρ_h)	912 kg m^{-3}
Mole fraction of water in the liquid phase (X_w^l)	0.969
Mole fraction of vapor in the liquid phase (X_v^l)	0.02
Mole fraction of salt in the liquid phase (X_s^l)	0.0108

Mole fraction of water in the gas phase (X_w^g)	0.00
Mole fraction of vapor in the gas phase (X_v^g)	1.00
Mole fraction of water in the hydrate phase (X_w^h)	0.866
Mole fraction of vapor in the hydrate phase (X_m^h)	0.134

C5. Unsteady-State Relative Permeability Measurements

From the experiments in Chapter 4, the measured effluent can be used to determine the relative permeability using unsteady-state methods. To derive relative permeability curves, the effluent data is used to fit relative permeability curves. The experiments in Chapter 4 were not designed to measure relative permeability but since gas is injected into sample and the effluent is measured, relative permeability can be determined.

In both the hydrate-free and hydrate saturated samples, gas is injected into the sample and the effluent (gas+water) is measured. For the hydrate free experiment, the sample begins fully water saturated and flue gas is injected. All effluent, water and gas, is measured. Therefore, using the hydrate free experiment, a gas/water relative permeability curve can be derived. For the hydrate saturated experiment, the sample is saturated with water and hydrate. Gas is then injected, and all effluent is measured. From these effluent curves, a relative permeability of gas and water in the presence of hydrate can be determined. However, this is significantly more challenging because this is reactive flow and the hydrate saturation does not remain constant. Therefore, this work is still in progress. The experimental parameters and preliminary results are shared in Table 4.

Table 4 Experimental parameters and results for unsteady-state relative permeability work.

Experiment	**Hydrate Free**	**Hydrate Saturated**
Hydrate saturation	0	0.3
Pressure (PSI)	300	2000
Temperature (°C)	7.5	7.5

Total water in (g)	0	0
Total water out (g)	36	21
Total gas in (mL)	60.1	240.2
Total gas out (mL)	38.1	211.0

Additional data and the workbooks used to calculate these relative permeability values can be found on the repository for this appendix: https://github.com/zwmurphy/unsteady_state_rel_perm.

Bibliography

Archer, D., Buffett, B. A., & Brovkin, V. (2008). Ocean methane hydrates as a slow tipping point in the global carbon cycle. *Proceedings of the National Academy of Sciences*, *106*(49), 20596-20601. https://doi.org/10.1073/pnas.0800885105

Baker, L. (1988). Three-phase relative permeability correlations. SPE Improved Oil Recovery Conference,

Bear, J. (1972). *Dynamics of Fluids in Porous Media*. American Elservier Publishing Company, Inc.

Birkedal, K. A., Hauge, L. P., Graue, A., & Ersland, G. (2015). Transport mechanisms for co2-ch4 exchange and safe co2 storage in hydrate-bearnig sandstone. *Energies*, *8*. https://doi.org/doi: 10.3390/en8054073

Blunt, M. J. (2017). *Multiphase Flow in Permeable Media: A Pore-Scale Perspective*. Cambridge University Press. https://doi.org/10.1017/9781316145098

Boswell, R. (2009). Is gas hydrate energy within reach? *Science*, *325*(5943), 957-958. https://doi.org/10.1126/science.1175074

Boswell, R., & Collett, T. (2011). Current prospective on gas hydrate resources. *Energy & Environmental Science*, *4*, 10.

Boswell, R., & Collett, T. S. (2011). Current perspectives on gas hydrate resources [10.1039/C0EE00203H]. *Energy & Environmental Science*, *4*(4), 1206-1215. https://doi.org/https://doi.org/10.1039/C0EE00203H

Boswell, R., Schoderbek, D., Collett, T. S., Ohtsuki, S., White, M., & Anderson, B. J. (2017). The Iġnik Sikumi Field Experiment, Alaska North Slope: Design, Operations, and Implications for CO2–CH4 Exchange in Gas Hydrate Reservoirs. *Energy & Fuels*, *31*(1), 140-153. https://doi.org/10.1021/acs.energyfuels.6b01909

Brooks, R. H., & Corey, A. T. (1964). Hydraulic Properties of Porous Media. *Hydrology Papers*.

Chen, X., & Espinoza, D. N. (2018). Ostwald ripening changes the pore habit and spatial variability of clathrate hydrate. *Fuel*, *214*, 614-622. https://doi.org/10.1016/j.fuel.2017.11.065

Chen, X., Espinoza, D. N., Luo, J. S., Tisato, N., & Flemings, P. B. (2020). Pore-scale evidence of ion exclusion during methane hydrate growth and evolution of hydrate pore-habit in sandy sediments. *Marine and Petroleum Geology*, *117*. https://doi.org/10.1016/j.marpetgeo.2020.104340

Chen, X., Kianinejad, A., & A. DiCarlo, D. (2017). Measurements of CO2-brine relative permeability in Berea sandstone using pressure taps and a long core. *Greenhouse Gases: Science and Technology*, *7*(2), 370-382. https://doi.org/10.1002/ghg.1650

Clennell, M. B., Hovland, M., Booth, J. S., Henry, P., & Winters, W. J. (1999). Formation of natural gas hydrates in marine sediments 1. Conceptual model of gas hydrate growth conditioned by host sediment properties. *Journal of Geophysical Research*, *104*(B10), 22985-23003. https://doi.org/10.1029/1999jb900175

Cook, A. E., & Malinverno, A. (2013). Short migration of methane into a gas hydrate-bearing sand layer at Walker Ridge, Gulf of Mexico. *14*(2), 283-291. https://doi.org/10.1002/ggge.20040

Dai, S., Kim, J., Xu, Y., Waite, W. F., Jang, J., Yoneda, J., Collett, T. S., & Kumar, P. (2019). Permeability anisotropy and relative permeability in sediments from the National Gas Hydrate Program Expedition 02, offshore India. *Marine and Petroleum Geology*, *108*, 705-713. https://doi.org/10.1016/j.marpetgeo.2018.08.016

Dai, S., Santamarina, J. C., Waite, W. F., & Kneafsey, T. J. (2012). Hydrate morphology: Physical properties of sands with patchy hydrate saturation. *Journal of Geophysical Research: Solid Earth*, *117*(B11), B11205. https://doi.org/10.1029/2012JB009667

Dai, S., & Seol, Y. (2014). Water permeability in hydrate-bearing sediments: A pore-scale study. *Geophysical Research Letters*, *41*(12), 4176-4184. https://doi.org/10.1002/2014GL060535

Daigle, H. (2016). Relative permeability of hydrate-bearing sediments from critical path analysis. *Journal of Petroleum Science and Engineering*.

Darnell, K. N., Flemings, P. B., & DiCarlo, D. (2019). Nitrogen-Driven Chromatographic Separation During Gas Injection Into Hydrate-Bearing Sediments. *Water Resources Research*. https://doi.org/10.1029/2018wr023414

Darnell, K. N. F., P.B.; DiCarlo, D. (2017). Subsurface injection of combustion power plant effluent as a solid-phase carbon dioxide storage strategy. *Geophysical Research Letters*, *44*, 5521-5530. https://doi.org/10.1002/2017GL073663

Delli, M. L., & Grozic, J. L. H. (2014). Experimental determination of permeability of porous media in the presence of gas hydrates. *Journal of Petroleum Science and Engineering*, *120*, 1-9. https://doi.org/http://dx.doi.org/10.1016/j.petrol.2014.05.011

Dickens, G. R., O'Neil, J. R., Rea, D. K., & Owen, R. M. (1995). Dissociation of oceanic methane hydrate as a cause of the carbon isotope excursion at the end of the Paleocene. *Paleoceanogr.*, *10*, 965-971.

Eleri, O., Graue, A., & Skauge, A. (1995). Steady-state and unsteady-state two-phase relative permeability hysteresis and measurements of three-phase relative permeabilities using imaging techniques. SPE Annual Technical Conference and Exhibition, Dallas, Texas.

Fang, Y., Flemings, P. B., Daigle, H., Phillips, S. C., Meazell, P. K., & You, K. (2020). Petrophysical properties of the Green Canyon Block 955 hydrate reservoir inferred from reconstituted sediments: Implications for hydrate formation and production. *AAPG Bulletin*, *104*(9), 1997-2028. https://doi.org/10.1306/01062019165

Fang, Y., Flemings, P. B., Daigle, H., Phillips, S. C., & O'Connell, J. (2022). Permeability of methane hydrate-bearing sandy silts in the deep-water Gulf of Mexico (Green Canyon Block 955). *AAPG Bulletin*, *106*(5), 1071-1100. https://doi.org/https://doi.org/10.1306/08102121001

Fu, X., Jimenez-Martinez, J., Nguyen, T. P., Carey, J. W., Viswanathan, H., Cueto-Felgueroso, L., & Juanes, R. (2020). Crustal fingering facilitates free-gas methane migration through the hydrate stability zone. *Proceedings of the National Academy of Sciences*, *117*(50), 31660-31664. https://doi.org/doi:10.1073/pnas.2011064117

Henry, P., Thomas, M., & Ben Clennell, M. (1999). Formation of natural gas hydrates in marine sediments 2. Thermodynamic calculations of stability conditions in porous sediments. *Journal of Geophysical Research*, *104*(B10), 23005-23022. https://doi.org/10.1029/1999jb900167

House, K. Z., Schrag, D. P., Harvey, C. F., & Lackner, K. S. (2006). Permanent carbon dioxide storage in deep-sea sediments. *Proceedings of the National Academy of Sciences*, *103*(33), 12291-12295. https://doi.org/10.1073/pnas.0605318103

Jaiswal, N. J., Dandekar, A. Y., Patil, S. L., Hunter, R. B., & Collett, T. S. (2009). Relative permeability measurements of gas-water-hydrate systems. In T. Collett, A. Johnson, C. Knapp, & R. Boswell (Eds.), *Natural gas hydrates—Energy resource potential and associated geologic hazards: AAPG Memoir 89*.

Jang, J., & Santamarina, J. (2014). Evolution of gas saturation and relative permeability during gas production from hydrate-bearing sediments: gas invasion vs. gas nucleation. *Journal of Geophysical Research Solid Earth*, *119*, 116-126. https://doi.org/https://doi.org/10.1002/2013JB010480

Johnson, A., Patil, S., & Dandekar, A. (2011). Experimental investigation of gas-water relative permeability for gas-hydrate-bearing sediments from the Mount Elbert Gas Hydrate Stratigraphic Test Well, Alaska North Slope. *Marine and Petroleum Geology*, *28*(2), 419-426. https://doi.org/https://doi.org/10.1016/j.marpetgeo.2009.10.013

Kang, H., Koh, D.-Y., & Lee, H. (2014). Nondestructive natural gas hydrate recovery driven by air and carbon dioxide. *Sci Rep*, *4*. https://doi.org/dx.doi.org/10.1038/srep06616

Katagiri, J., Konno, Y., Yoneda, J., & Tenma, N. (2017). Pore-scale modeling of flow in particle packs containing grain-coating and pore-filling hydrates: Verification of a Kozeny–Carman-based permeability reduction model. *Journal of Natural Gas Science and Engineering*, *45*, 537-551. https://doi.org/https://doi.org/10.1016/j.jngse.2017.06.019

Khan, S. A., Pope, G. A., & Sepehrnoori, K. (1992). Fluid Characterization of Three-Phase CO2/Oil Mixtures. SPE/DOE Enhanced Oil Recovery Symposium,

Kleinberg, R. L., Flaum, C., Griffin, D. D., Brewer, P. G., Malby, G. E., Peltzer, E. T., & Yesinowski, J. P. (2003). Deep sea NMR: Methane hydrate growth habit in porous media and its relationship to hydraulic permeability, deposit accumulation, and submarine slope stability. *Journal of Geophysical Research: Solid Earth*, *108*(B10), 2508. https://doi.org/10.1029/2003JB002389

Kneafsey, T. J., Seol, Y., Gupta, A., & Tomutsa, L. (2011). Permeability of laboratory-formed methane-hydrate-bearing sand: measurements of observations using X-ray computed tomography. *SPE Journal*, *16*(1), 78-94.

Koh, D.-Y., Kang, H., Lee, J.-W., Park, Y., Kim, S.-J., Lee, J., Lee, J. Y., & Lee, H. (2016). Energy-efficient natural gas hydrate production using gas exchange. *Applied Energy*, *162*(Supplement C), 114-130. https://doi.org/https://doi.org/10.1016/j.apenergy.2015.10.082

Konno, Y., Fujii, T., Sato, A., Akamine, K., Naiki, M., Masuda, Y., Yamamoto, K., & Nagao, J. (2017). Key Findings of the World's First Offshore Methane Hydrate Production Test off the Coast of Japan: Toward Future Commercial Production.

Energy & Fuels, *31*(3), 2607-2616. https://doi.org/10.1021/acs.energyfuels.6b03143

Kralik, J., Manak, L., Jerauld, G., & Spence, A. (2000). Effect of trapped gas on relative permeability and residual oil saturation in an oil-wet sandstone. SPE Annual Technical Conference and Exhibition, Dallas, Texas.

Kvenvolden, K. A., & McMenamin, M. A. (1980). *Hydrates of natural gas; a review of their geologic occurrence* [Report](825). (Circular, Issue. U. S. G. Survey. http://pubs.er.usgs.gov/publication/cir825

Lake, L. W. (1989). *Enhanced oil recovery*. Prentice Hall. https://books.google.com/books?id=nm5MAQAAIAAJ

Lee, H., Seo, Y., Seo, Y.-T., Moudrakovski, I. L., & Ripmeester, J. A. (2003). Recovering Methane from Solid Methane Hydrate with Carbon Dioxide. *Angewandte Chemie International Edition*, *42*(41), 5048-5051. https://doi.org/https://doi.org/10.1002/anie.200351489

Lei, L., Park, T., Jarvis, K., Pan, L., Tepecik, I., Zhao, Y., Ge, Z., Choi, J. H., Gai, X., Galindo-Torres, S. A., Boswell, R., Dai, S., & Seol, Y. (2022). Pore-scale observations of natural hydrate-bearing sediments via pressure core sub-coring and micro-CT scanning. *Sci Rep*, *12*(1), 3471. https://doi.org/10.1038/s41598-022-07184-6

Lei, L., Seol, Y., Choi, J.-H., & Kneafsey, T. J. (2019). Pore habit of methane hydrate and its evolution in sediment matrix – Laboratory visualization with phase-contrast micro-CT. *Marine and Petroleum Geology*, *104*, 451-467. https://doi.org/10.1016/j.marpetgeo.2019.04.004

Lei, L., Seol, Y., & Myshakin, E. M. (2019). Methane Hydrate Film Thickening in Porous Media. *Geophysical Research Letters*, *46*(20), 11091-11099. https://doi.org/10.1029/2019gl084450

Liu, X., & Flemings, P. B. (2006). Passing gas through the hydrate stability zone at southern Hydrate Ridge, offshore Oregon. *Earth and Planetary Science Letters*, *241*(1–2), 211-226. https://doi.org/doi:10.1016/j.epsl.2005.10.026

Liu, X., & Flemings, P. B. (2007). Dynamic multiphase flow model of hydrate formation in marine sediments. *Journal of Geophysical Research*, *112*(B3). https://doi.org/doi:10.1029/2005jb004227

Liu, X., & Flemings, P. B. (2011). Capillary effects on hydrate stability in marine sediments. *Journal of Geophysical Research-Solid Earth*, *116*(B07102), 24. https://doi.org/10.1029/2010jb008143

Mahabadi, N., Dai, S., Seol, Y., & Jang, J. (2019). Impact of hydrate saturation on water permeability in hydrate-bearing sediments. *Journal of Petroleum Science and Engineering*, *174*, 696-703. https://doi.org/https://doi.org/10.1016/j.petrol.2018.11.084

Malinverno, A. (2010). Marine gas hydrates in thin sand layers that soak up microbial methane. *Earth and Planetary Science Letters*, *292*(3-4), 399-408. https://doi.org/10.1016/j.epsl.2010.02.008

Masson-Delmotte, V., Zhai, P., Pörtner, H.-O., Roberts, D., Skea, J., Shukla, P. R., Pirani, A., Moufouma-Okia, W., Péan, C., Pidcock, R., Connors, S., Matthews, J. B. R., Chen, Y., Zhou, X., Gomis, M. I., Lonnoy, E., Maycock, T., Tignor, M., & Waterfield, T. (2018). *Global Warming of 1.5°C. An IPCC Special Report on the impacts of global warming of 1.5°C above pre-industrial levels and related global greenhouse gas emission pathways, in the context of strengthening the global response to the threat of climate change, sustainable development, and efforts to eradicate poverty* (IPCC, Issue. https://www.ipcc.ch/sr15/

McConnell, D. R., Zhang, Z., & Boswell, R. (2012). Review of progress in evaluating gas hydrate drilling hazards. *Marine and Petroleum Geology*, *34*(1), 209-223. https://doi.org/10.1016/j.marpetgeo.2012.02.010

Meyer, D. W., Flemings, P. B., & DiCarlo, D. (2018). Effect of Gas Flow Rate on Hydrate Formation Within the Hydrate Stability Zone. *Journal of Geophysical Research-Solid Earth*, *123*(8), 6263-6276. https://doi.org/10.1029/2018jb015878

Milkov, A. V. (2004). Global estimates of hydrate-bound gas in marine sediments: how much is really out there? *Earth-Science Reviews*, *66*(3–4), 183-197. https://doi.org/https://doi.org/10.1016/j.earscirev.2003.11.002

Milkov, A. V., Dickens, G. R., Claypool, G. E., Lee, Y.-J., Borowski, W. S., Torres, M. E., Xu, W., Tomaru, H., Tréhu, A. M., & Schultheiss, P. (2004). Co-existence of gas hydrate, free gas, and brine within the regional gas hydrate stability zone at Hydrate Ridge (Oregon margin): evidence from prolonged degassing of a pressurized core. *Earth and Planetary Science Letters*, *222*(3–4), 829-843. https://doi.org/http://dx.doi.org/10.1016/j.epsl.2004.03.028

Moridis, G., Kowalsky, M. B., & Pruess, K. (2008). *TOUGH+HYDRATE v1.2 User's Manual: A Code for the Simulation of System Behavior in Hydrate-Bearing Geologic Media*. Lawrence Berkeley National Laboratory. http://escholarship.org/uc/item/23p861p4

Moridis, G. J., Kowalsky, M. B., & Pruess, K. (2007). Depressurization-Induced Gas Production From Class 1 Hydrate Deposits. *SPE Reservoir Evaluation & Engineering*, *10*(05), 458-481.

Moridis, G. J., Reagan, M. T., Kim, S.-J., Seol, Y., & Zhang, K. (2007). Evaluation of the Gas Production Potential of Marine Hydrate Deposits in the Ulleung Basin of the Korean East Sea. In.

Moridis, G. J., Reagan, M. T., Queiruga, A. F., & Boswell, R. (2019). Evaluation of the performance of the oceanic hydrate accumulation at site NFHP-02-09 in the Krishna-Godavari Basin during a production test and during single and multi-well production scenarios. *Marine and Petroleum Geology*, *108*, 660-696. https://doi.org/10.1016/j.marpetgeo.2018.12.001

Moridis, G. J., Seol, Y., & Kneafsey, T. J. (2005). Studies of Reaction Kinetics of Methane Hydrate Dissocation in Porous Media. In: Lawrence Berkeley National Laboratory.

Murphy, Z. W., DiCarlo, D. A., Flemings, P. B., & Daigle, H. (2020). Hydrate is a Nonwetting Phase in Porous Media. *Geophysical Research Letters*, *47*(16), e2020GL089289. https://doi.org/https://doi.org/10.1029/2020GL089289

Myshakin, E. M., Gaddipati, M., Rose, K., & Anderson, B. J. (2012). Numerical simulations of depressurization-induced gas production from gas hydrate reservoirs at the Walker Ridge 313 site, northern Gulf of Mexico. *Marine and Petroleum Geology*, *34*(1), 169-185. https://doi.org/10.1016/j.marpetgeo.2011.09.001

Myshakin, E. M., Seol, Y., Lin, J.-S., Uchida, S., Collett, T. S., & Boswell, R. (2019). Numerical simulations of depressurization-induced gas production from an interbedded turbidite gas hydrate-bearing sedimentary section in the offshore India: Site NGHP-02-16 (Area-B). *Marine and Petroleum Geology*, *108*, 619-638. https://doi.org/10.1016/j.marpetgeo.2018.10.047

Nole, M., Daigle, H., Cook, A. E., & Malinverno, A. (2016). Short-range, overpressure-driven methane migration in coarse-grained gas hydrate reservoirs. *Geophysical Research Letters*, *43*, 9500-9508. https://doi.org/10.1002/2016GL070096

Nole, M., Daigle, H., Cook, A. E., Malinverno, A., & Flemings, P. B. (2018). Burial-driven methane recycling in marine gas hydrate systems. *Earth and Planetary Science Letters*, *499*, 197-204. https://doi.org/10.1016/j.epsl.2018.07.036

Oak, M. (1991). Three-phase relative permeability of intermediate-wet Berea sandstone. SPE Annual Technical Conference and Exhibition?, Dallas, Texas.

Ohgaki, K., Takano, K., Sangawa, H., Matsubara, T., & Nakano, S. (1996). Methane exploitation by carbon dioxide from gas hydrates—phase equilibria for CO2-CH4 mixed hydrate system—. *Journal of chemical engineering of Japan*, *29*(3), 478-483.

Ota, M., Abe, Y., Watanabe, M., Smith, R. L., & Inomata, H. (2005). Methane recovery from methane hydrate using pressurized CO2. *Fluid Phase Equilibria*, *228-229*, 553-559. https://doi.org/https://doi.org/10.1016/j.fluid.2004.10.002

Paganoni, M., Cartwright, J. A., Foschi, M., Shipp, R. C., & Van Rensbergen, P. (2016). Structure II gas hydrates found below the bottom-simulating reflector. *Geophysical Research Letters*, *43*(11), 5696-5706. https://doi.org/10.1002/2016GL069452

Park, Y., Kim, D.-Y., Lee, J-W., Hyh, D.-G., Park, K.-P., Lee, J., & Lee, H. (2006). Sequestering carbon dioxide into complex structures of naturally occuring gas hydrates. *Proceedings of the National Academy of Sciences*, *103*, 12,690-12694. https://doi.org/https://doi.org/10.1073/pnas.0602251103

Phillips, S. C., Flemings, P. B., Holland, M. E., Schultheiss, P., Waite, W. F., Jang, J., Petrou, E. G., & Helen, H. (2020). High concentration methane hydrate in a silt reservoir from the deep-water Gulf of Mexico. *AAPG Bulletin*, *104*(9), 1971-1995. https://doi.org/https://doi.org/10.1306/01062018280

Phillips, S. C., Flemings, P. B., You, K., Meyer, D. W., & Dong, T. (2019). Investigation of in situ salinity and methane hydrate dissociation in coarse-grained sediments by slow, stepwise depressurization. *Marine and Petroleum Geology*, *109*, 128-144. https://doi.org/10.1016/j.marpetgeo.2019.06.015

Priest, J. A., Rees, E. V. L., & Clayton, C. R. I. (2009). Influence of gas hydrate morphology on the seismic velocities of sands. *Journal of Geophysical Research: Solid Earth*, *114*(B11), B11205. https://doi.org/10.1029/2009JB006284

Ruppel, C. D., & Kessler, J. D. (2017). The interaction of climate change and methane hydrates. *Reviews of Geophysics*, *55*(1), 126-168. https://doi.org/https://doi.org/10.1002/2016RG000534

Sakai, H., Gamo, T., Kim, E.-S., Tsutsumi, M., Tanaka, T., Ishibashi, J., Wakita, H., Yamano, M., & Oomori, T. (1990). Venting of Carbon Dioxide-Rich Fluid and Hydrate Formation in Mid-Okinawa Trough Backarc Basin. *Science*, *248*(4959), 1093-1096. https://doi.org/doi:10.1126/science.248.4959.1093

Schicks, J. M., Strauch, B., Heeschen, K. U., Spangenberg, E., & Luzi-Helbing, M. (2018). From Microscale (400 µl) to Macroscale (425 L): Experimental Investigations of the CO2/N2-CH4 Exchange in Gas Hydrates Simulating the Iġnik Sikumi Field Trial. *Journal of Geophysical Research: Solid Earth*, *123*(5), 3608-3620. https://doi.org/https://doi.org/10.1029/2017JB015315

Schoderbek, D., & Boswell, R. (2011). Iġnik Sikumi# 1, gas hydrate test well, successfully installed on the Alaska North Slope. *Natural Gas & Oil*, *304*, 285-4541.

Schoderbek, D., Martin, K. L., Howard, J., Silpngarmlert, S., & Hester, K. (2012, 2012/12/3/). *North Slope Hydrate Fieldtrial: CO2/CH4 Exchange*

Schuur, E. A. G., Bockheim, J., Canadell, J. G., Euskirchen, E., Field, C. B., Goryachkin, S. V., Hagemann, S., Kuhry, P., Lafleur, P. M., Lee, H., Mazhitova, G., Nelson, F. E., Rinke, A., Romanovsky, V. E., Shiklomanov, N., Tarnocai, C., Venevsky, S., Vogel, J. G., & Zimov, S. A. (2008). Vulnerability of Permafrost Carbon to Climate Change: Implications for the Global Carbon Cycle. *BioScience*, *58*(8), 701-714. https://doi.org/10.1641/b580807

Sloan, E. D., & Koh, C. A. (2007). *Clathrate Hydrates of Natural Gases*. CRC Press.

Smith, D. H., Seshadri, K., & Wilder, J. W. (2001). *Assessing the Thermodynamic Feasibility of the Conversion of Methane Hydrate into Carbon Dioxide Hydrate in Porous Media* Conference: National Conference on Carbon Sequestration, Washington DC, (United States), 15-17 May 2001; Related Information: Presentation given at the First National Conference on Carbon Sequestration, United States.

Spangenberg, E. (2001). Modeling of the influence of gas hydrate content on the electrical properties of porous sediments. *Journal of Geophysical Research: Solid Earth*, *106*(B4), 6535-6548. https://doi.org/10.1029/2000JB900434

Suzuki, K., Takayama, T., & Fujii, T. (2015). Density structure report from logging-while-drilling data and core data at the first offshore gas production test site on Daini-Atsumi Knoll around eastern Nankai Trough. *Marine and Petroleum Geology*, *66*, 388-395. https://doi.org/10.1016/j.marpetgeo.2015.02.026

Thomas, C., Phillips, S. C., Flemings, P. B., Santra, M., Hammon, H., Collett, T. S., Cook, A. E., Pettigrew, T., Mimitz, M., Holland, M., & Schultheiss, P. (2020). Pressure coring operations during The University of Texas-Gulf of Mexico 2-1 (UT-GOM2-1) Hydrate Pressure Coring Expedition in Green Canyon Block 955, northern Gulf of Mexico. *AAPG Bulletin*, *104*(9), 1877-1901. https://doi.org/10.1306/02262019036 van Genuchten, M. T. (1980). A Closed-form Equation for Predicting the Hydraulic Conductivity of Unsaturated Soils. *Soil Science Society of America Journal*, *44*(5), 892-898. https://doi.org/10.2136/sssaj1980.03615995004400050002x

Waite, W. F., Santamarina, J. C., Cortes, D. D., Dugan, B., Espinoza, D. N., Germaine, J., Jang, J., Jung, J. W., Kneafsey, T. J., Shin, H., Soga, K., Winters, W. J., & Yun, T. S. (2009a). Physical properties of hydrate-bearing sediments. *Reviews of Geophysics*, *47*(4). https://doi.org/10.1029/2008rg000279

Waite, W. F., Santamarina, J. C., Cortes, D. D., Dugan, B., Espinoza, D. N., Germaine, J., Jang, J., Jung, J. W., Kneafsey, T. J., Shin, H., Soga, K., Winters, W. J., & Yun, T. S. (2009b). Physical properties of hydrate-bearing sediments. *Reviews of Geophysics*, *47*(4), RG4003. https://doi.org/10.1029/2008rg000279

White, M. D., Kneafsey, T. J., Seol, Y., Waite, W. F., Uchida, S., Lin, J. S., Myshakin, E. M., Gai, X., Gupta, S., Reagan, M. T., Queiruga, A. F., Kimoto, S., Baker, R. C., Boswell, R., Ciferno, J., Collett, T., Choi, J., Dai, S., De La Fuente, M., . . . Zyrianova, M. (2020). An international code comparison study on coupled thermal, hydrologic and geomechanical processes of natural gas hydrate-bearing sediments. *Marine and Petroleum Geology*, *120*, 104566. https://doi.org/https://doi.org/10.1016/j.marpetgeo.2020.104566

Yoneda, J., Jin, Y., Muraoka, M., Oshima, M., Suzuki, K., Waite, W. F., & Flemings, P. B. (2022). Comprehensive pressure core analysis for hydrate-bearing sediments from Gulf of Mexico Green Canyon Block 955, including assessments of geomechanical viscous behavior and nuclear magnetic resonance permeability. *AAPG Bulletin*, *106*(5), 1143-1177. https://doi.org/https://doi.org/10.1306/04272120204

Yoneda, J., Jin, Y., Muraoka, M., Oshima, M., Suzuki, K., Walker, M., Otsuki, S., Kumagai, K., Collett, T. S., Boswell, R., & Okinaka, N. (2021). Multiple physical properties of gas hydrate-bearing sediments recovered from Alaska North Slope 2018 Hydrate-01 Stratigraphic Test Well. *Marine and Petroleum Geology*, *123*, 104748. https://doi.org/https://doi.org/10.1016/j.marpetgeo.2020.104748

Yoneda, J., Oshima, M., Kida, M., Kato, A., Konno, Y., Jin, Y., Jang, J., Waite, W. F., Kumar, P., & Tenma, N. (2019). Pressure core based onshore laboratory analysis on mechanical properties of hydrate-bearing sediments recovered during India's National Gas Hydrate Program Expedition (NGHP) 02. *Marine and Petroleum Geology*, *108*, 482-501. https://doi.org/10.1016/j.marpetgeo.2018.09.005

You, K., & Flemings, P. B. (2018). Methane Hydrate Formation in Thick Sandstones by Free Gas Flow. *Journal of Geophysical Research: Solid Earth*, *123*(6), 4582-4600. https://doi.org/10.1029/2018jb015683

You, K., & Flemings, P. B. (2021). Methane Hydrate Formation and Evolution During Sedimentation. *Journal of Geophysical Research-Solid Earth*, *126*(4). https://doi.org/10.1029/2020JB021235

You, K., Flemings, P. B., Malinverno, A., Collett, T. S., & Darnell, K. (2019). Mechanisms of Methane Hydrate Formation in Geological Systems. *Reviews of Geophysics*, *0*(ja). https://doi.org/https://doi.org/10.1029/2018rg000638

You, K., Kneafsey, T. J., Flemings, P. B., Polito, P., & Bryant, S. L. (2015). Salinity-buffered methane hydrate formation and dissociation in gas-rich systems. *Journal of Geophysical Research: Solid Earth*, *120*(2), 643-661. https://doi.org/10.1002/2014JB011190

Zatsepina, O. Y., & Buffett, B. A. (1998). Thermodynamic conditions for the stability of gas hydrate in the seafloor. *J. Geophys. Res.*, *103*(B10), 24127-24139. https://doi.org/10.1029/98jb02137